USF Tampa Graduate Theses and Dissertations

USF Graduate Theses and Dissertations

June 2022

Mm-Wave Reconfigurable Antenna Arrays, Phase Shifters and Beamforming Networks With Reduced Hardware Complexity Using Integrated Microfluidic Actuation

Jonas J. Mendoza Sandoval
University of South Florida

Follow this and additional works at: https://digitalcommons.usf.edu/etd

Part of the Engineering Commons

Mm-Wave Reconfigurable Antenna Arrays, Phase Shifters and Beamforming Networks

With Reduced Hardware Complexity Using Integrated Microfluidic Actuation

by

Jonas J. Mendoza Sandoval

A dissertation submitted in partial fulfillment
of the requirements for the degree of
Doctor in Philosophy in Electrical Engineering
Department of Electrical Engineering
College of Engineering
University of South Florida

Major Professor: Gokhan Mumcu, Ph.D.
Huseyin Arslan, Ph.D.
Nathan Crane, Ph.D.
Rasim Guldiken, Ph.D.
Jing Wang, Ph.D.

Date of Approval:
June 28, 2022

Keywords: microfluidics, reconfigurability, piezoelectric actuation, phased arrays

Dedication

This dissertation is dedicated to my wife, Marife, who has been my support throughout the past ten years of my life. I am confident she will be rewarded in an abundance of delight and triumph for all the sacrifices she endured for me to achieve this goal. This work is also dedicated to my parents, siblings, nephew, and son for their unconditional love.

Table of Contents

List of Tables

List of Figures

Abstract

Microfluidically reconfigurable radio-frequency (RF) devices, in general, are found attractive for low-loss, wide-frequency tunability, low hardware complexity, and high-power-handling capabilities. More recently, microfluidic actuation has also been proposed as an alternative to semiconductors and micro-electromechanical systems-based approaches to realize new and compact reconfigurable devices operating in mm-Wave bands. This research expands the knowledge base on low-loss and compact mm-Wave reconfigurable devices. The reconfiguration approach relies on utilizing a microfluidically actuated selectively metalized plate (SMP) within proximity of the RF device to alleviate the practical issues arising from the traditional usage of liquid metals in microfluidically reconfigurable devices.

The first novel concept is a microfluidically actuated spatially adaptive antenna array (MRSA) that can be used to achieve control of the mm-Wave wireless communication channel. MRSA concept is realized with a new compact RF feed network so that spatial adaptation on the order of several wavelengths can be accomplished without unnecessarily increasing the microfluidic system's size that enables this spatial adaptation. MRSA allows the improvement of the link-level performance of a wireless channel by 24%, from 8.5 bps/Hz to 10.5 bps/Hz. 100% improved system-level average spectral efficiency, and a 5 dB improvement in the average signal-to-interference ratio was achieved without additional antenna elements.

The second concept is a novel frequency reconfigurable antenna with integrated microfluidic actuation for the 28 GHz or 38 GHz mm-Wave bands. The device's novelty resides in a new multilayer integrated microfluidic actuator that can reposition multiple metalized plates

simultaneously within the microfluidic channel performing complex mechanical reconfigurations with reduced hardware complexity to achieve the desired functionality. It exhibits a realized gain of 5.6 dBi and 4.9 dBi at 28 GHz and 38 GHz, respectively, with improved loss compared to alternatives such as liquid metals, which exhibit challenges associated with actuation and liquid metal oxidization within channels that require lossy solutions for encapsulation.

The integrated actuation approach is subsequently utilized in a novel microfluidically reconfigurable mm-wave slow-wave phase shifter. The phase shifter achieves better loss and compactness when compared to other microfluidic technologies such as liquid metals and dielectric liquid loadings by utilizing a selectively metalized plate (SMP) repositionable within a microfluidic channel placed in close proximity to a microstrip line, creating a variable capacitive loading that alters the speed of its propagating wave. The device achieves total reconfiguration in approximately 50 ms, which is 39× higher than its predecessor.

Finally, by combining multiple phase shifters through a new design approach a mm-wave beamforming network is introduced to achieve beam steering antenna arrays. The beam steering is performed with a single microfluidic actuator and a circuit model is introduced to facilitate the design of the beamforming network. The design example presented is for a four-element antenna array operating at 28 GHz exhibiting continuous beam steering capability within $\pm 30°$ when its SMP is actuated within its -100 to 100 μm displacement range. Unlike beaming steering antennas using beamforming ICs, they do not require active amplification to compensate for high loss and have reduced hardware complexity associated with control bits and bias lines. Compared to previously investigated microfluidically actuated beam steering antennas, it offers the advantage of not relying on switched beam techniques and bulky lenses.

Chapter 1: Introduction

The combined effect of near future hyper-connected devices (IoT), new application-specific requirements, and the sub-6 GHz frequency spectrum reaching saturation have triggered an increased need for wireless systems operating at mm-Wave frequencies. However, mm-Wave communications suffer from high path propagation and blockage losses. Consequently, mm-Wave wireless networks are created to be densely deployed [1] while employing high-gain reconfigurable antenna arrays with electronic beam-steering capabilities [2, 3]. Moreover, implementing mm-Wave reconfigurable antennas increases hardware complexity with low power handling due to dense inter-element spacing, higher antenna element count, many active components, macro electromechanical motorized positioning systems, and the need for routing many RF bias and control signals. Unlike at lower frequency bands, the cost and power consumption of analog-to-digital and digital-to-analog (ADC/DAC) and macro electromechanical components prohibit realizing mm-Wave multiple-input–multiple-output (MIMO) architectures entirely in the baseband [4].

The most traditional technologies utilized in the design of mm-Wave reconfigurable antennas rely on silicon-based integrated circuits. IC technology, with GaAs such as RFIC, RF-SOI, or MMIC, has the advantage of high mass production. However, these technologies suffer from non-linear effects, increased losses, and low power handling at mm-Wave bands [5]. Contrary to IC technology, Micro Electromechanical Systems (MEMS) technology has been proposed to overcome IC's challenges at mm-Wave frequencies because of its low loss, high efficiency, and linearity. MEMS exhibits low loss and high-power handling but suffers from low

reliability and slower reconfiguration than IC performance [6]. Another technology implemented in reconfigurable antennas is macro mechanical repositioning. In mechanically actuated reconfigurable antennas, the actuation mechanism alters the antenna's resonating frequency, beam scanning angle, or spatial position of the elements. The method does not include switching mechanisms or optical fiber/laser diode integration. However, this technique depends on the device's physical limitations and results in heavy structures that increase power consumption and slow reconfiguration.

A more recent reconfiguration technology for antenna arrays utilizes microfluidics as the actuation mechanism. In microfluidically reconfigurable actuated devices, the reconfiguration is achieved by repositioning either a liquid metal [7] [8] or a dielectric material [9] inside a microfluidic channel by circulating a low-loss liquid dielectric. Subsequently, the liquid metal or dielectric relocation inside the microfluidic channel loads the RF device and modifies its geometry or RF performance. Due to the physically small size of the mm-Wave devices employed on 5G, reconfiguration of RF devices through microfluidic has proved promising in modern research for applications where high efficiency and low loss are required [10].

1.1 Research Goals and Contributions

This research aims to enhance the current knowledge on microfluidically reconfigurable antennas using selectively metallized plate (SMP) repositioning as the actuation principle. This technology's implementation is motivated by work that demonstrated highly reconfigurable RF devices in [11], [12], [13], [14], [15]. For this, four concepts were explored, and the outline, as well as specific contributions discovered, are as follows:

- Implementing microfluidic actuation based on SMP repositioning to introduce a novel Microfluidically Actuated Spatially Adaptive Antenna Arrays (MRSA) for Mm-Wave

Wireless Channel Control. This contribution is supported by introducing a novel RF feed that simplifies the MRSA's hardware complexity by reducing the SMP/Channel utilization.

- Demonstrating the first experimental verification of frequency reconfiguration based on microfluidic technology. This contribution is supported by introducing a novel frequency reconfigurable antenna with integrated microfluidic actuation for the 28 GHz or 38 GHz mm-Wave bands and presenting a multilayer microfluidic actuator that can reposition multiple metalized plates simultaneously within the microfluidic channel to achieve frequency reconfiguration.

- Introducing a novel mm-Wave microfluidically reconfigurable phase shifter (MRPS) with reduced hardware complexity using SMP-based microfluidically reconfiguration techniques. This contribution is supported by introducing a novel microfluidic actuated RF loading technique based on variable capacitive coupling generated by SMP repositioning within the microfluidic channel, thus altering the propagating wave's speed.

- Detailing a novel mm-Wave microfluidically reconfigurable phased antenna array (MRPAA) with beam steering capabilities and reduced hardware complexity. This contribution is supported by introducing a beamforming network built on multiple MRPS with zero IC count and spatial reconfiguration in the micron range. It is also supported by introducing a circuit representation describing the capacitive loading nature of the MRPAA.

1.2 Dissertation Outline

This dissertation is comprised of seven chapters. Chapter 2 provides a literature review of different reconfiguration technologies implemented for mm-Wave antennas. Chapter 3 presents a comprehensive study of microfluidically reconfigurable spatially adaptive antenna arrays (MRSA)

for mm-Wave wireless channel control. Chapter 4 introduces a microfluidically reconfigurable dual-frequency antenna (MRDA). Chapter 5 details an mm-Wave microfluidically reconfigurable phase shifter (MRPS) with reduced hardware complexity using SMP-based microfluidically reconfiguration techniques. Chapter 6 expands on the concept introduced in chapter 5 to study a microfluidically reconfigurable phased antenna array (MRPAA). Finally, Chapter 7 summarizes the dissertation and includes recommendations for future work.

Chapter 2: Background and Literature Review

The traditional wireless communications spectrum below 6 GHz is reaching a saturation point. Therefore, it is crucial to discover novel techniques and resources to provide higher capacity and data rates, reduced costs, as well as a consistent quality of experience. The efforts made on the resources side point toward utilization of higher frequency bands within the mm-Wave spectrum. However, the mm-Wave band has always been considered undesirable for wireless transmission due to several physical constrains such as high path loss, shadowing, high phase noise, and the increased cost of equipment necessary for its operation.

Reconfigurable antennas are a crescent topic among the RF/microwave research groups worldwide because of their promising potential to overcome some of the challenges presented by the mm-Wave band usage. A typical reconfigurable antenna employs adaptive characteristics to modify its frequency, polarization characteristics, radiation pattern, or a combination of the above to provide additional resources in wireless communications and/or reduce the hardware complexity and cost. Depending on the reconfiguration mechanisms, reconfigurable antennas can be classified into four main groups: those using electrical actuation principles such as IC, RF-MEMS systems, mechanical actuators, and those taking advantage of changes in the material properties of its components. This chapter explores different antenna reconfiguration principles and their applications in mm-Wave bands such as frequency reconfiguration, polarization reconfiguration, beamforming reconfiguration and spatial adaptation. It also highlights the current state-of-the-art RF/microwave reconfigurable antennas and a review of recent research on microfluidically actuated reconfigurable devices.

2.1 Mm-Wave Antenna Reconfiguration

The increasing trend of data-demanding applications requires an unprecedented increase in the volume of information traffic. These new applications satisfy users' requirements and draw new horizons for wireless operators to increase their revenue.

2.1.1 Challenges of Existing Mobile Networks

A quick look into recent statistics regarding wireless networks worldwide reveals that more than five billion devices demand wireless connections to run voice, data, and other applications. Mobile subscriptions have been growing around 2 percent year after year. In addition, LTE subscriptions have reached 4.6 billion, while WCDMA/HSPA reached 1510 million subscriptions (according to the Ericsson Mobility Report of November 2021). Over the long term, traffic growth is motivated by both the increasing number of smartphone subscriptions and the rising volume of data per subscription as burgeoning video content beckons more views.

2.1.2 The Mm-Wave Spectrum and 5G

The combined effect of near future hyper-connected devices (IoT), new application-specific requirements, and the fact that the actual frequency spectrum is reaching saturation have been the inspiration for advancing the so-called next-generation of wireless networks or 5G. It is usually presumed that 5G communication should address six goals that are not adequately addressed by 4G, higher capacities, higher data rates, lower latency, massive device connectivity, reduced costs, and consistent quality of experience provisioning [16]. As a result, the wireless industries as well as academic and research organizations, have all started collaborating on different aspects of 5G wireless systems.

Among the solutions proposed to reach the 5G goals, cellular networks are now aiming to explore the available, high-frequency mm-Wave band (ranging from 20 GHz to 300 GHz). As

compared to previous technologies, there is an abundance of frequency resources within the mm-Wave band. The U.S. Federal Communications Commission has approved and made available an additional 1.7 GHz of mm-Wave spectrum for use in 24 GHz and 48 GHz wireless bands [17]. This support also increases the already available mm-Wave spectrum in the 28 GHz, 37 GHz, 39 GHz, and 64-71 GHz bands - making a total of 13 GHz of probable spectrum for 5G networks.

Despite all the merits of mm-Wave technology, the mm-Wave band has traditionally been considered unsuitable for wireless transmission. In fact, the mm-Wave bands are characterized by too many challenges in physical, routing, and MAC layers for mm-Wave communications to be useful for 5G networks.

2.1.3 Understanding the Mm-Wave Wireless Channel

The physical layer in mm-Wave bands presents a challenge regarding communication performance. Among the characteristics that define the behavior of the physical layer in mm-Wave bands, the high propagation loss and its scattering characteristics play an important role. Additionally, wireless mobile communication is characterized by the random nature of the relative motion between users and access points. In fact, according to [18], [19] and [20], a proper wireless channel characterization can be defined by analyzing its propagation, shadowing, Doppler effect, and multipath loss performance.

2.1.3.1 Propagation Loss

The free space signal loss is stated by the Friis equation. The Friis equation formulates that the free space omnidirectional path loss increases proportionally to the square of the distance. This translates into high propagation loss due to ultra-small wavelengths. However, the use of a shorter wavelength allows not only for the miniaturization of the antennas but also for the formation of multiple narrow beams by using antenna arrays. The use of multiple antenna systems has recently

been proven to increase gain and reduce interference [21] by increasing spatial multiplexing capabilities.

2.1.3.2 Penetration and Shadowing

For effective system design, there is a need to understand mm-Wave propagation in diverse environments. There is a critical concern regarding obstacle obstruction because mm-Wave signals are incredibly susceptible to shadowing. Because of this, it is essential to understand the comportment of mm-Wave signals when propagating in the presence of ordinary objects.

The attenuation of mm-Wave for different materials has been previously investigated in [4], and materials such as concrete can attenuate signals by as much as 170 dB at 40GHz. Such behavior confines mm-Wave signals to small-cell environments. Propagation in a small cell environment looks promising for mm-Wave communications and automatically requires investigation into Non-Line of Sight (NLOS) propagation.

2.1.3.3 Multipath and NLOS

In wireless communications, multipath is the effect of receiving a signal in an antenna from several paths at a time and inflicting random variations of the received signal [18]. In simulations, [22] shows the difference in the propagation performance at two frequencies (i.e., 15 GHz and 28 GHz) and also remarks on the impact of diffuse scattering at 28 GHz. The above-mentioned phenomenon has been conventionally accepted as uncontrollable since it is assumed that the environment and the propagation scenario are random.

However, understanding multipath behavior might enable NLOS problem mitigation because there is a vast capacity inherent in multipath random fields, which can then be utilized to improve wireless channel performance [23].

2.1.3.4 Doppler Effect on Mm-Wave

The Doppler Effect represents the alteration in the received signal frequency due to the relative motion concerning the receiver and the emitter. The Doppler Effect is an important variable when designing mm-Wave wireless communication systems. According to [4], the Doppler shift on a 3GHz to 60GHz system with relative mobility between 3-350 km/h causes a frequency shift between 10Hz to 20kHz. However, the frequency shift due to multipath signals in mm-Wave scattering scenarios results in a phenomenon called Doppler spread. Doppler shift can be effectively controlled by adapting the receiver beamwidth, packet sizing, and proper coding over the coherence time of the channel.

2.1.4 Mm-Wave Antenna Reconfiguration to Improve Signal to Interference Ratio

Cell densification has been envisioned as the future scheme for the next-generation wireless network [24], resulting in the usage of ultra-small cells (i.e. microcells, picocells, and femtocells). Since small cells need to be deployed in a decentralized way, an increase in interference between each other and between users is expected. Regardless of the type of interference (inter-symbol interference, inter-user interference, and inter-antenna interference), all share the same mechanism of generation at mm-Wave in which multiple symbols, users, or data streams compete for the use of the same resource. Such interference behavior sequentially degrades the signal-to-interference ratio (SIR) and the error performance of the network while modifying the channel capacity [25]. In this sense, advanced interference mitigation techniques need to be deployed to combat interference and improve spectral efficiency.

According to [26], the new wireless communication systems are required to be cognitive and adjustable in order to overcome the inherent challenges associated with mm-Wave bands. As such, the evidence holds reconfigurable antennas as a promising solution for mm-Wave

applications. Moreover, reconfigurable antennas are not only for frequency reconfiguration but also for radiation pattern reconfiguration and polarization reconfiguration [27]. Their ability to be adaptive allows the reconfigurable antennas to provide multiple wireless applications. One of the main applications regarding reconfigurable antennas is cognitive radio. Cognitive radio systems are based on monitoring the transmission channels and searching for unused frequencies in the spectrum. Therefore, a cognitive radio requires an antenna that can efficiently identify changes in the communications channels and react accordingly [26].

2.2 State of the Art Reconfigurable Antennas

The deployment of 5G will require the design of both compact and efficient antennas. Lately, there has been a collective interest in developing an efficient antenna for mm-Wave to operate in the 28 GHz band and 38 GHz band. They will have the intelligence and capacity to adopt the most appropriate communications strategy based on feedback from channel sensing activities and signal quality assessment (i.e. the operating frequency, beam pattern and polarization).

Reconfigurable antennas facilitate the use of mm-Wave devices to deal with extendable and reconfigurable multiservice as well as for multiband operations with efficient spectrum usage and power utilization. These new strategies can be efficiently applied to reduce the number of components, hardware complexity, and cost compared to current radio technology. A typical reconfigurable antenna employs adaptive characteristics to modify either its frequency, polarization characteristics, radiation pattern, or a combination of the above. Depending on the reconfiguration mechanisms, reconfigurable antennas can be classified into three main groups: those using electrical actuation principles (i.e. PIN diodes, varactor diodes, and radio frequency

microelectromechanical systems [RF-MEMS]), those using mechanical drivers and those taking advantage on changes in the properties of the material.

2.2.1 Frequency Reconfigurability

A frequency reconfigurable antenna has the capability to cover a number of frequency bands for wireless communications. Currently, it is common for a single device to multitask services over a wide frequency range and to be operational at multiple frequency bands. Compared to multiband and wideband antennas, one of the merits of frequency reconfigurable antennas is that the antenna provides noise rejection in bands that are not in use, and as such, the filter requirements of the front-end circuits are significantly reduced. Frequency reconfigurable antennas can modify its operating frequency band - both in a continuous or discrete manner while keeping the polarization and radiation pattern stable.

2.2.1.1 Electrically Induced Reconfigurability

A frequency reconfigurable slot antenna with three tunable frequencies is presented [28]. The investigation presents a method that combines two approaches to reduce patch antenna dimensions. The addition of a slot in the ground plane shifts the frequency of the patch from 7.273 GHz to 4.267 GHz while keeping the dimensions of the antenna the same. Additionally, by altering the varactor, a series of successive bands could be obtained. The system frequency ranged from 4.65 GHz to 6.18 GHz. Similarly, a concept of frequency reconfigurable antenna based on S-PIN diodes has been investigated in [29]. The study shows the use of a reconfigurable aperture to replace the narrow wall of a rectangular waveguide. The aperture contains a silicon device covered with a conductor layer comprising four reconfigurable slots. S-PIN diodes are embedded under each slot and silicon technology allows for selected slots to be closed electronically.

Similarly, RF-MEMS actuated frequency reconfigurable antennas have been investigated in several studies. For instance, in [30], the authors propose the use of MEMS cantilevers to alter the height of a suspended patch antenna. The antenna uses voltage to modify the distance between the antenna and the ground plane, hence changing the fringing fields of the patch edges while increasing the resonance frequency.

According to the results, the resonant frequency of the antenna is 189.2GHz with an 18.7dB return loss. However, as a dc voltage is applied, the resonant frequency shifts to 191GHz at 42V dc voltage. Similarly, Luo *et al.* in [31] offer a cantilever approach for phase modulation. It is formed as a periodic structure that modifies the phase velocity of the wave propagating in the device. Each unit cell contains the antennas, and therefore beamforming is achieved by creating a progressive phase shift between the unit cells. The device achieves a ±15° beam steering range as the J-units are sequentially actuated.

Another implementation of MEMS technology as reconfiguration mechanism is the work by Ibrahim *et al.* in [32]; the work explores a reconfigurable monopole UWB antenna that operates at a frequency band from 3.2 GHz to 12 GHz. The reconfiguration is achieved by using an RF MEMS switch in a series configuration. The structure has two modes controlled by the RF MEMS switch. Similar to the previous study, the paper presented in [33] explores the use of an RF-MEMS switch while using a coplanar waveguide transmission line for signal transmission. The MEMS switch controls the two branches of the antenna which can work in four different frequency bands and achieve frequency reconfigurability.

2.2.1.2 Material Properties Reconfiguration

Antenna reconfigurability can also be achieved by changing the substrate characteristics with the use of materials such as liquid crystals and ferrites. The material change is obtained by

modifying the relative electric permittivity or magnetic permeability of a material. As an example, liquid crystals are used as reconfigurable materials due to their ability for continuous tuning, along with low power consumption and high integration capability. A study on this subject has been presented in [34], where a ferrite of relative permittivity 4.3 was used.

The antenna design was based on a waveguide cavity and a ferrite slab to accomplish frequency reconfigurability. Similarly, in [35], a slotted-waveguide antenna array was used in conjunction with two photoconductive switches to adjust the electrical length of the slot. The concept makes use of a photonics-based reconfigurable strategy to provide frequency tunability within the 28GHz and 38GHz frequency bands.

2.2.1.3 Mechanically Induced Reconfigurability

In mechanically actuated reconfigurable antennas, the actuation mechanism is obtained by the structural alteration of the radiating elements of the antenna. This method does not include switching mechanisms or optical fiber/laser diode integration. However, this technique is highly dependent on the physical limitations of the device.

In [36], a mechanically controlled frequency agile antenna was successfully designed, fabricated, and verified for its applications in wireless communication from 0.5GHz to 3GHz. The reconfigurability was achieved by adjusting the ground plane dimensions under the patch using an actuation mechanism based on liquid metal.

Another mechanical technique to achieve frequency reconfiguration involves the superposition of a metamaterial on top of the antenna, similar to the study proposed in [37]. The antenna is formed by a patch radiator covered in a metasurface in which several elliptical unit cells are arranged periodically. The frequency reconfiguration capabilities of the device can be impulsed by mechanically rotating the metasurface.

2.2.2 Radiation Pattern Reconfigurability

Pattern reconfigurable antennas allow for beam steering capabilities on RF devices. These reconfigurable antennas have become relevant for several applications in telecommunications and radar. The radiation pattern reconfigurable antennas mitigate interference by channeling the antenna's radiation in the direction of interest. This turns out to be an essential characteristic in mm-Wave applications where high path loss, shadowing, and Doppler Effect are relevant.

2.2.2.1 Electrically Induced Reconfigurability

The electrically induced antenna pattern reconfigurability has been investigated in [38]. The investigation presents a radiation pattern reconfigurable antenna with an operating band from 36GHz to 40GHz. The design possesses multiple antennas and comprises a tunable power divider.

The power divider feeds one or multiple antennas according to the system's directives and subsequently provides various radiation patterns. Similarly, another technique utilizes the activation of individual antenna elements to radiate and cover a specific region. This principle is utilized in [39], in which a beam-steering antenna based on lens antenna subarrays (LAS) is presented, and an mm-Wave beam-steering antenna consisting of L lens antenna subarrays (LASs) is introduced. Each LAS hosts an M-element feed antenna array at its focal plane. The desired single antenna on each LAS is fed through an SPMT, with each LAS connected to their respective phase shifters (PS). The switch and PS states can be used to steer the beam. According to the results of the study, the antenna performs with 8.5% $|S\ 11\ |<;$ -10 dB bandwidth, 15.7 dBi Gain, 5.2° H-plane half-power beamwidth, and 75° field of view.

2.2.2.2 Material Properties Reconfiguration

Material properties reconfiguration antennas have been investigated in [40]. The study presents the design and construction of a relatively large Fresnel lens (>18λ) using a true-time-

delay (TTD) metamaterial structure for low-profile applications (F/D<0.36) that provides the antenna with multiple-beam capabilities. According to the authors, multiple beams can be produced from a single lens antenna using multiple feed horns at the proper spacing.

2.2.2.3 Mechanically Induced Reconfigurability

An example of a radiation pattern reconfigurable antenna is reported in [41]. The antenna comprises a monopole with a couple of V-shaped parasitic elements (VPE) in which the motion of the VPE is controlled by a dielectric elastomer mechanical actuator. A prototype was used to validate the simulations as well as the relationship between VPE displacements and the voltage applied to the actuator. It was shown that the pattern changes are sufficient for diverse applications and the impedance match is reasonably maintained over a 20% bandwidth.

2.3 Current Research in Mm-Wave Microfluidically Reconfigurable Antennas

Due to the physically small size of the mm-Wave devices employed on 5G, fluidic reconfiguration of RF devices has proved to be a promising topic in modern research. As an alternative to MMICs or MEMS technology, microfluidics present favorable outcomes where high efficiency, high power handling and low loss are required. The microfluidic actuation as a reconfiguration mechanism for RF devices utilizes the recirculation of a dielectric liquid to alter the RF properties of the device. This chapter explores important research on microfluidic reconfigurable antennas that utilize either the electrical properties of the fluid to achieve reconfiguration, liquid metal actuation to modify its performance, and finally, antennas utilizing the novel approach of selectively metalized (SMP) to achieve reconfigurability.

Microfluidically actuated frequency reconfigurable antennas using dielectric properties of the liquid to achieve reconfiguration have been explored in [42], where a planar mm-Wave antenna with two microfluidic channels pipes located below the radiating edges of the antenna is

introduced. The flow of different dielectric liquid materials on the microfluidic channels allowed an operating frequency reconfiguration from 16.8GHz to 28.4GHz. The prototype in the investigation has a wide frequency tuning range (51% of the center frequency) with a 1.78 dB gain, and 27% radiation efficiency is calculated using numerical models. Similarly, a radiation pattern reconfigurable microfluidic antenna has been investigated in [43]. The study presents a microfluidic reactive impedance loading mechanism based on a colloidal fluid under the ground plane. Changes in the concentration of the fluid alter the impedance-loading factor, thereby facilitating a phase change in the radiated signal. The mechanism allows low loss and phase control over the microstrip patch element and explores the implementation of the technique for beam steering reflectarrays. Another interesting implementation of liquid dielectric properties to antenna reconfiguration is presented in [44], where a microstrip patch antenna with quartwer wave long stubs at each corner in a multilayered substrate achieves frequency and polarization reconfigurability by modifying the loading of the stubs. Each stub can be individually loaded by filing or withdrawing distilled water into a series of microfluidic channels under the stubs. The antenna achieves 7.85% frequency tuning in the 2400 MHz band with linear polarization when loading is symmetric and 5.76% frequency tuning with circular polarization when the loading is asymmetric. In an asymmetric loading configuration, the antenna can switch the sense of polarization between LHCP and RHCP by alternating the loading along the diagonals of the antenna. Another important aspect of this work is the use of 3D printed molds to cast PDMS structures instead of the traditional SU8 molding process.

Another popular method to achieve reconfigurable microfluidic devices is utilizing liquid metals to generate electrical contacts in the devices. Even though using liquid metals to achieve antenna reconfiguration comes with a set of drawbacks, such as the utilization of mercury which

16

is hazardous for humans and the environment, and the oxidation of the metal droplet inside the channel with the consequent reduction of conductivity, this technique presents several devices demonstrating its functionality [45] [46] [47]. Recent works on reconfigurable antennas utilizing liquid metal as a reconfiguration mechanism include the work done by Bharambe *et al.* in [48] demonstrating a planar antenna with the capability of achieving H-plane and E-plane beam scanning. The antenna utilizes the repositioning of liquid metal droplets inside five microfluidic channels acting as directors, reflectors and driven elements to form a reconfigurable quasi-Yagi array. Repositioning the liquid metal inside the 3D printed structures allow for ±48° steering in the H-plane and ±54° steering in the E-plane, covering as much as 23% of the spherical area with at least 5 dBi of realized. Similarly, Carrasco *et al.* in [49] introduced two concepts for reflectarray reconfiguration utilizing Galinstan instead of mercury. The first topology is based on the aperture-coupled patch antenna that is hexagonal and can be reconfigured by introducing Galinstan into two cavities that extends the patch. As the cavities fill, the antenna achieves dynamic frequency tuning due to the variation of its physical length. The antenna achieves a wide frequency tuning range from 34.45 GHz to 25.85 GHz as the cavities get filled. The investigation also explores the possibility of implementing phase reconfiguration by utilizing Galistan to alter the physical length of the delay line in a reflectarray configuration. The concepts were demonstrated using CST simulations showing a 360° phase range from 24 GHz to 32 GHz. In addition, the investigation explores the use of capillary burst valves to control the length of the delay line filling utilizing the sudden expansion at the interconnecting microchannel. The concept was experimentally verified to control the length of the delay line filling upon the application of external pressure.

Relevant and most cited references in this field include the investigation performed by Dey *et al.* in [11]. Dey investigated a frequency reconfigurable liquid metal antenna whose operation

principle relies on the movement of the liquid metal volume over a microstrip line feed network. The liquid metal antenna is capacitive coupled to the microstrip line while the liquid metal volume is actuated with a micro pump unit. To maximize the capacitive coupling between the metal volume and the microstrip line, the metal is enclosed within a PDMS structure bonded to the substrate. The concept was demonstrated by the design and experimental verification of a frequency-tunable monopole antenna operating from 1.29 GHz to 5.17 GHz. Similarly, a switchable liquid metal based slot is presented in [50]. The antenna operation principle was based on the continuous movement of a liquid metal volume over a 3D printed channel while superposing to the antenna slots. Simulation results prove that repositioning the liquid metal on top of the slots causes a frequency tuning bandwidth of 70%. A prototype was fabricated, and the tests show good agreement between simulations and measurements. The work performed by Arbelaez *et al.* in [51] introduces a microstrip circular patch antenna with frequency and polarization reconfigurability using liquid metal. The antenna contains a C-shaped slot at its center and its reconfigurability is achieved utilizing two putty containers and liquid metal to switch between four different states. The antenna exhibits linear polarization at 5.83 GHz with a gain of 2.68 dB, circular polarization (CP) at 6 GHz with a gain of, right-hand CP (RHCP), and LHCP observed at 6.15 GHz with a gain of 2.44 dB.

More recently, there has been an increased interest in repositionable metalized plate reconfigurable microfluidic devices. The technique consists of recirculating a fluid to generate the repositioning of a selectively metalized plate (SMP) inside a microfluidic channel [52] [53] [54] [55] [56] [57] [58] [59]. This technique has shown to be a practical approach to achieving low-cost, high-power capable, and compact devices while reducing the power consumption associated with a traditional mechanical actuation.

Among the most relevant research on this microfluidic technology using metalized plates reconfiguration, the study by Dey *et al.* in [60] used a meandered dipole antenna where the frequency tunability was accomplished by repositioning an SMP within the microfluidic, thereby acting as a parasitic short circuit to electrically connect different sections of the dipole. The device utilized external micropumps to circulate the fluid flow and achieve repositioning of the metalized plate inside the microfluidic channel and over the antenna gaps. The closing of such gaps with the metalized plate modifies the electrical length of the meandered dipole and reconfigures the antenna's resonance frequency. A fabricated prototype was experimentally verified and showed a tuning range between 0.88 GHz and 1.39 GHz. On a similar note, Dey *et al.* elaborated on the concept introduced in [11] of frequency reconfigurable microfluidic antennas by utilizing metalized plates in [55] as an alternative to the liquid metal reconfiguration approach. The monopole antenna showed a high RF power-handling capability utilizing a movable metalized plate located within a microfluidic channel to extend the electrical length of the monopole. The antenna was coupled to the feed mechanism through capacitive coupling. The monopole showed frequency reconfigurability from 1.7GHz to 3.5GHz. The evolution of the technology was scaled by exploring radiation pattern reconfigurability utilizing selectively metalized plates (SMP) inside a microfluidic channel. The concept explored by Gheethan *et al.* in [54] paves the way for reliable liquid-metal-free microfluidic reconfigurable devices with higher efficiency and improved power-handling capabilities. The study investigated microfluidic focal plane arrays (MFPAs) to obtain compact and high-gain beam steering antennas. The patch element had the ability to be repositioned at the focal plane of the microwave lens. The side lobe level was proven reduced with the novel non-resonant feed line and the performance improvements were experimentally verified through an eight-element extended hemispherical dielectric lens-based microfluidic focal plane

array prototype. The concept was then further explored by Gonzalez *et al.* in [61]. The study utilized SMPs as switching mechanism to activate individual antennas at different positions under the lens. This principle reduced the motion range required for complete actuation, therefore improving the performance of the microfluidic focal plane arrays. The prototype utilizes a repositionable SMP on top of a sectioned microstrip line. Depending on the position of the selectively metalized plate on the microfluidic channel, the plate acts as an ON/OFF switch aided by a strong capacitive coupling created between the plate and the feed line. The switches showed less than 0.1 dB insertion loss resulting in a wide band low loss feed network. The feed network was utilized in an 8 element 30 GHz MFPA with a measured gain value (>22 dB). Additionally, the concept was extended with the design of a 2D beam-steering an 8×8 array design. Another important reference for the work in this dissertation was performed by Yilmaz *et al.* in [58]. The work introduces a microfluidically repositionable (i.e., spatially adaptive) beam steering array concept (via EM modeling and simulations) to increase the capacity of mm-Wave communication systems by exploiting the spatial resource in random fields. The array was capable of repositioning itself within a 4.5 λ spatial range inside a 9λ microfluidic channel for a microfluidic channel utilization of 50%. In a multipath environment, this configuration was shown to increase the wireless channel gain beyond what could be achieved by a stationary antenna array. Unfortunately, the research did not address whether it is possible to increase the microfluidic channel utilization of the antenna array design. On the other hand, the device was not fabricated therefore, fabrication-related issues were not successfully addressed. The fabrication-related issues of the antenna are related to material softness and dimensions of the microfluidic channel (showed a high aspect ratio of "0.0062"). According to [62], the fabrication of low (<0.2) aspect ratio PDMS channels were shown to collapse, thus exhorting a complexity escalation during the fabrication process.

These challenges motivated further investigations on this topic and are addressed in Chapter 3 of this dissertation. Similarly, the work introduced by Qaroot *et al.* in [13] sets an important precedent on SMP actuated reconfigurable microfluidic devices that can be utilized to design phased antenna arrays. In this case, [13] explored a reflection phase shifter based on a quadrature hybrid coupler with reflective line terminations. The SMP can be repositioned along the microfluidic channel to modify the electrical length of the reflect lines utilizing the capacitive coupling mechanism due to the close proximity between the PCB and the SMP metallizations. The concept was demonstrated with a 9.5 GHz X-band phase shifter design that is 24 mm × 15 mm and operates with <0.95 dB insertion loss. The device could achieve 360° shift with a total reconfiguration of 9.5 mm of the SMP in 1.95 s. The actuation was carried with external micropumps. On this topic of actuation by external pumps, a more recent work by Gonzalez *et al.* in [14], aside from introducing a low loss switch at 30 GHz with wide bandwidth (18 GHz) that motivated part of the work in Chapter 4, the work is also relevant to this dissertation due to the introduction of a novel actuation mechanism utilizing an integrated approach based on piezoelectric disk actuation. The piezo disk deformation as a function of the applied voltage creates recirculation of the fluid inside the channel and therefore modifies the location of the SMP. The concept of integrated reservoirs motivates further development of compact actuations mechanisms such as vertically stacked reservoirs for microfluidic actuation.

Chapter 3: Spatially Adaptive Antenna Array for Mm-Wave Wireless Channel Control with Microfluidics Based Reconfiguration

[1]Mm-Wave communications suffer from a high path, propagation, and blockage losses. Consequently, mm-Wave wireless networks are planned to be densely deployed [1] while employing high-gain antenna arrays with electronic beam-steering capabilities [3, 23]. Phased antenna arrays (PAAs) are an attractive solution. However, mm-Wave PAAs exhibit high hardware complexity due to dense inter-element spacing, many antenna elements, many active components, and the need for routing of many RF, bias, and control signals. These challenges motivate novel approaches to hardware integration, packaging, and antenna array architectures. Silicon integrated circuits (ICs) have been demonstrated to support the beam-steering functionalities with high output power and excellent linearity. An example of this can be found in [63] where SiGe technology is employed to realize a 44 GHz transceiver architecture with integrated beam-steering capability for a 4×4 antenna array. Similarly, reference [64] reports a PAA IC for 5G communications based on SiGe BiCMOS technology. Reference [65] addresses the packaging of ICs and antenna arrays by resorting to a hybrid integration approach with multiple printed circuit board (PCB) layers. Other notable techniques being pursued in the packaging of PAAs are on-wafer integration [66], heterogeneous integration [67], and additive manufacturing [68, 69]. At the architecture level, subarrays [70] [71] [72], lens antenna subarrays [39],

---

[1] This chapter was published in IEEE as reference [120]. Permission is included in Appendix B

beamforming networks [73], and traditional lens antennas [74] are being investigated to reduce the complexity of PAAs.

Different from these approaches, we have recently demonstrated that providing a new spatial adaptation (i.e., changing the physical location) capability for mm-Wave PAAs increases the wireless channel capacity and system signal to interference ratio (SIR) [58]. Figure 3.1(a) shows a potential scenario where a spatially adaptive antenna array (SAA) is at the access point of a system. SAA maintains electronic beam-steering capability. Therefore, spatial adaptation adds a degree of freedom. By changing its position, SAA at the access point may alter/control the reflections/scattering in the environment to improve channel link capacity and system SIR (i.e., controlling/tailoring of multipath fading [75, 76]). A successful SAA design should consider the following:

- Spatial Adaptation Range: [77] shows that small-scale wireless channel changes with antenna location. Changing antenna location by $\lambda_0/2$ (λ_0 denotes free space wavelength) causes the received signal to be uncorrelated by 50% with the signal received in the previous location – implying a different multipath fading environment. The capability to vary position in many multiples of $\lambda_0/2$ is expected to maximize the possibility of finding a favorable multipath environment for maximizing link capacity and system SIR.

- Physical Size: Array assembly size should be kept close to its spatial adaptation range. A basic approach of connectorization of the antenna elements and cables for connecting to the printed circuit board (PCB) hosting the beam-steering electronics will be bulky, slow, and perhaps unsuitable for mm-Wave frequencies due to the antenna element spacing.

- Frequency: Since displacements of multiple wavelengths are desired, SAA becomes practical in mm-Wave bands and applications where multipath fading is still essential.

- Speed of Spatial Adaptation: Coherence time defines the time duration where the wireless channel is stable in each antenna location. One of the promising applications of mm-Wave systems is in indoor communication [78]. Studies on mm-Wave indoor communication channel characteristics show the coherence time of the channel can be up to 30 ms [79] [80]. Therefore, performing $\lambda_0/2$ motion in less than 30 ms may allow the system to employ better wireless channel conditions.

To satisfy the physical size and speed demands, we propose strategically designed antenna feed networks that allow moving only the antenna metallizations (e.g., patches) while keeping other parts of the array assembly (e.g., active ICs, beamforming ICs, and other frontends/backend electronics) fixed. The earlier work in [58] focused on the wireless system modeling and performance while utilizing simulation-only antenna gain data from a smaller (5 element) SAA that did not satisfy the physical size requirement well. In [58], spatial adaptation range is 4.2 λ_0, but the physical assembly length is significantly larger as 9.8λ_0. Actuation of antenna metallizations was planned to be carried out with microfluidics, hence making it a microfluidically reconfigurable SAA (MRSA) motivated by our work that demonstrated highly reconfigurable RF devices [11-14, 81, 82]. In addition, the proposed assembly in [58] is not practically implementable for large arrays due to the flexibility of the polymer housing of microfluidic channels, necessitating modifications in assembly and manufacturing. Hence, the main goal of this manuscript is to design and experimentally characterize an MRSA for the first time by also satisfying the SAA design needs.

This is accomplished with the following contributions:

- A novel feed network that provides a spatial adaptation range of 4.2 λ_0 with a minimum physical assembly length of 5.69 λ_0 (Section III). This is enabled by using metallizations

on both sides of the selectively metalized plate (SMP) repositioning within the microfluidic channel. As compared to literature [11-14, 81, 82], this is the first time SMP is metalized in both sides and for different RF functionality (impedance matching vs. antenna radiation), suggesting new possibilities for future microfluidically reconfigurable RF devices.

- The design of an 8-element MRSA (Section IV) with a new substrate stack-up (Section II) and its fabrication (Section V). Hard materials are used due to the failure of flexible materials of [58] and reliable actuation with high radiation efficiency ($>80\%$) is accomplished (Section VI).

- Demonstrating improvement in wireless channel link-level performance by 24%, system-level spectral efficiency by 100%, and average SIR by 5 dB using measured antenna gain vs. physical location data (Section VII). Since these improvements are achieved without boosting antenna array gain (i.e., 5 dB gain implies 3.2× more antenna elements), SAA offers significant savings in antenna numbers and supporting ICs.

3.1 Operation Principle

Figure 3.1(b) depicts the 3D view. Antenna elements are formed over a selectively metalized plate (SMP) inside a microfluidic channel. The channel is bonded over a PCB that carries the static section of the RF feed network consisting of 50 Ω microstrip lines. For experimental verification, the lines are extended to mount RF connectors. More PCB layers can be added under the microfluidic channel to keep the size compact in a full-scale implementation with beam-steering electronics. The patch antennas on the top surface of the SMP are electrically connected to the metallization layer on SMP's bottom surface. The bottom layer transfers RF signals efficiently between the microstrip lines of the PCB and antenna elements, while SMP may take any spatial location within the channel. As compared to the design of [58], this is a significant

(a)
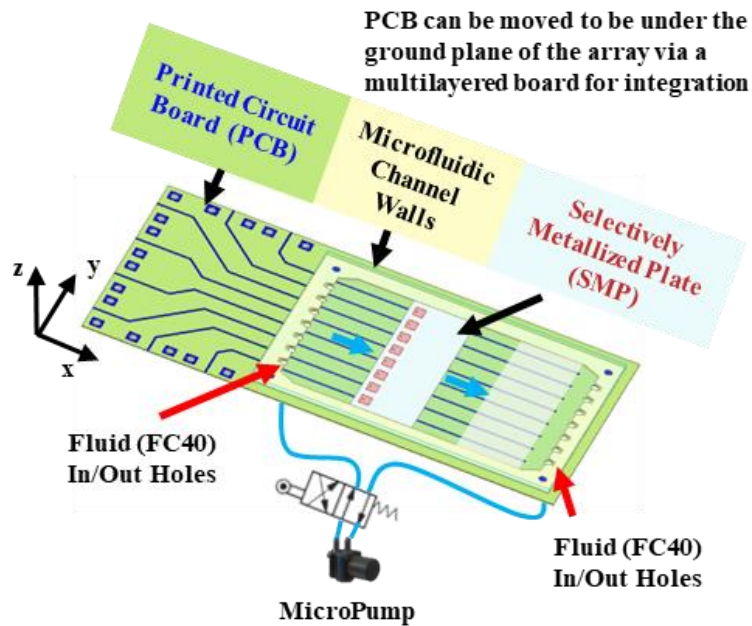
(b)

Figure 3.1: Spatially adaptive antenna array (SAA) concept. (a) Example application scenario; (b) 3D view of the microfluidically reconfigurable spatially adaptive antenna array (MRSA).

difference. By realizing a new feed transition on the bottom surface of the SMP (but not in the

form of a large number of resonators on PCB), the assembly size is significantly reduced.

The spatial adaptation of the SMP is achieved by circulating a low-loss dielectric liquid FC40 (ϵ_r = 1.9, tanδ = 0.0005). Although PDMS has been attractive for microfluidically reconfigurable RF devices, the high aspect ratio channels needed by the MRSA make PDMS impossible to use due to flexibility collapse [62]. The substrate stack-up is therefore formed from hard materials. As shown in Figure 3.2, 0.203 mm thick RO4003C laminates (ϵ_r = 3.55 and tanδ = 0.0027) are utilized for realizing both the PCB and SMP. The sidewalls of the channel are implemented from photoresist SU8 (ϵ_r = 3.25 and tanδ = 0.0270).

The top wall of the channel is formed with a 1 mm thick fused silica (ϵ_r = 3.81 and tanδ = 0.0002 [83]). The bottom surface of the SMP is coated with a 5 μm thick Parylene-N (ϵ_r = 2.40 and tanδ = 0.0006). This coating enforces a minimum constant gap between the SMP and PCB metallizations and potentially lowers friction. Microfluidic channel walls are 264 μm in total height to accommodate 203 μm thick SMP, 2×17 μm thick SMP metallizations, 5 μm Parylene-Ng, 17 μm thick PCB metallization, and 5 μm FC-40. FC-40 thickness is due to channel height non-uniformity in the fabrication process.
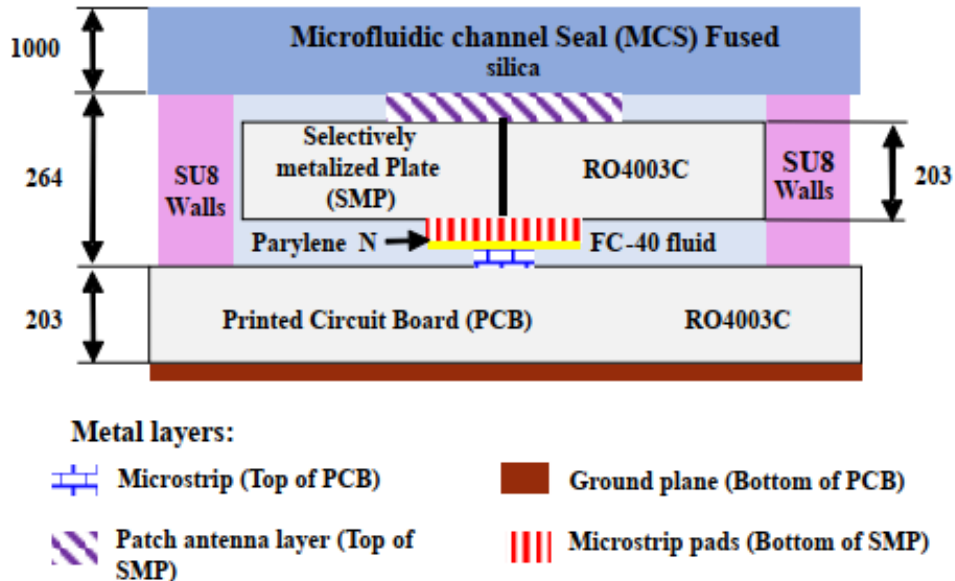

Figure 3.2: Substrate stack-up. (all dimensions are in μm).

3.2 Design

Figure 3.3(a) shows the top view of the antenna element that is used to form the MRSA. Keysight Advanced Design System (ADS) Momentum suite is employed for the feed network designs. The design is carried out in the following steps:
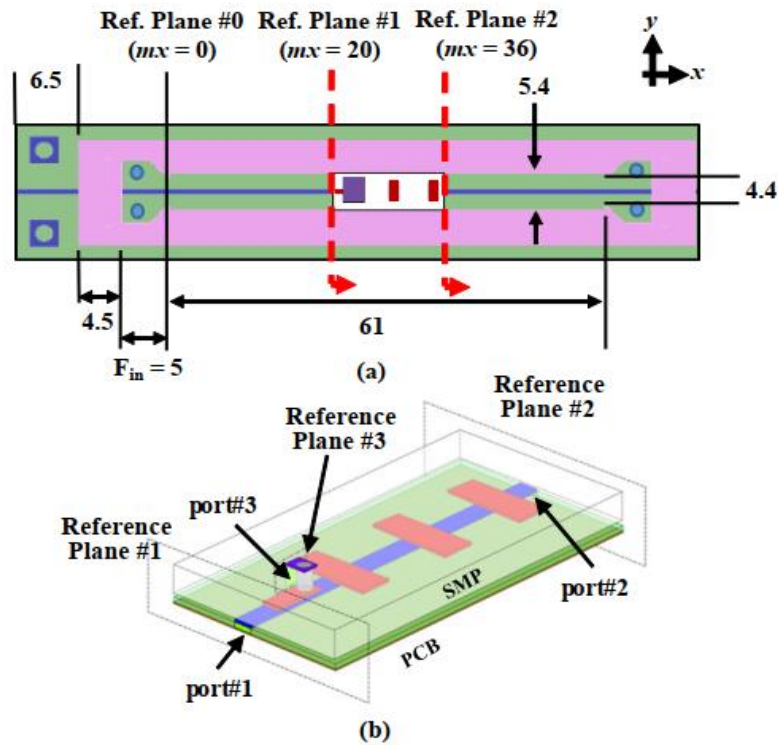
Figure 3.3: Single antenna element layout. (a) Top view; (b) 3D view of the SMP when the patch antenna is replaced with port #3. (all dimensions are in mm).

3.2.1 Static RF Feed Network

The static RF feed network consists of a microstrip line over the PCB. It is partially under the microfluidic channel and sidewalls. The ML is designed to exhibit 50 Ω characteristic impedance under these substrate stack-ups. Line sections displaying different widths are connected as shown in Figure 3.4. The line section referred to as TL1 is only over the PCB and exhibits 0.42 mm width. TL2 section lies under the sidewall of the microfluidic channel (SU8 + fused silica). It is in 0.36 mm width and designed using the approach reported in [54]. Its length is 4.5 mm and

Figure 3.4: Layout of the microstrip feed line. Dimensions are in mm.

matches the sidewall width. TL3 section is inside the microfluidic channel filled with FC-40. It is

0.4 mm wide and 61 mm long. TL3 is followed by 4.5 mm long TL2 and 7.44 mm long TL1
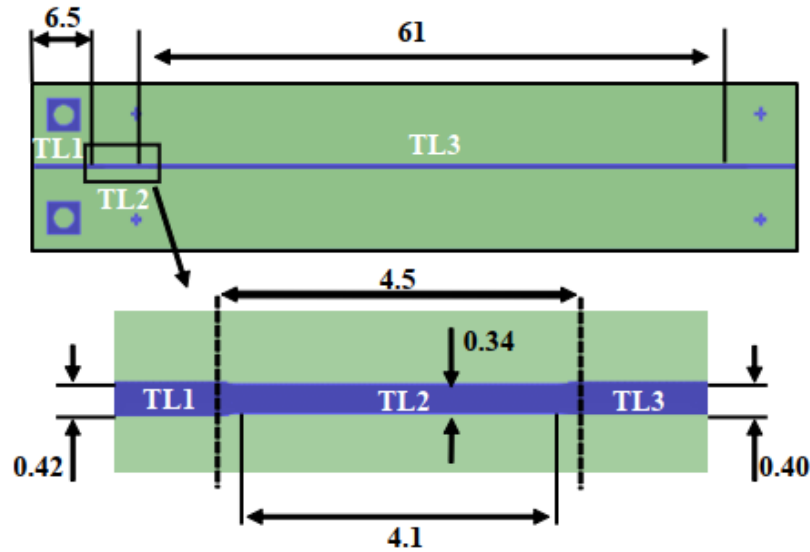
sections. The feed network is open-ended. Hence, the transition of the RF signal from the feed

network to the antenna on SMP must prevent signal loss and resonances associated with this type

of termination.

3.2.2 SMP

SMP has top and bottom surface metallization layers and a metalized via that electrically

connects them. First, the top layer is designed as a patch antenna without the presence of the bottom

layer (see Figure 3.5(a)). The metalized via is replaced with a port referred to as reference plane

and port #3. Figure 3.3(b) shows all reference planes and ports. Dimensions are tuned to achieve

a resistive input impedance of 30 Ω. Replacing the port with a 0.3 mm diameter metalized via-hole

creates a capacitive coupling between the SMP bottom metallization layer, transforming this

impedance to 50 Ω at the reference plane #1. Figure 3.5(b) depicts the bottom layer. A pad overlaps
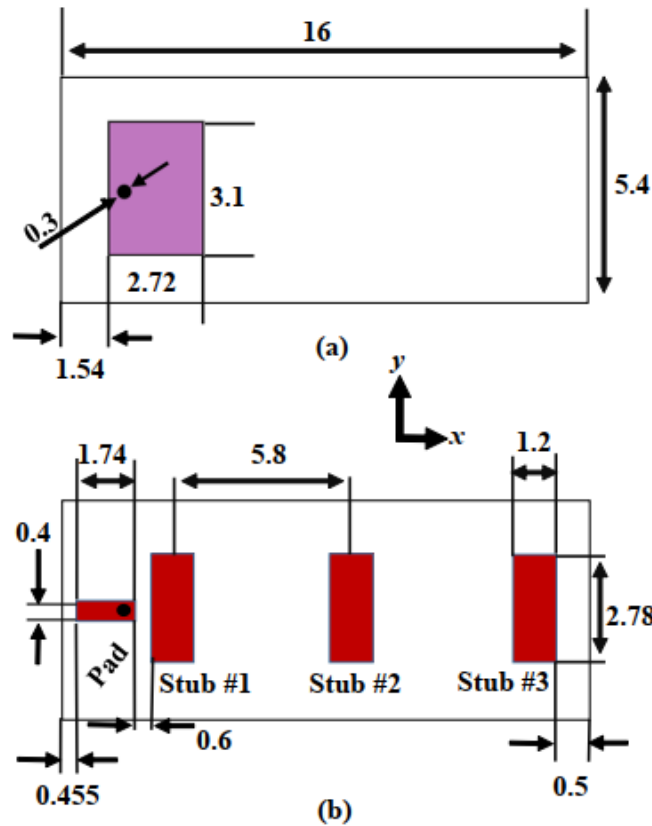
Figure 3.5: SMP layouts. (a) Top; (b) Bottom. Dimensions are in mm.

with the 0.4 mm wide microstrip line on the PCB to pick up the RF signal through capacitive coupling. The stubs periodically load the microstrip line on the PCB.

These stubs act as an RF block mechanism to prevent resonances of the open-ended microstrip line on the PCB. The design is based on an S-parameter analysis of a three-port network where the patch antenna is represented with 30 Ω port #3. The design goal is to maximize $|S_{31}|$ while minimizing $|S_{11}|$ and $|S_{21}|$. The length of the pad is designed when no stubs are present. Figure 3.6(a) presents $|S_{31}|$, $|S_{21}|$ and $|S_{11}|$ at 28 GHz for various pad lengths. Reflected power is minimized for 1.74 mm pad length. However, $|S_{31}|$ is only -3.6 dB, implying considerable RF signal leakage from reference plane #1 to #2. $|S_{21}|$ of the network confirms this by being -3.8 dB. To minimize the leakage, stub #1 is included. It is 1.39 mm in length, which represents a ~0.25 λ_g

Figure 3.6: S-parameters at 28 GHz. (a) As a function of pad length; (b) As a function of stub #1 position relative to the pad.
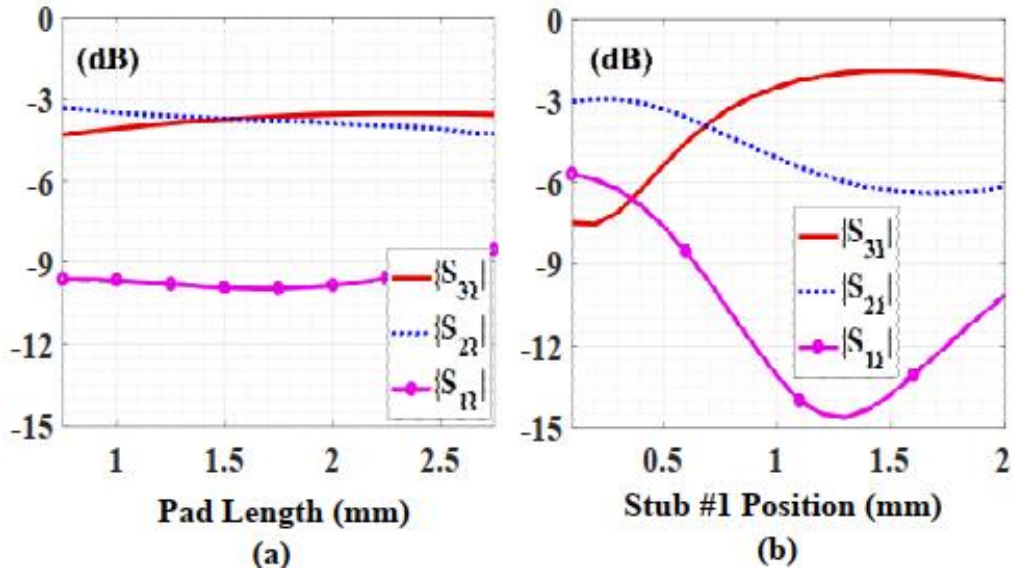
guided wavelength at 28 GHz. The stub approximates a short circuit condition on the microstrip line of the PCB. The initial stub width is 0.36 mm, corresponding to a 50 Ω impedance.

A parametric study on stub #1 position depicted in Figure 3.6(b) shows that reflected power is minimized when stub #1 is 1.25 mm separated from the pad. This is close to a quarter-wavelength and transforms the short-circuit condition realized by stub #1 to an open-circuit condition at the pad location. Figure 3.7(a) presents $|S_{31}|$ performance for varying stub widths. 1.2 mm wide stub maximizes the $|S_{31}|$. Stub #1 improves $|S_{31}|$ from -3.6 dB to -1.38 dB at 28 GHz. Inclusion of other stubs that are separated from each other by 5.8 mm (i.e. λ_g) further improves $|S_{31}|$. Figure 3.7(b) depicts the $|S_{31}|$ when the number of stubs is varied from one to four. The addition of the fourth stub affects the $|S_{31}|$ minimally. Consequently, the layout of the SMP is finalized with three stubs. Figure 3.8(a) presents the $|S_{21}|$, $|S_{11}|$, and $|S_{31}|$ for the finalized SMP layouts.

31
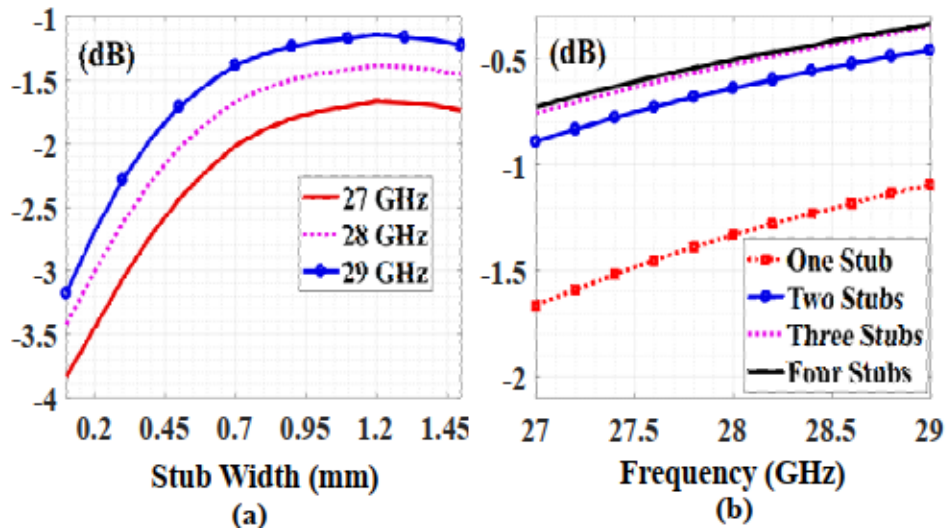
Figure 3.7: $|S_{31}|$ Simulations. (a) as a function of stub #1 width; (b) As a function of the frequency

The insertion loss between reference planes #1 and #3 is less than 0.4 dB at 28 GHz, with return losses exceeding 20 dB. Figure 3.8(b) depicts the insertion loss of the feed network at 28 GHz as a function of mx between reference planes #0 and #1. Loss linearly increases with mx as expected from a well-matched transmission line. Insertion loss remains below 1.1 dB, and SMP can take any position.
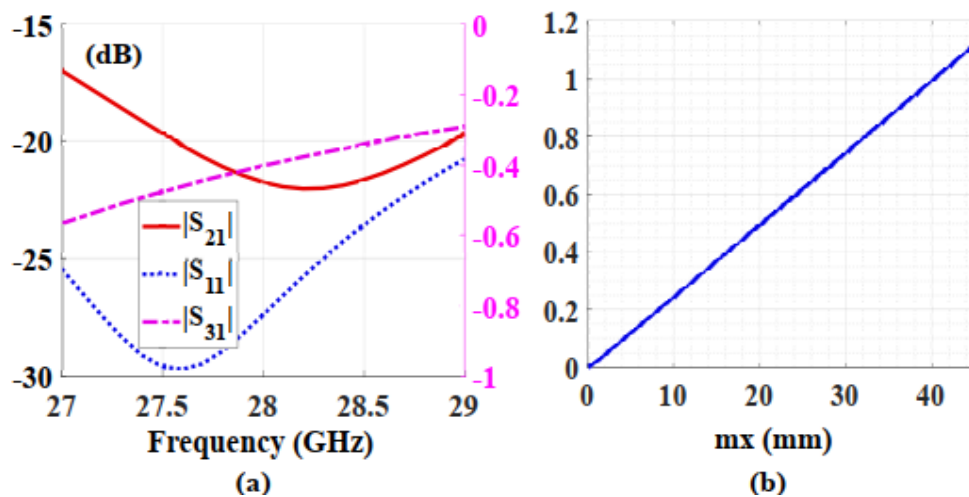
Figure 3.8: Simulated performance with finalized SMP layout. (a) S-parameters; (b) Feed network insertion loss vs mx at 28 GHz.

3.3 MRSA

MRSA design is shown in Figure 3.9. PCB and SMP widths are enlarged to accommodate replicas of the microstrip feed lines and SMP metallizations to include eight antenna elements. Antenna elements are evenly spaced at 5.4 mm ($\lambda_0/2$). The Microfluidic channel is enlarged to host the $16 \times 45 \ mm^2$ SMP. The overall size is $80 \times 50 \ mm^2$, excluding the extension lines that are connectorized for experimental purposes. The radiation performance of the MRSA is simulated using Ansys HFSS. Each microstrip feed line is excited by a 50 Ω lumped port. Figure 3.10 demonstrates $|S_{11}|$ of an antenna element as the array is repositioned across the microfluidic channel from $mx = 0$ mm to $mx = 45$ mm. $|S_{11}|$ is < -12 dB within the 27 GHz – 29 GHz frequency band. Simulated radiation efficiency is 84% at 28 GHz when the SMP is located closest to the feed ports, i.e., $mx = 0$ mm. The radiation efficiency is due to the dielectric loss of the materials (3.6%), conductor losses (3.6%), and the 0.4 dB insertion loss of the feed network to antenna transition (8.8%). Uniformly excited MRSA exhibits 14.86 dBi realized gain at 28 GHz with 12° half power beam width (HPBW) in the H-plane and less than -5 dBi back radiation gain. The E-plane HPBW
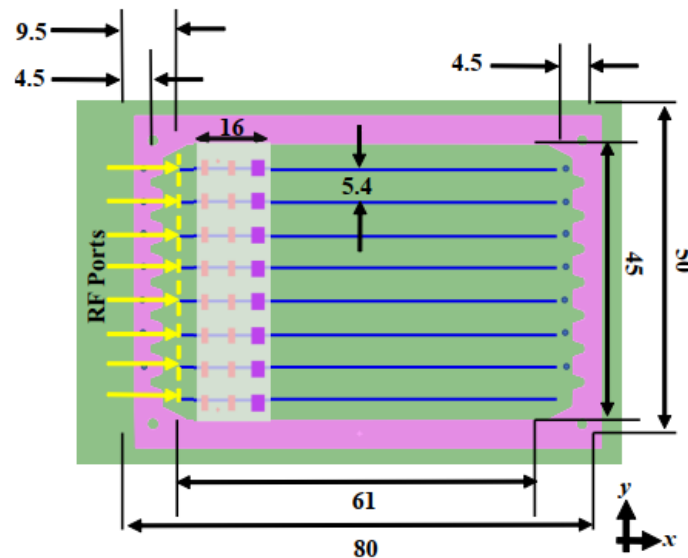

Figure 3.9: Eight element MRSA layout.
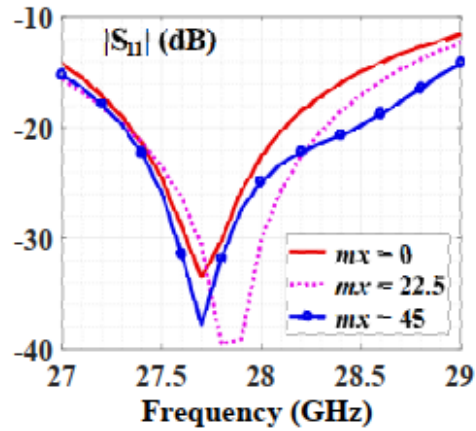
Figure 3.10: $|S_{11}|$ of a single element of the array for different mx.

is 48°. Figure 3.11(a) depicts the beam-steering in $12°$ increments in H-plane when $mx = 0$ mm. H-plane realized gain pattern could be scanned from -48° to 48° with a gain loss below 2.35 dB. The side lobe level is less than -12 dB. Figure 3.11(b) depicts the broadside gain of the MRSA for 0°, 24°, and 48° scan directions at 28 GHz as the SMP is repositioned within the microfluidic channel. The simulated realized broadside gain is worst for the 48° direction and remains > 9 dBi for all scan directions, including those not shown. The realized gain of the 48° scan is primarily associated with the expected scan loss.

The broadside gain varies by ± 1 dB of an average level. This is associated with the electrically large ground plane size of the array. As shown in Figure 3.11(c), the E-plane radiation pattern of the antenna exhibits ripples similar to the cases reported in previous literature [84, 85], implying contributions of scattered fields. As the array is repositioned, these contributions vary. Electromagnetic band gap structures (EBG) can improve the E-plane radiation pattern affected by surface wave refraction [86-88]. As shown in Figure 3.12(a), EBG can be placed within the side walls of the microfluidic channel. EBG unit cell is modeled in Ansys HFSS with the eigenmode solver. It is $2\times2\ mm^2$ and consists of a 0.3 mm diameter metalized via. The unit cell height is
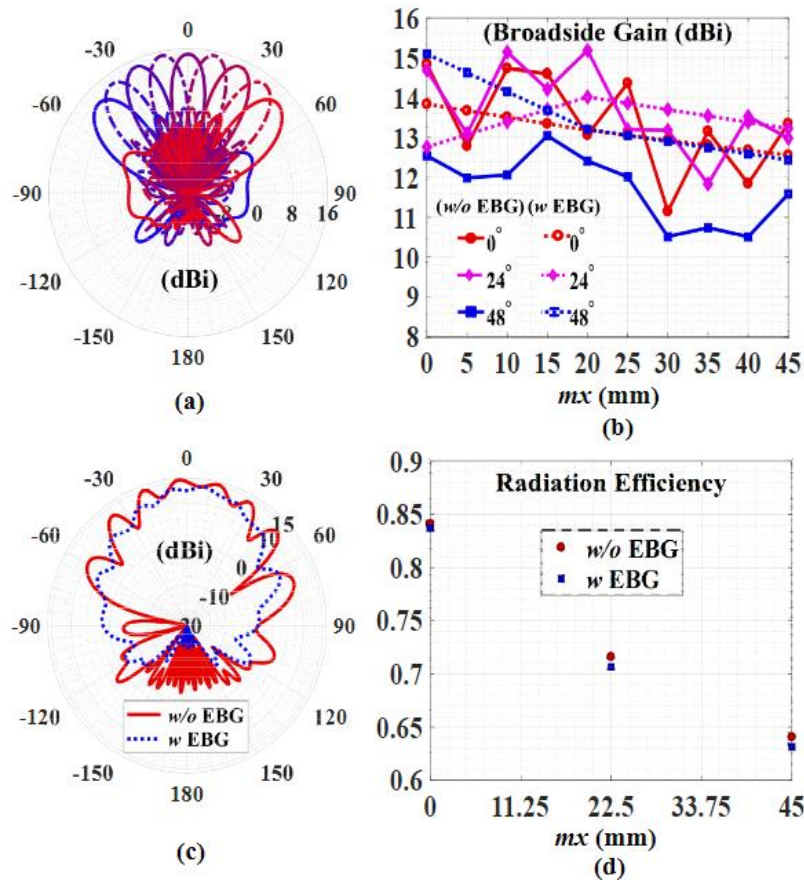
Figure 3.11: Comparison between simulation and measurements. (a) Realized gain pattern at 28 GHz for eight different steering angles in the H-plane (y-z) plane for $mx = 0$ mm; (b) Broadside realized gain vs SMP displacement for 0°, 24°, and 48° beam steering at 28 GHz with and without EBG; (c) Realized gain pattern in the E-plane at $mx = 0$mm; (d) Radiation efficiency for different mx positions.

1.467 mm and covers the entirety of the substrate stack-up. The dispersion diagram in Figure 3.12(b) shows that the design exhibits a band gap between 25 GHz and 40 GHz. With EBGs, the gain ripples can be eliminated, as seen in Figure 3.11(c). Broadside gain also gets stabilized for mx, as shown in Figure 3.11(b). Figure 3.11(d) presents the simulated radiation efficiencies for both approaches. Inclusion of EBGs causes only a 1% reduction in radiation efficiency. The drop in the radiation efficiency with mx is associated with increasing feed network loss. Fabrication of metalized vias through fused silica substrate is out of the current capabilities of our laboratory.

Hence, the experimental characterization is carried out without the EBGs. Nevertheless, the wireless communication system evaluation based on measured antenna performance still shows significant benefits arising due to the proposed spatial adaptation capability. This improvement is expected since the wireless channel gain observed in different mx positions exhibits statistically distributed fading (i.e., channel gain fluctuations). Hence, the multiplication of antenna gain and wireless channel gain that governs the overall system performance consistently exhibits statistically distributed ripples even if the MRSA gain is smoothed out with the EBGs. Therefore, at the system level, small ±1 dB gain ripples related to the surface wave scattering are not critical for the overall performance.
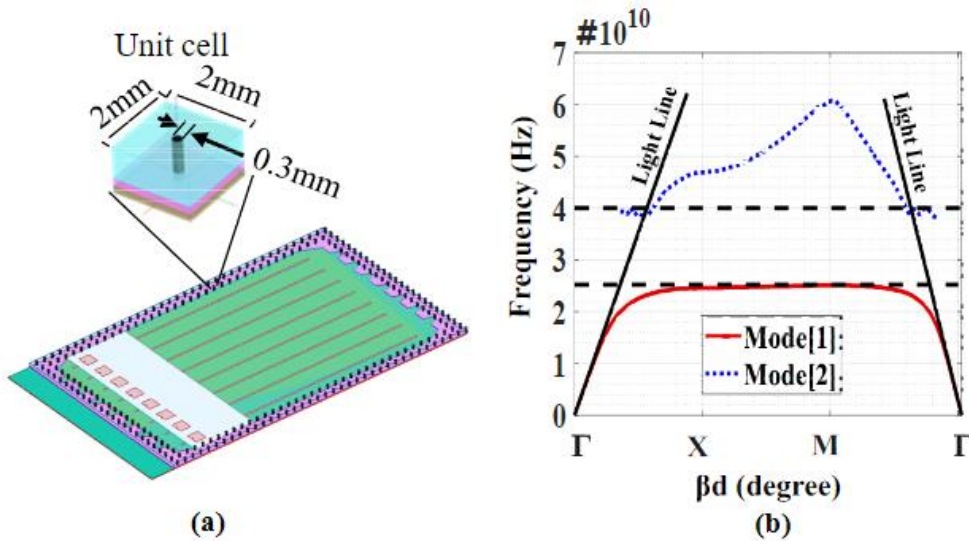
Figure 3.12: Implementing EBG structures for surface waves suppression. (a) MRSA with EBGs in microfluidic channel walls; (b) Dispersion diagram for the EBG.

3.4 Fabrication

Microfluidically reconfigurable RF devices with rigid channel walls are not commonly pursued as compared to flexible material-based approaches such as PDMS [89]. Among the limited work, reference [90] uses laser machined Poly Methyl Methacrylate (PMMA) and bonds it with

an inkjet-printed photo-paper substrate. The bonding is performed by using inkjet-printed SU8 as a glue agent. Similarly, [91] uses a silica-based superhydrophobic coated PMMA as microfluidic channel material on a liquid metal-based reconfigurable antenna. The bonding is performed by using a Norland Optical Adhesive-63 glue. Likewise, [92] proposes a frequency reconfigurable slot antenna enabled by liquid metal actuation inside an S-glass microfluidic channel. These are different from the substrate stack-up utilized in this work. Most recently, in [14], we used a substrate stack-up that is similar to the one in this paper. Due to the brevity of [14], fabrication details were not given. In addition, the size and aspect ratios of the channels for MRSA are considerable, making its manufacturing details critical for repeatability.

The PCB and SMP are patterned using photolithography. The RO4003C substrate is spin-coated with a thin layer of AZ® 12XT negative photoresist at 2000 rpm. This is followed by a soft bake for 120 s at 110°C. The coated substrate is exposed to 110 mJ/cm^2 dosage through the lithography mask. The mask includes the patterns for the pads, patches, via holes, microstrip lines, and alignment marks. The exposed substrate is soft baked for 60 s at 90 °C. Subsequently, the photoresist is developed with AZ 300MIF. The PCB and SMP patterns are completed using a copper etchant and rinsing. A dicing saw is used to cut the PCB and SMP to desired dimensions. LPKF Protomat S63 milling machine is used to drill the via holes and perform plating using the LPKF ProConduct paste. The 0.203 mm thick PCB is first bonded with a 1.5 mm thick RO4003C substrate to reduce its flexibility. Subsequently, it is spin-coated with a 254 µm thick layer of SU8 in two spin-coating steps. First, the SU8 layer is spin-coated at 1500 rpm for 45 s and soft baked for 25 minutes at 95 °C. The second SU8 layer is spin-coated at 2200 rpm for 45 s and then soft baked for 45 min at 95 °C. The spin coating process is followed by a 400 mJ/cm^2 UV exposure and three steps of post-exposure baking profile. The first section of the baking profile keeps the

PCB at 60 °C for 7 min. The second step ramps the temperature up to 90 °C in 20 min. The final step cools down the PCB to room temperature. The application of multiple SU8 coatings and the utilized temperature profile reduces deformation and planarizes the SU8 walls. Profilometer characterizations demonstrate a ±10 µm height variation across the SU8 layer. The final step in the preparation of microfluidic channel walls is the development of the SU8 layer and rinsing of the PCB substrate.

The channel sidewalls are bonded with the fused silica using the adhesive bonding technique described in [93]. First, a 20 µm thick SU8 layer is spin-coated on a polyamide surface. Subsequently, the spin-coated polyimide surface is brought in contact with the sidewalls of the microfluidic channel to transfer uncured SU8 from the polyamide surface to the top surface of the sidewalls (i.e., contact imprinting).
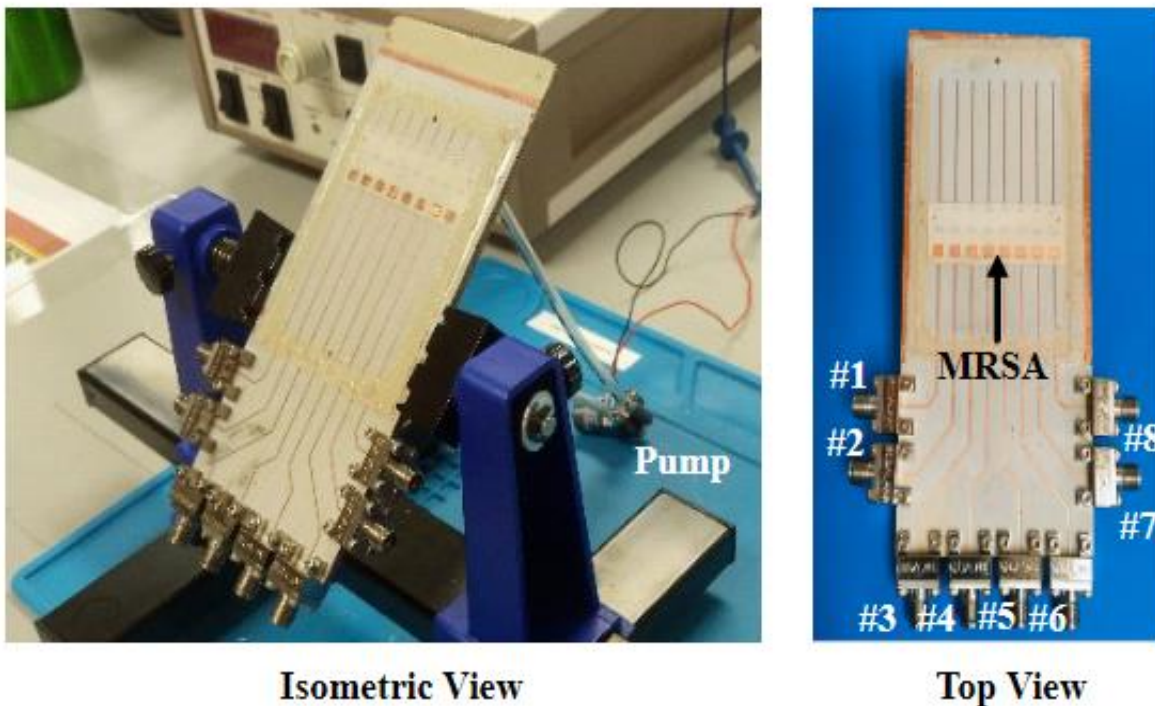

Figure 3.13: Experiment setup for the MRSA.

Next, the PCB with the thin SU8 bonding layer is kept at 60 °C for 10 minutes to minimize the SU8 viscosity and leak into the channel during contact bonding with the fused silica. The fused silica substrate is then pressed against the microfluidic channel and kept at 90 °C for 2 min. Figure 3.13 shows the MRSA prototype. The liquid FC40 is actuated by a TCS M100 pump through the fluid in/out holes at the back of the PCB structure. 3 mm internal diameter Teflon pipes and valves connect the pump to the microfluidic channel. The entry points to the microfluidic channel are fitted with PDMS-based adapters as used in our previous work [94].

3.5 Experimental Verification

The reconfiguration speed of the prototype is characterized as 14.3 λ_0/s (154 mm/s) which implies 35 ms per λ_0/2 displacement. The speed is achieved with 2 V DC voltage. It is possible to attain λ_0/2 displacement in 15 ms with the maximum pump capacity achieved at 3 V DC voltage. However, increased speed has caused unreliability in PDMS/tube adapters for our set-up. Future prototypes can utilize larger peripheral pipes and liquid in/out ports to improve reliability at the PDMS/tube adapters. As explained in the introduction, these actuation times are suitable for indoor communications. Figure 3.14(a) and (b) present $|S_{11}|$ elements #3 and #1 since they are connected to their own RF edge connectors with the shortest and longest transmission lines. The difference between the simulated and measured $|S_{11}|$ primarily due to the TL1, TL2 and RF edge connectors not being included in the simulations. In addition, fabrication tolerances/errors may contribute to the differences. Nevertheless, all antenna elements in the MRSA prototype (including the elements whose $|S_{11}|$ are not shown for brevity) are well-matched with $|S_{11}|$ below -10 dB. Figure 3.15(a) depicts the measured realized gain of the MRSA at 28 GHz for different beam-steering angles in the $mx = 0$ positions. The radiation pattern of each antenna element is measured while other elements are terminated with 50 Ω loads.
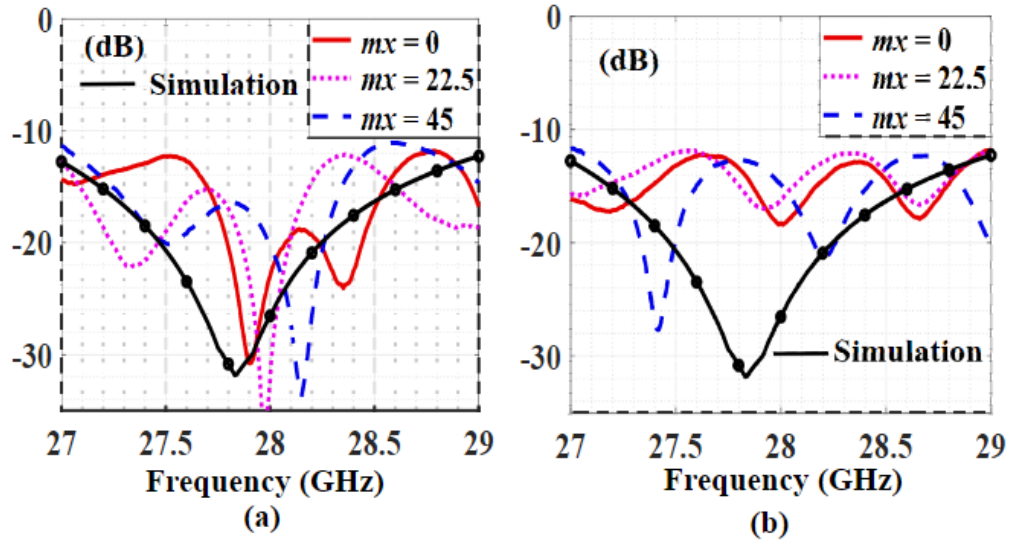
Figure 3.14: $|S_{11}|$ Measurements. (a) Element #3; (b) Element #1.

The measured radiated fields of the antenna elements are summed in software with phase shifts to generate beam-steering in H-plane with 12° increments. The phase delay and insertion loss of the microstrip extension lines used to connect with the edge connectors are calculated with Keysight ADS and compensated for in the radiated field summation. Edge connectors exhibit 0.5 dB insertion loss in this frequency range, which is accounted for in the radiation pattern summation. As shown in Figure 3.15(a), simulated and measured realized gain values are in good agreement. MSRA exhibits 14 dBi measured realized broadside gain at 28 GHz for $mx = 0$ and 12° HPBW in the H-plane. Figure 3.15(b) compares simulated and measured 28 GHz broadside realized gains of the MSRA for 0°, 24° and 48° beam-steering angles at different mx. The array shows a realized gain higher than 9 dBi for all beam-steering angles, including those not shown here. The average variation between the measured and simulated realized gain is 1.08 dBi. This difference can be related to slight misalignments in fabrication and anechoic chamber measurements. In addition, the ground plane size for the prototype is larger than the simulated model (see Figure 3.1(b) vs. Figure 3.9) due to the inclusion of connectors.
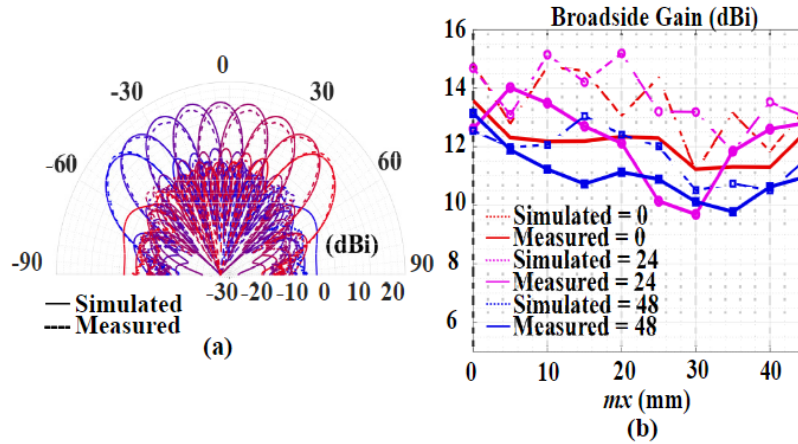
Figure 3.15: Realized gain measurements. (a) Realized gain pattern for mx = 0mm; (b) Broadside realized gain vs mx for multiple beam steering directions.

3.6 System Evaluation

To demonstrate the advantages of MRSA, wireless system and link-level performance simulations are carried out based on the measured H-plane gain patterns obtained from the MRSA prototype at varying mx positions. Measured H-plane gain patterns include all the nonidealities stemming from the feed network losses and realized gain variations as a function of mx. Hence, the presented system evaluation provides insight into performance under realistic/practical situations. Simulations follow a similar approach to [58]. Path loss model is assumed as PL(dB) = 72 + 29.2log10(d) based on [95], where d is the distance between transmitter and transmitter. First, link-level simulations are performed in a scattering environment. Up to 4 scatterers are randomly placed with Poisson distribution to generate a multipath channel in $800\,\lambda_0 \times 800\,\lambda_0$ area between the transmitter and receiver. Only the transmitter is assumed to be equipped with the MRSA, whereas the receiver antenna is omnidirectional. The transmitter beam and location are selected to maximize the received signal strength. Assuming a noise floor of -174 dBm, the spectral efficiency of the wireless channel link is calculated. Figure 3.16(a) presents the link-level spectral efficiency when the transmitter is equipped with omni directional antenna, a traditional 8-element beam-
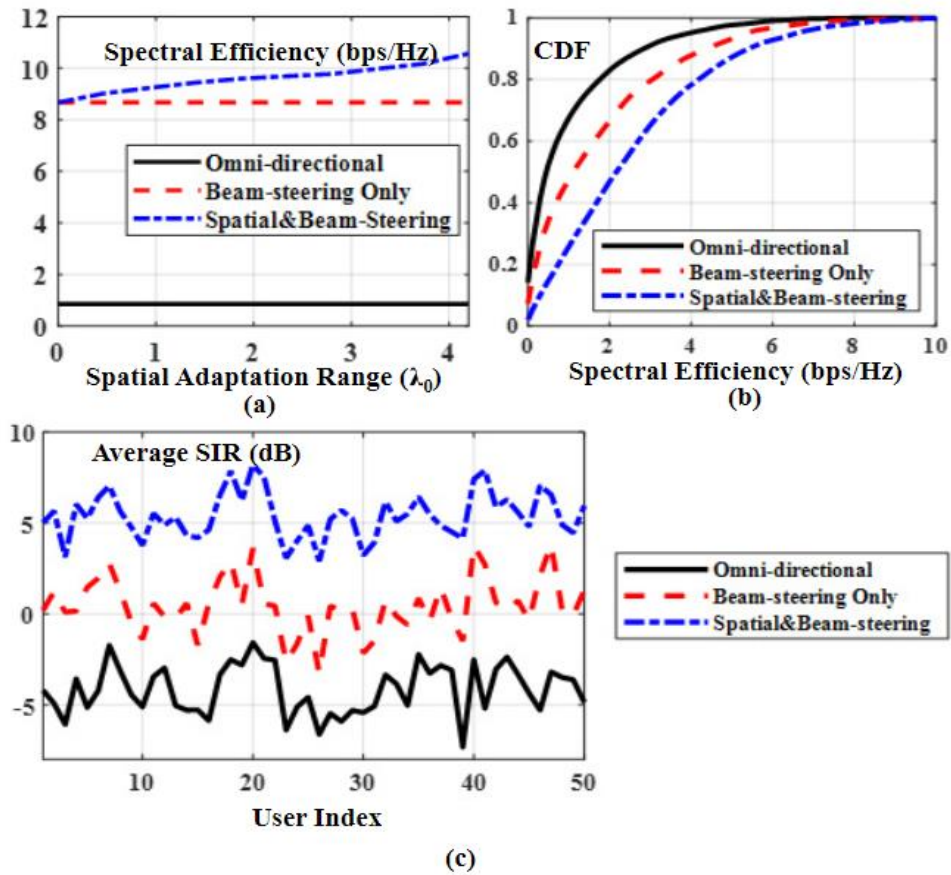
Figure 3.16: Link level simulations and spectral efficiency. (a) Link level spectral efficiency vs. spatial adaptation range; (b) Cumulative distribution of spectral efficiency in wireless network for users; (c) Instantaneous SIR values of the user in the network while MRSA ('Spatial and Beam-Steering' arrays) exhibit maximum 4.2 λ_0 spatial adaptation.

steering array (i.e., MRSA prototype in its best position closest to the feed points), and the 8-element MRSA prototype with spatial adaptation capability. MRSA increases spectral efficiency with its spatial adaptation range. For 4.2 λ_0 spatial adaption range, MRSA achieves 24% more spectral efficiency. In the wireless system simulation, 50 base stations with their attached users are spread in $200 \ m^2 \times 200 \ m^2$ area. The channel and path loss is generated based on models given in [95] while the transmit power of the base stations is considered as 30 dBm. Each base station is assumed to be selfish and maximizes the spectral efficiency of its users. The maximization algorithm calculates the spectral efficiency based on signal to interference rates (SIR) of the

available beam and spatial displacement options and selects the maximum. Thus, the algorithm does not only aim to increase the received power but also minimize interference.

Figure 3.16(b) shows the cumulative distribution of spectral efficiency for the users in the system. Equipping the base stations with the MRSAs provides a 100% gain in average spectral efficiency. The gain in system-level simulation is significantly higher than the link-level gain since MRSA provides an additional diversity for interference management. At the same time, link-level evaluation assumes no interference in the environment. Figure 3.16(c) gives instantaneous SIR values of the users, and it is seen that the proposed approach provides an average 5 dB SIR gain in the system.

A conventional approach to increasing signal level by 5 dB would be to increase the gain of the antenna array by 5 dB. From effective aperture area consideration, this would require employing 3.2× area and antenna elements. Therefore, in a full-scale implementation that will include beam-steering electronics, 3.2× antenna elements will need to be supported by corresponding electronics such as beamforming integrated circuits, RF feed networks, and bias/control lines – significantly increasing the implementation complexity. On the other hand, we show that spatial adaptation provides this improvement without increasing antenna numbers and corresponding electronics. Table 3.1 presents a comparison between the presented MRSA and the simulation only one reported in earlier work [58]. In addition, the table includes performance comparison with several conventional PAAs reported in literature [58] [96] [97] [98] [99-102]. It is observed that presented MRSA is significantly improved in assembly size and experimentally verified as compared to [58]. It is also seen that the radiation efficiency and realized gain of the MRSA is comparable to other antenna arrays. This verifies that spatial adaptation can be used as an additional degree of freedom in wireless systems.

Table 3.1: MRSA performance comparison.

Ref.	Efficiency [%]	Max. Realized Gain [dBi]	Spatial Adaptation Range	Assembly Length	Ant. Count	Avg. SIR gain
This work	84	14 Measured	4.2 λ_0	61 mm	1×8	5dB
[58]	80	11.1 ~Simulated	4.2 λ_0	105 mm	1×5	3dB
[96]	83	14.0	-	-	1×8	-
[97]	72	14.5	-	-	-	-
[98]	76.8	14.96	-	-	1×8	-
[99]	~65	21	-	-	4×8	-
[100]	50	28.4	-	-	[4×6] ×8	-
[101]	72	12.2	-	-	1×4	-
[102]	80	12.5	-	-	1×8	-

3.7 Chapter Summary

A spatially adaptive antenna array (SAA) is an electronically scanned antenna array capable of changing its physical location. This new capability allows SAA to control the wireless channel environment to increase link capacity without employing an increased number of antenna elements. Compact and cost-effective implementation of SAA requires a strategically designed RF feed network that can allow the radiating antenna elements to be repositioned. At the same time, other RF and digital electronics remain stationary. This manuscript introduces a novel RF feed network and demonstrates the first experimental verification of SAA by using microfluidic-based reconfiguration. The presented microfluidically reconfigurable SAA (MRSA) exhibits the best possible compact form - a total footprint that is approximately equal to the spatial adaptation range. MRSA operates at 28 GHz with 45 mm (4.2 λ_0) spatial adaptation capability. Evaluating MRSA in communication systems using its measured realized gain patterns shows that the wireless channel's link-level performance is improved by 24% from 8.5 bps/Hz to 10.5 bps/Hz. Additionally, spectral efficiency is improved by 100%, with a 5 dB improvement in the average signal-to-interference ratio.

Chapter 4: Mm-Wave Frequency Reconfigurable Antenna with Multilayer Integrated

Microfluidic Actuation

[2]Microfluidically reconfigurable RF devices are attractive for their compact size, low insertion loss, high radiation efficiency, and high-power handling capability. Several research groups applied microfluidics for reconfigurable antennas and RF devices. For mm-Wave applications, liquid-metal-based device realizations like the ones in [11] and [103] can potentially suffer from high conductive losses in addition to challenges associated with their packaging and long-time operation. Replacing liquid metal volumes with metalized plates that are repositionable within microfluidic channels can significantly enhance the efficiency of the devices with improved reliability.

Recent work has successfully demonstrated an mm-Wave microfluidically reconfigurable single-pole single-throw (SPST) switch with low insertion loss (0.42 dB) and wide bandwidth (>18 GHz) performance [14]. The switch is realized by constructing a microfluidic channel over a printed circuit board (PCB) that carries the stationary metallization patterns (i.e., microstrip line exhibiting gap discontinuity). A selectively metalized plate within the microfluidic channel is repositioned over the PCB layer. The vertical spacing between the selectively metalized plate and fixed metallization pattern is less than 10 µm.Consequently, overlapping the metalized plate with the metallization patterns of the PCB leads to strong capacitive coupling that can be utilized to achieve the desired SPST functionality. The switch employs a piezoelectric disk as its integrated

---

[2] This chapter was published in IEEE as reference [118]. Permission is included in Appendix B

actuator. Therefore, the switch achieves a high reconfiguration speed (1.12 ms) from a compact size.
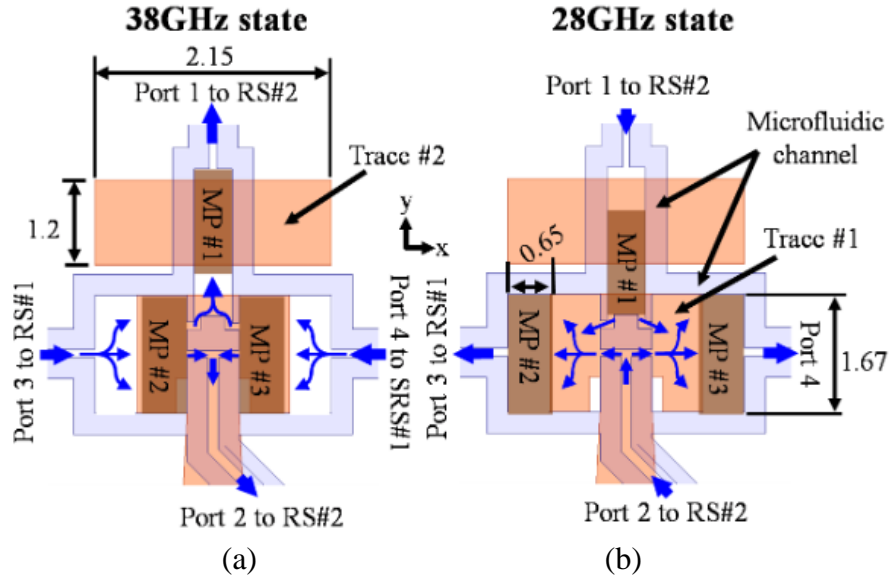

Figure 4.1: Layout view at different operating states. (a) 38 GHz: (b) 28 GHz. (all dimensions are in mm).

This paper aims to advance this recently introduced integrated actuation of the microfluidic device concept to mm-Wave frequency tunable antennas. In addition, another goal is to introduce a novel actuator that can reposition multiple metalized plates simultaneously within the microfluidic channel to achieve the desired functionality. Specifically, a microfluidically reconfigurable patch antenna that can switch its operation between 28 GHz and 38 GHz bands is presented.

4.1 Operation Principle and Design

Figure 4.1} shows the layout of the patch antenna in its two radiation states (a) and (b). Figure 4.2} shows the substrate stack up. The structure consists of two rectangular traces marked as trace #1 (1.67×2.15 mm^2) and trace #2 (1.2×3.35 mm^2). These traces are stationary and realized on the 406 μm thick Rogers RO4003C PCB ($\epsilon_r = 3.55,\ \tan\delta = 0.0027$). Traces are

separated from each with 0.43 mm in the y-direction. Trace #1 is modified with $0.15 \times 0.5\ mm^2$ slots to realize an inset feed mechanism from a 0.9 mm wide 50 Ω microstrip line.

A microfluidic channel is overlapped with these traces, as shown in Figure 4.1. The microfluidic channel contains three metalized plates, marked as MP#1, #2, and #3. The remaining volume of the channel is filled with low-loss dielectric liquid FC-40 ($\epsilon_r = 1.9$, tanδ = 0.0005) As shown in Figure 4.2}, the microfluidic channel is constructed from rigid materials as in [14] with
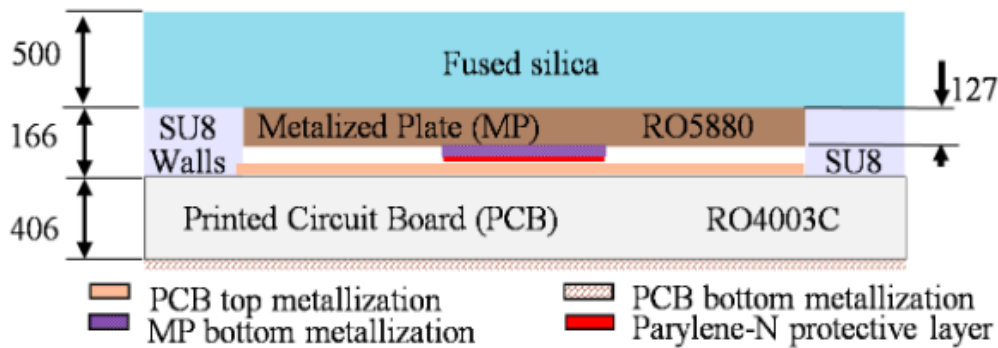

Figure 4.2: Substrate stack-up. Dimensions are in µm. All conductors are 17 µm thick.

a thickness of 170 µm. MPs are realized from 0.127 mm thick RO5880 ($\epsilon_r = 3.55$, tanδ = 0.0027). The MPs have 17 um metal thickness and are coated with 2 um Parylene-N ($\epsilon_r = 2.40$ and tanδ = 0.0006). The fabrication tolerances, as explained in [14], cause the MP and PCB and metallizations to be ~10 µm apart. Nevertheless, this spacing allows the creation of an effective RF short between the MP and PCB traces with very small overlap areas ($> 0.35\ mm^2$).

The design uses this principle to realize a frequency reconfigurable patch antenna. As shown in Figure 4.1(a), when the antenna operates at 38 GHz, MP#1 is fully overlapped with trace #2, and the remaining MPs are fully overlapped with trace #1. Consequently, trace #1 radiates like a traditional rectangular inset-fed patch antenna. To lower its radiation frequency to 28 GHz, MP#1 needs to be repositioned to capacitively load and connect traces #1 and #2 through RF shorting

principle. However, the antenna loses its impedance matching due to the extreme spacing between the 28 GHz and 38 GHz frequencies (i.e., 50 Ω to 70 Ω). Consequently, MP#2 and MP#3 need to

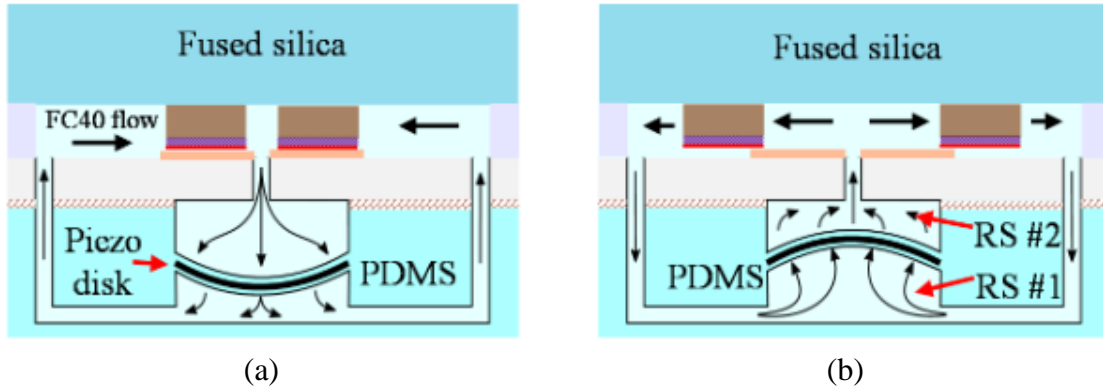(a)   (b)

Figure 4.3: Stacked PDMS actuation sequence. Swing FC40 flow for (a) OFF state and (b) ON state.

be repositioned to extend the antenna width to improve impedance matching. Figure 4.1(b) demonstrates the position of the MPs at the 28 GHz operation state.

It is essential to operate the antenna with a single actuator to achieve compact size and low cost. A piezoelectric actuator with stacked reservoirs is proposed, as shown in Figure 4.3. The reservoirs are placed at the backside of the PCB and constructed from flexible PDMS polymer. As shown in Figure 4.3(a), actuating the piezoelectric disk with proper DC voltage compresses the bottom reservoir marked as RS#1, pushing the dielectric liquid from the horizontal channels marked as RS#1 in Figure 4.1(a). Simultaneously, the top reservoir marked as RS#2 is expanded, and this causes the dielectric liquid to be pulled from vertical channels marked as RS#2 in Figure 4.1(a). The channel shapes must be appropriately selected to actuate MP#1 before letting the liquid flow out from the opposite channel end. Reversing the actuation voltage's polarity flips the reservoirs' state, as shown in Figure 4.3(b). The MPs are repositioned as shown in Figure 4.1(b). The antenna design is carried out with Ansys Electronics desktop R2 2019 with the selected substrate stack up. The total lateral dimensions of the substrates and ground plane were chosen as

$25 \times 30 \ mm^2$ to be able to fit the reservoirs. The size of the MPs is adjusted based on a parametric study for the overlap area and layout simplification. In simulations, the antenna operates with 7% and 9% $|S_{11}| <$ -10 dB impedance matching bandwidth in its 28 GHz and 38 GHz states, respectively.

4.2 Performance

The antenna prototype is shown in Figure 4.4(a). Figure 4.4(b) depicts the $|S_{11}|$ performance. The antenna is well matched for both states, with measured bandwidths of 7% and 9% at 28 and 38 GHz, respectively. Figure 4.4(c) shows the realized gain patterns of the antenna
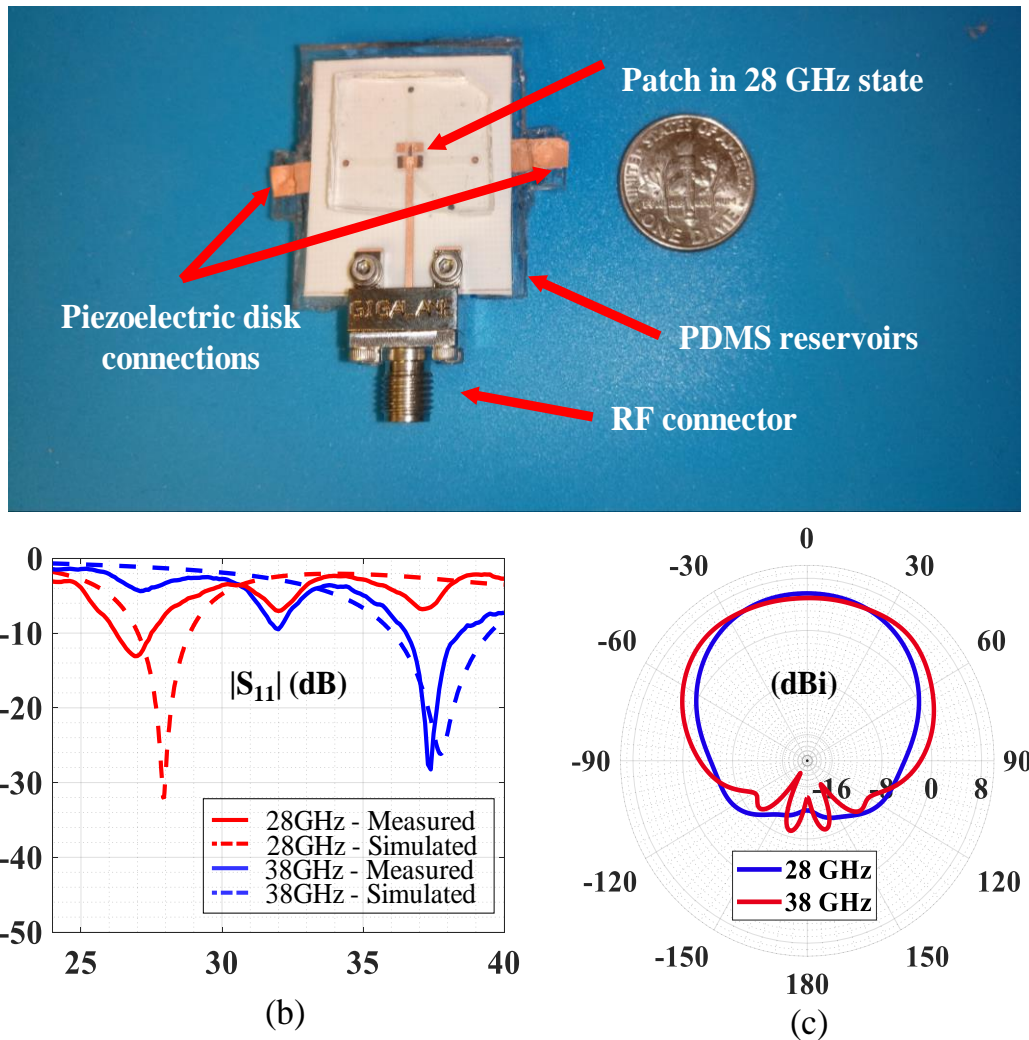

Figure 4.4: Experimental verification. (a) Prototype; (b) $|S_{11}|$; (c) Realized gain pattern.

in the H-plane at 28 and 38 GHz operation. It exhibits a realized gain of 5.6 dBi and 4.9 dBi at 28 GHz and 38 GHz, respectively. This corresponds to $> 90\%$ radiation efficiency. The H-plane half-power beam width of the antenna is136° at 38 GHz and 96° at 28 GHz.

A minimum actuation voltage of 70 V is needed to switch between the operation states. The actuation speed is estimated as approximately 100 ms based on initial experiments.

4.3 Chapter Summary

A microfluidically reconfigurable frequency tunable mm-Wave patch antenna is presented. Unlike the previously reported work on microfluidically reconfigurable RF devices, the actuation of the multiple metalized plates reconfiguring the antenna is carried out using a piezoelectric disk within a multilayered fluid reservoir stack. The antenna operates with 7% and 9% $|S_{11}| < $ -10 dB impedance matching bandwidth in its 28 GHz and 38 GHz states, respectively. Additionally, it exhibits a simulated realized gain of 5.66 dBi and 4.9 dBi at 28 GHz and 38 GHz.

Chapter 5: Microfluidically Reconfigurable Mm-Wave Slow Wave Phase Shifter

with Integrated Actuation

[3]Phase shifters (PSs) are key components of mm-Wave phased antenna arrays [104]. Low-loss PSs are essential for efficiency, whereas PSs with high power handling capability can be critical for applications such as backhauling [105]. Mm-Wave PSs in the literature are often based on CMOS [106], GaAs [107], and SiGe [108] technologies. However, their insertion losses (ILs) are high [109] with typical power handling on the order of 10 dBm. MEMS-based PSs have been reported with lower ILs (1-5 dB) [110] [111] [112] with a power handling capability $\sim$30 dBm.

More recently, microfluidics-based device reconfiguration has attracted interest due to large frequency tuning and power handling. In these devices, liquid metals [7] [8, 113] and dielectrics [9] have been introduced to the vicinity of the device to reconfigure its RF response. A microfluidics based PS [114] has relied on circulating fluids with different dielectric constants and achieved a "phase shift"/ "IL" figure of merit (FoM) of $\sim$ 9.36°/dB at 60 GHz. A recent PS [90] has also utilized dielectric property of the circulating liquid to archive 9.28 °/dB FoM at 0.9 GHz. On the other hand, utilization of liquid metals has remained much below the mm-Wave band due to the challenges associated with actuation [81] and liquid metal oxidization [9] within channels that require lossy solutions for encapsulation [115].

In contrast to liquid metals, [14, 15] have utilized an integrated actuation mechanism and selectively metallized plates (SMP) repositionable within microfluidic channels to demonstrate mm-Wave switches and tunable filters. SMP has also been used in [73] to demonstrate a

---

[3] The content of this chapter is "partially" submitted in a manuscript to IEEE and is still under review at the time.

reflection type X-band PS; but, actuation was external and actuation distance/time was large (9.5 mm / 1.95 s).

This chapter introduces a novel SMP based microfluidically reconfigurable phase shifter (MRPS) that operates at 28 GHz with integrated actuation and significantly reduced actuation time. As depicted in Figure 5.1, SMP is encapsulated inside a photolithographically manufactured microfluidic channel made of SU8 (ϵ_r = 3.25 and tanδ = 0.0270) and sealed with fused silica to capacitively and periodically load a microstrip line patterned over a printed circuit board (PCB). The separation between SMP and PCB is kept constant by coating the PCB traces with a 6 µm thick Benzocyclobutene (BCB, Cyclotene 3022-46, ϵ_r = 2.65 and tanδ = 0.002). SMP and PCB metallization overlap areas are reconfigured by repositioning the SMP using liquid FC40 (ϵ_r = 1.9, tanδ = 0.0005), which has also been used in numerous prior work due to its low viscosity and dielectric loss [116] [117]. Compression and decompression of the fluid reservoirs under the device ground plane by a piezoelectric disk is used to actuate FC40 and reconfigure the SMP. The reservoir structure is inspired by [118] actuation. The channel shape constraints SMP displacement to 100 µm, while different piezoelectric disk actuation voltages can be used to generate a continuous phase difference. Section II covers the design of the MRPS. Section III presents the prototype and measured response. Specifically, MRSP exhibits <2 dB IL at 28 GHz with a >10 dB return loss (RL). It achieves reconfiguration within 50 ms.

The device is characterized to handle 1 W of continuous RF power and is expected to handle up to 6.2 W. It operates with small deviations when subject to different orientations and vibrations. A prototype is actuated 5 million cycles without damage.
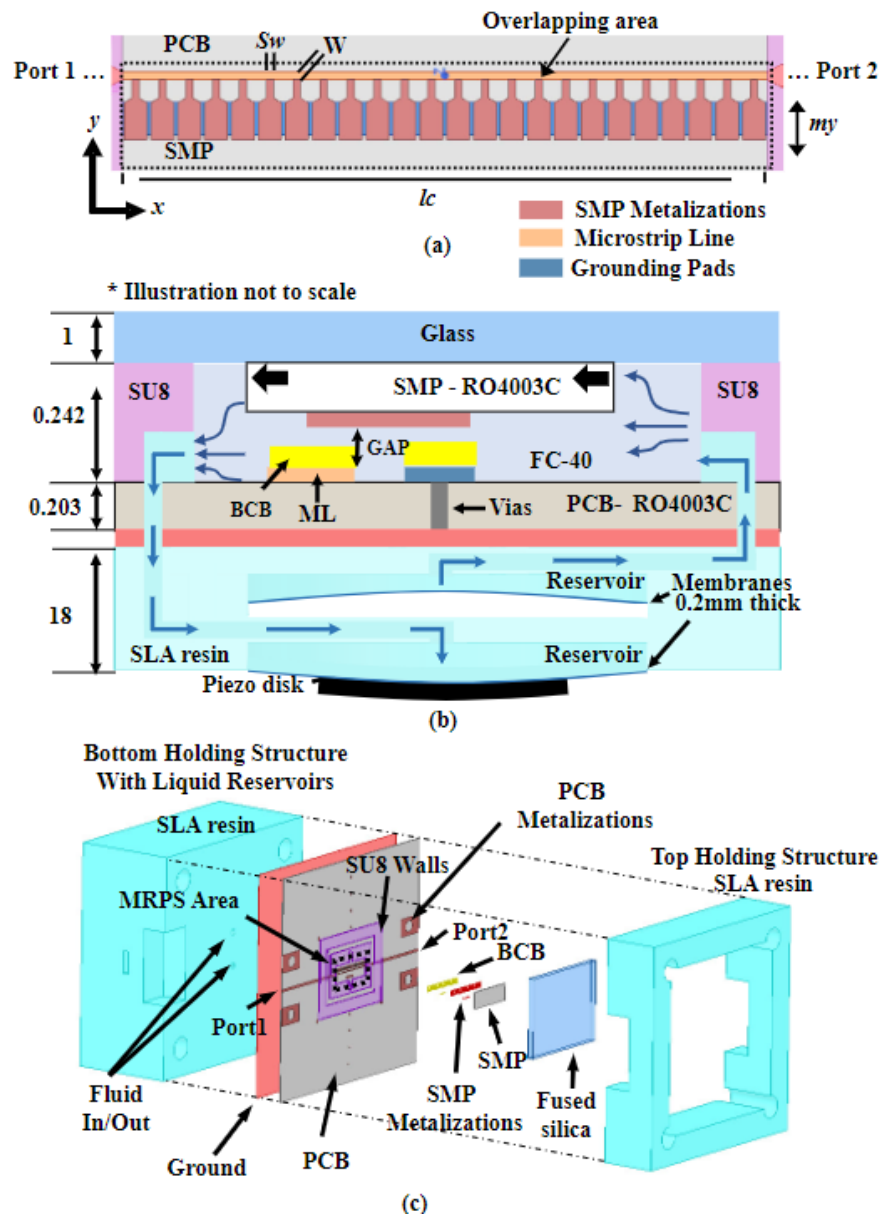
Figure 5.1: MRPS structure and operation principle. (a) Exploded view; (b) Top view of SMP and PCB metallizations; (c) Substrate stack-up and vertically stacked liquid reservoirs loaded with piezoelectric disk.

5.1 MRPS Design

The substrate stack-up is from hard materials as shown in Figure 5.1(b). 0.203 mm thick

RO4003C substrates (ϵ_r = 3.55 and tanδ = 0.0027) are utilized for both the PCB and SMP. The

sidewalls of the microfluidic channel are grown over the PCB using SU8 photoresist. Additionally,

the top seal of the channel is a 1 mm thick fused silica substrate ($\epsilon_r = 3.28$ and $\tan\delta = 0.0005$). The microfluidic channel walls are 242 μm tall. The design is initially carried out using Keysight Advanced Design System (ADS) Momentum suite with a 2D material approximation and validated in 3D by using Ansys HFSS.

The first design step is the microstrip line width. Similar to [119], the line impedance is taken high since capacitive loading will reduce its impedance. ADS's controlled impedance line tool is employed to determine the width of the line (w) as 0.12 mm for 78 Ω impedance. This implies a worst-case reflection of ≈ -10 dB when the line is terminated with 50 Ω. The line exhibits L' and C' (unit length inductance and capacitance) of 486.72 nH/m and 79.21 pF/m, respectively.

A conductive pad that is 0.5 mm wide (0.2mm larger than the diameter of the vias) and a length as long as the device is placed near the microstrip line and grounded using vias. The distance between the pad and the line is reduced (0.35 mm) in a way to avoid changes in $|S_{11}|$ of the stand-alone line at 28 GHz. PCB also includes metallizations for edge connectors and interconnect lines for measurement (50 Ω with $w = 0.42$ mm).

The next design step is concerned with the unit cell (UC). As shown in Figure 5.2, the UC consists of a microstrip line section (on PCB), a grounding pad section (on PCB), and a metallization trace (on SMP). The UC length is selected as 0.3813 mm, which is 1/15th of a guided wavelength and suggests a per unit cell line capacitance and inductance of $C = 0.0302$ pF and $L = 0.1856$ nH. The section of the SMP trace that overlaps with the microstrip line (as SMP is repositioned along the y-axis with a displacement of *my*) creates capacitive loading per UC C_{added}. Similarly, the section of the SMP trace that overlaps with the grounding pad creates another capacitive loading per UC C_{grnd}.

Using parallel plate capacitance approximation, the dimensions for the overlapping areas over the grounded traces of the PCB and the separation between PCB and SMP of 6 μm, C_{grnd} becomes 0.6257 pF. Additionally, taking into consideration that the total displacement of the SMP is limited to 0.12 mm (i.e. line width), and the width of the overlapping area is limited by 0.3 mm (to avoid mutual coupling among UCs), the maximum value of C_{added} is 0.1408 pF. The series
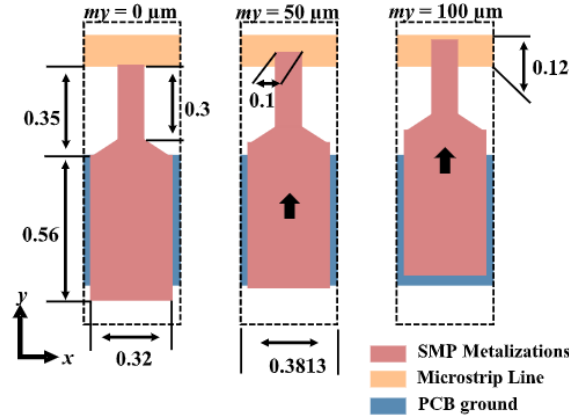

Figure 5.2: Unit cell details for different SMP positions. From left to right: 0 μm, 50 μm and 100 μm. (all dimensions are in mm).

connection of the two capacitors is the total loading, and it is therefore approximately equal to C_{added}. The capacitance and inductance per UC of the MRPS becomes $C_{uc} \approx C_{added} + C'_{line_{uc}}$ and $L_{uc} = L'_{line_{uc}}$, respectively. Note that $C_{added} \neq 0$ for $my = 0$ due to the parasitic coupling. Fitting the LC circuit model to S-parameters of the UC simulated with ADS for $my = 0$ mm position shows that $C_{uc} = 0.0363$ pF, which implies $C_{added_{min}} = 0.0061$ pF. Equation (5.1) can be used to calculate maximum C_{uc} for the desired Bragg frequency. For this design, $f_{Bragg} = 84$ GHz (i.e. 3×28 GHz) that gives $C_{uc_{max}}$ as 0.0774 pF and $C_{added_{max}}$ as 0.0472 pF.

$$C_{uc_{max}} = \frac{1}{\left(\left(f_{Bragg}\right)^2 (\pi)^2\right)(L_{uc})} \tag{5.1}$$

The following design step utilizes $C_{added_{max}}$ and $C_{added_{min}}$ in (5.2) to calculate the maximum overlapping area A as 0.01 mm^2. Assuming a square-shaped overlapping area for $C_{added_{max}}$ state, the width of the overlap area and the maximum my value become 0.1 mm as depicted in Figure 5.2.

$$A = my^2_{(max)} = \frac{\left(C'_{added(Max)} - C'_{added(Min)}\right)(d)}{(\epsilon_0 \epsilon_r)} \tag{5.2}$$

The final design step is to determine the number of UCs required to attain 360° phase shift. By using comparison (such as a cascade of 15 and 14 unit cells), the phase shift per UC is estimated as 15.2° when my is changed from 0 to 0.1 mm. Therefore, the minimum number of UCs required to achieve 360° is 24 and results in a total MRPS length l_c of 8.88 mm. The final dimensions are shown in Figure 5.1 and Figure 5.2.

5.2 MRPS Performance

The device is simulated with Ansys HFSS by including details pertaining to its 3D nature (SU8 walls, finite substrate size). Although the gap d between the SMP and PCB traces is deterministic in design as 6 µm, the fabrication tolerances place uncertainty. Therefore, parametric sweeps are also performed on d to correlate the simulated with the measured performance. The fabrication of the MRPS utilizes the process detailed in [120]. The functional footprint of the MRPS is $3 \times 8.8 \ mm^2$ while the total footprint including connectors and piezo actuation is $40 \times 45 \ mm^2$. The piezodisk utilized is a T216-A4NO-05 with a rated drive voltage of ± 180 V. The actuation use vertically stacked reservoirs for achieving compact size. The reservoirs are placed at the backside of the PCB and constructed from ANYCUBIC 3D printing UV sensitive resin using a Stereolithography (SLA) printer. The details of the reservoirs is documented in Appendix A. The larger size of the 3D printed holder allows to achieve stability in test, which may be compromised due to cable weights on connectors. The device also exhibits an internal cavity represented as the

absence of resin in Figure 5.1(c) to allow for unrestricted movement of the 3D printed inner membrane.

Figure 5.3(a) shows the $|S_{11}|$ at 28 GHz. Simulated and measured $|S_{11}|$ are well matched to 50 Ω as my is varied from 0 to 0.1 mm. Figure 5.3(b) presents $|S_{21}|$ at 28 GHz. The IL remains < 2 dB in simulated scenarios and measurements. Since simulations account for the MRPS operational area, the experimental results are compensated for connector and interconnect line losses. Figure 5.3(c) depicts phase shift performance which is sensitive to d.

The measured maximum phase shift is 305° and it is well predicted with $d = 7$ µm, which is very close to the design value of 6 µm. This fabrication accuracy issue can be resolved by adding ~5 unit cells in future prototypes. Figure 5.3(d) shows the prototype used in experimental verification, while Figure 5.3(e) shows the wideband measured response for $my = 0.1$ mm. Additionally, the phase profile vs actuation voltage with repeatability error bars is shown in Figure 5.3(f) for 20 subsequent measurements. SMP position seems to be reset with a 0 V bias. However, a negative voltage is applied in tests to ensure $my = 0$ mm is achieved.

An initial prototype was also tested for reliability. The device remained functional after continuous operation of 6 days with an actuation of 2×0.1 mm per cycle at a frequency of 10 Hz, for a total of 5 million cycles. The device speed was measured using an AmScope Microscope Digital Camera Model MU300 which has a limited resolution of 25ms between frames. The experimental setup shows total displacement in 2 frames which translates in a reconfiguration time less than 50 ms. This represents an improvement of 39× when compared against previous work in [13]. Actuation times in the order of ms could be attractive for applications requiring high power handling with low loss. Actuation time may be potentially decreased with SMP cross section and design variations.
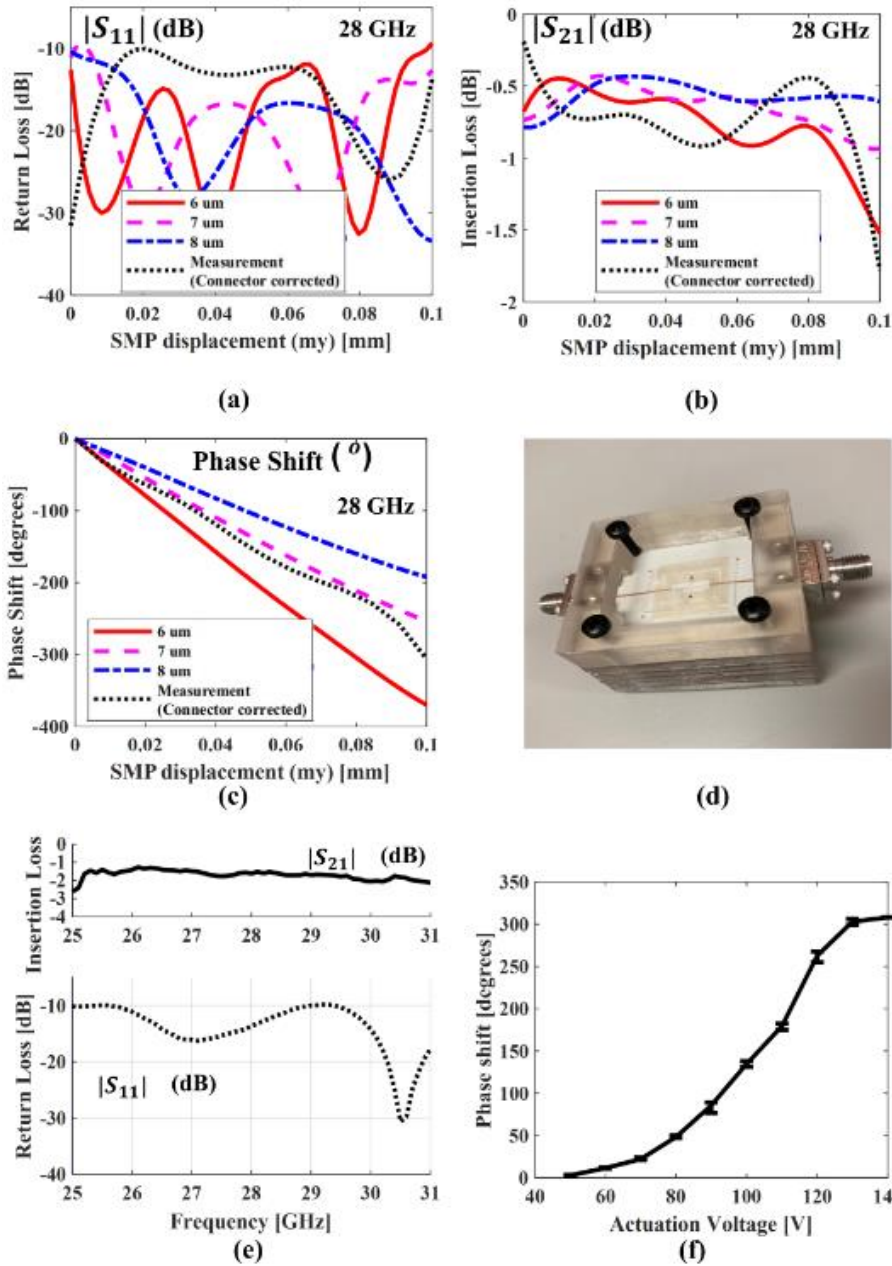
Figure 5.3: MRPS experimental verification. (a) $|S_{21}|$, (b) $|S_{11}|$, and (c) Phase shift at 28 GHz; (d) Prototype; (e) Wideband response; (f) Voltage vs Phase shift.

The effects of gravity on the device performance were studied with $|S_{21}|$, $|S_{11}|$, and phase measurements when the MRPS was facing up, down, and sideways. These resulted in 0.16 dB, 3.02 dB, and 7.73° average deviations, respectively. The results are shown in Figure 5.4 To asses power handling capabilities of the MRPS, the full-wave electromagnetic model of the phase shifter
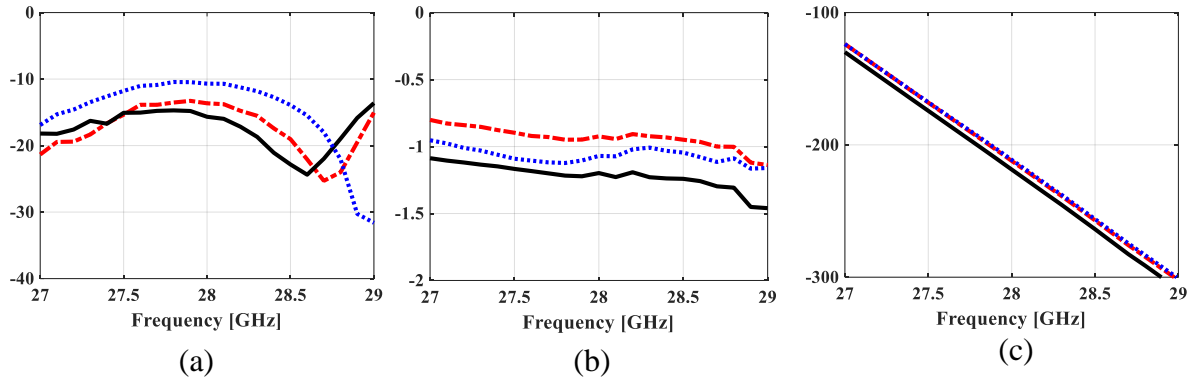
Figure 5.4: Stability for different device orientations. (Solid black = face up), (Dotted Blue = Face down), (Dashed red = vertical) - (a) $|S_{11}|$; (b) $|S_{21}|$; (c) Phase.

is imported into a Mechanical (Thermal) module on the same Ansys Electronics Desktop 2021 R1 project. The software configuration process is shown in Figure 5.5. The thermal properties of the materials utilized in the HFSS model are updated according to the values shown in Table 5.1.

Table 5.1: Thermal conductivity of MRPS materials

Material	Thermal conductivity (W/m°C)
RO4003	0.71
BCB	0.29
FC-40	0.065
Copper	401
SU8	0.2
Fused Silica	1.38

The initial temperature was set to room temperature of 20°C. The surface of the PCB, SU8 and Fused silica exposed to the air were initially set as a convection boundary with a film coefficient of 7.4 W/m2K as in [121] . The simulation predicts a temperature of 31.05 °C at the surface of the glass and 32.81 °C internal temperature when energized with 0.5 W of input power. Similarly, the simulation was performed at 1 W input power resulting in 41.51 °C of surface temperature and 46.6 °C internal temperature when energized with 1 W input power. The initial assumption in film coefficient (laminar air flow) predicts a max power handling of 5.2 W where

the temperature of the FC40 liquid reaches the boiling point detailed by the manufacturer of 155 °C. Experimental verifications of the temperature in the device are carried out using keysight thermal camera (U5855A), which has a spectral range from 8 to 14 µm and an emissivity value of 0.95. The experimental verification was performed at 0.5 W of input power and detected a surface temperature of 28.3 °C. Similarly, a temperature of 37.9 °C was detected at the surface of the glass when energized with 1 W of input power. The measurements better match simulations with a film coefficient of 10 W/m2K. Under these circumstances, the simulations predict 29.16 °C at the surface of the glass with an internal temperature of 30.31 °C under the SMP with 0.5 W of input power and 38.32 °C at the surface of the glass with an internal temperature of 40.62 °C when using 1 W input power. The expected maximum temperature the device can handle under the same test setup occurs when simulations utilize 6.2 W of input power. The resulting measurements in Figure 5.6 show a 0.6 °C error (1.7 %) when compared to simulations using 10 W/m2K and validate the expected power handling capability of the device.

Finally, Table 5.2 compares the MRPS presented in this document against recent state-of-the-art phase shifters. The presented PS has good performance with the lowest IL and highest power handling capability and best [PS]/[IL] at mm-Wave bands.

5.3 Chapter Summary

A microfluidically reconfigurable phase shifter (MRPS) with integrated actuation is presented. The presented MRPS uses a 100 µm reconfiguration distance to provide 305° of phase range at 28 GHz band. Future work will consider alternative fabrication techniques to increase the speed of MRPS and support multiple simultaneous PS actuation for application in phased antenna arrays.
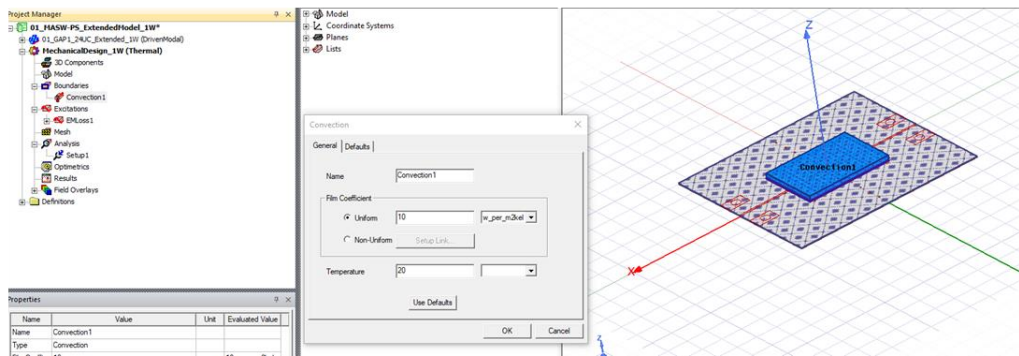
1- Insert HFSS design, create the model for EM simulations, and run the simulations.
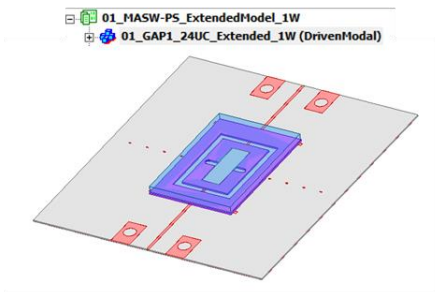
2- Insert a mechanical design, create the model for EM simulations, and run the simulations.

3- Copy the HFSS geometry into the mechanical (thermal) module and assign the boundary conditions as convection

4- Eliminate the excitation ports sheets from the thermal model and select the geometry. Assign the it as excitation EM loss. Use the last adaptative setup from the HFSS design as source solution making sure the variables are mapped by name.
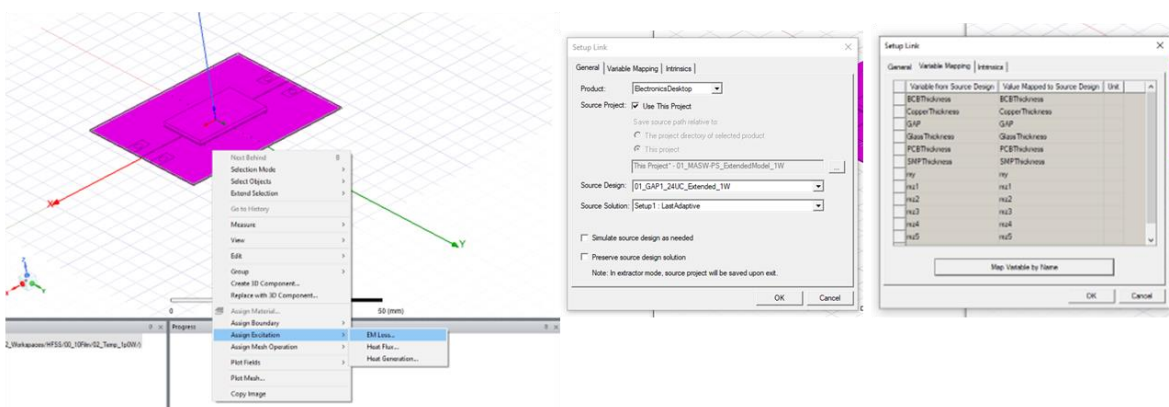
5- Final step is to create the analysis setup and import the mesh from the HFSS design (again from the last adaptative setup) and simulate
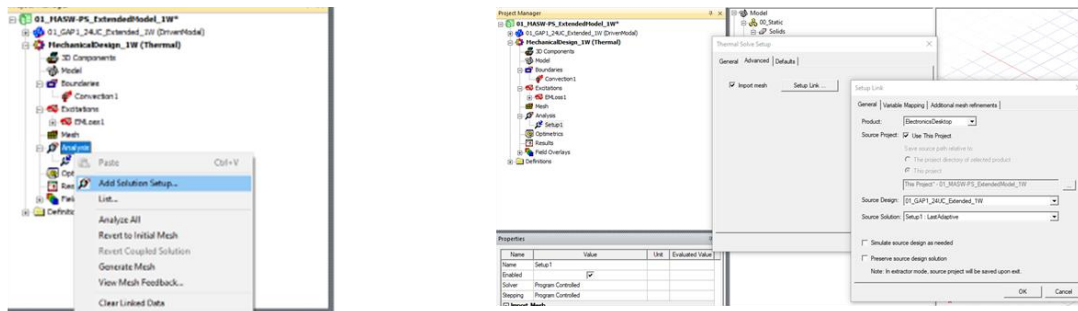

Figure 5.5: Simulation setup for power handling capability analysis.

Table 5.2: MRPS performance comparison.

Ref.	Tecnology	Frequency [GHz]	Insertion Loss [dB]	Pashe Shift [°]	FOM [°/dB]	P_{in} [mW]	Size [mm^2]
[106]	CMOS	11	8.3	360	32.72	6.5	2.06×0.58
[122]	MEMS	28	5.95	120	20.16	-	4×2.6
[123]	MEMS	25	2.34	360	153	-	-
[124]	SiGe	25	4.5	180	40	-	0.45
[125]	GaN	9	14	180	12.85	3000	5×4.7
[13]	µfl	9.5	0.95	360	379	5000	24×15
[90]	µfl	0.9	5.6	52	9.28	-	30×68
This work	µfl	28	1.8	305	170	5200-6200	8.8×3
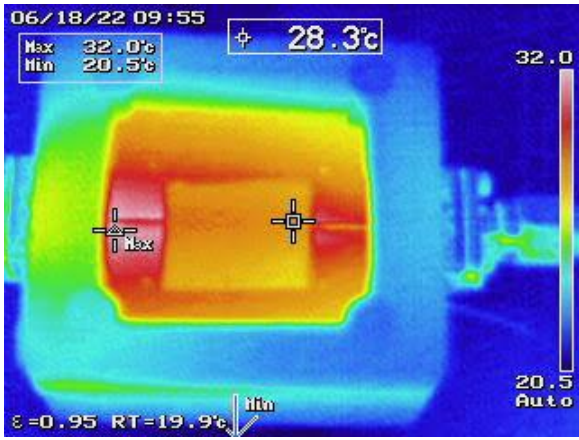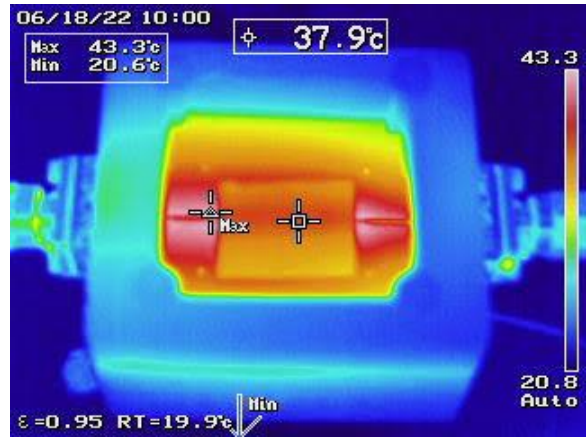
(b)   (c)

Figure 5.6: Power handling capability analysis. (a) Temperature measurement at 0.5 W; (b) Temperature measurement at 1 W

Chapter 6: Mm-Wave Beam Steering Antenna Arrays Using Microfluidically

Reconfigurable Beamforming Networks

Phased antenna arrays (PAA) are essential for mm-Wave communications [104] due to their high directivity and beam steering capability. Low-loss beamforming networks with high power handling capability become critical for applications such as backhauling [105], high-speed train-ground communication [126], and satellite communication systems [127]. Feed networks of PAAs typically employ phase shifters (PSs) that are often based on CMOS [106], GaAs [107], and SiGe [108] technologies. However, the losses in these technologies are high [109] with typical power handling being on the order of 10 dBm. Different approaches such as MEMS-based PSs have been reported with lower ILs (1-5 dB) [110] [111] [112] with power handling capability $\sim$30 dBm.

More recently, beam steering has also been demonstrated with beamforming ICs [128] [129] [130] which typically support multiple antennas with active amplification and phase shifting capabilities. The output power is typically around 10 to 15 dBm. Aside from power handling and losses, PSs are also challenging to employ due to the significant increase in hardware complexity associated with their control bits and bias lines. Therefore, alternative beam steering approaches have also been proposed to reduce complexity. For example, beamforming networks such as butler matrices can perform beam steering with only switches, but at the expense of a large device footprint and by sacrificing the precision in the scan direction. Combinations of such switched beamforming concepts (butler matrices [131] [132] and lens antenna subarrays [39, 133] with PSs

have also been considered to reduce complexity, but usually at the expense of sidelobe level performance.

Power handling capability, loss, and control complexity concerns motivated the investigation of microfluidics-based device reconfiguration as an alternative technique. In microfluidics based reconfiguration, liquid metals [7] [8] and dielectrics [9] are typically introduced to the vicinity of the device to reconfigure the RF response. However, utilization of liquid metals has challenges associated with actuation [81] and liquid metal oxidization [9]. In[115], the lossy solution of NaOH alleviates the oxidation problem but degrades the RF performance. [14, 15] have utilized an integrated actuation mechanism and selectively metallized plates (SMP) to improve actuation utilizing integrated piezo disks. SMPs have also been used in [13] to demonstrate a reflection type X-band PS; but, actuation was implemented with external and costly pumps, while reconfiguration distance/time was large (9.5 mm / 1.95 s). In [134], we have introduced a microfluidically reconfigurable slow-wave PS (MRPS) that is much more compact in size and operates at 28 GHz in mm-Wave band with integrated actuation. As compared to the reported dielectric liquid based phased shifters [9, 135], MRPS has been shown to provide a large phase shift with small IL (a figure of merit of 170°/dB as opposed to ~10°/dB), high power handling (up to 5W) and improved reconfiguration speed (50ms). However, MRPS have never been shown in operation of mm-Wave beam steering antenna arrays. To date, use of microfluidics based reconfiguration for beam steering of antenna arrays have been limited to the SMP technique and it has been solely based on switched beam techniques. [54] [82] [81] has demonstrated mm-Wave beam steering by repositioning an SMP based antenna element at the focal plane of a dielectric lens and achieved a beam scanning range of ±30°. Later on, [14] has significantly increased the reconfiguration speed by using SMP as a multi-throw switch.

This manuscript builds on the MRPS concept introduced recently in [134] to achieve beam steering in mm-Wave band with microfluidics reconfiguration. As in traditional PAAs, a microfluidically reconfigurable PAA (MRPAA) can be constructed by connecting each antenna element to an individual MRPS. However, the integrated actuation size of MRPS and the MRPS device structure (which includes the sidewalls of the microfluidic channel) make such a classical implementation very complex to achieve. Therefore, a beamforming network is proposed that is strategically designed to incorporate multiple MRPS on a single SMP while still being reconfigured by a single integrated actuation mechanism. This approach requires the SMP metallization traces corresponding to an MRPS to be different than the metallization traces of other MRPSs so that the motion of the SMP can generate a progressive phase shift to perform the beam steering functionality. Section II details the operational principle and phase shift requirements for this proposed MRPAA. Designing these customized metallization traces requires a well-established circuit model that is not available in [134]. Hence, Section III introduces a circuit model and uses it in the design of the proposed beamforming network. In addition, Section III also outlines the design of the other RF components of the MRPAA. Specifically, a $N = 4$ element 28 GHz MRPAA is designed to perform continuous beam steering in the range of $\pm 30°$ with an SMP actuation range of $\pm 100 \ \mu$m. Section IV presents fabrication details. Experimental verification provided in Section V shows that the MRPAA achieves > 5.6 dBi realized gain and reconfiguration time of 75 ms. with an expected power handling capability of 10 W.

6.1 MRPAA Operation Principle

Figure 6.1 shows the top view of the MRPAA which consists of three main design sections: 4-to-1 power divider, microfluidically reconfigurable beamforming network, and antenna elements. The antenna element spacing is taken as d = 5.4 mm which corresponds to half
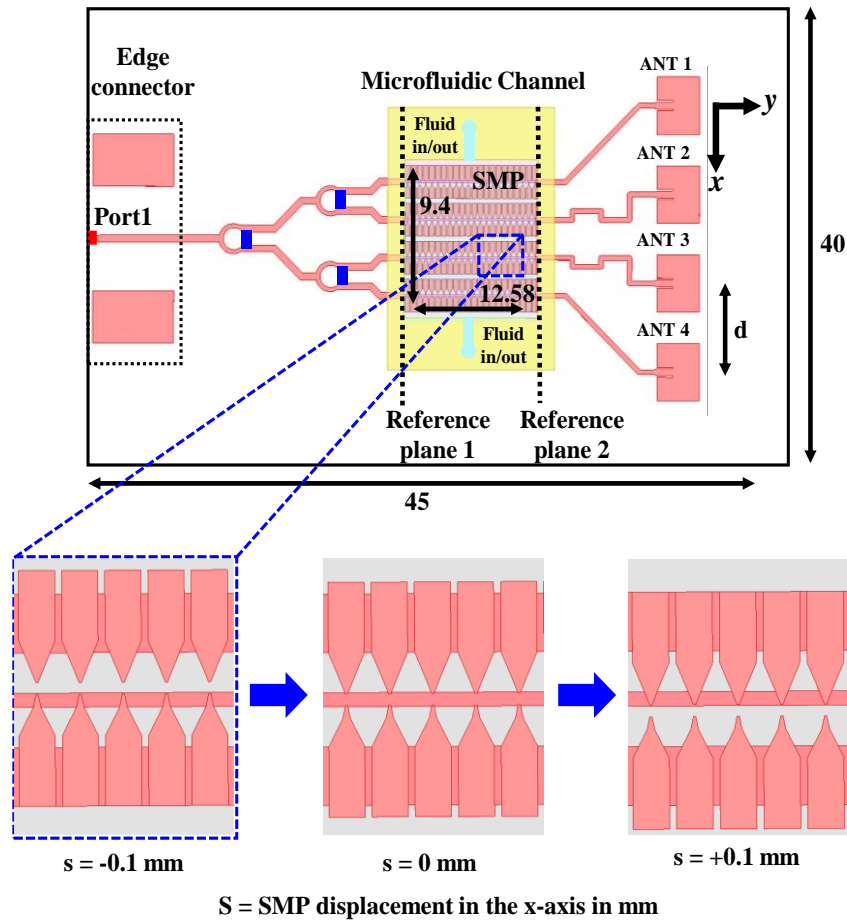
Figure 6.1: MRPAA top view and operation principle. (all dimensions are in mm).

wavelength $\lambda_0/2$ of free space at 28 GHz. Figure 6.2(a) depicts the exploded 3D view of the MRPAA. The substrate stack-up is shown in Figure 6.2(b) and it is formed from hard materials as in [120]. Microstrip lines and antenna elements are formed over a 0.203 mm thick RO4003C laminate ($\epsilon_r = 3.55$ and tan$\delta = 0.0027$) that also carries the edge connector launch. SMP is also formed over a 0.203 mm thick RO4003C laminate. SMP is encapsulated inside a photolithographically manufactured microfluidic channel made of SU8 side walls ($\epsilon_r = 3.25$ and tan$\delta = 0.0270$) and sealed with 1 mm thick fused silica ($\epsilon_r = 3.81$ and tan$\delta = 0.0002$ [109]) to capacitively and periodically load the microstrip lines patterned over the PCB. The separation
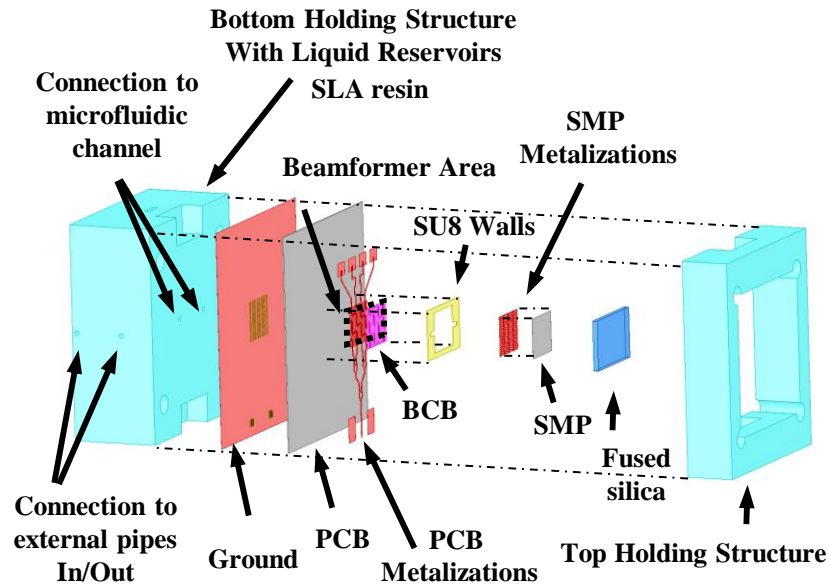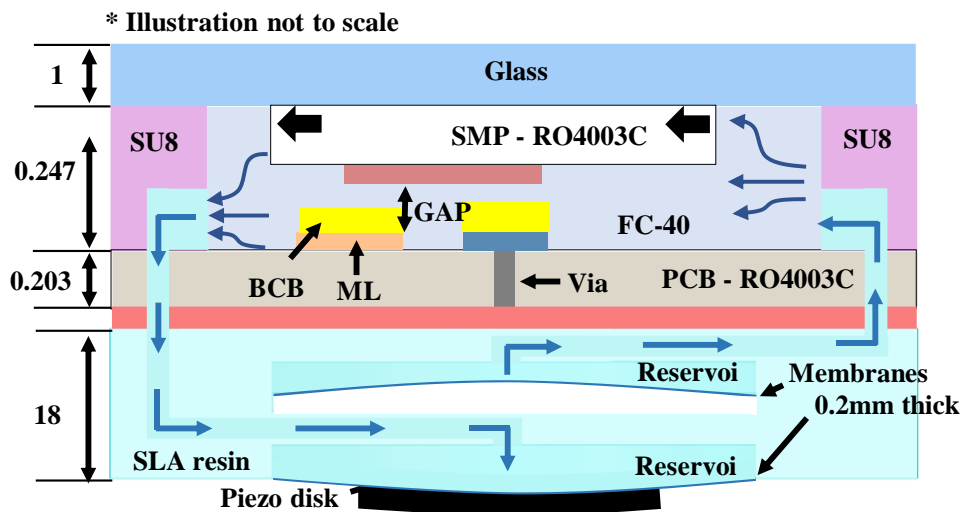
Figure 6.2: MRPAA structure. (a) Exploded view; (b) Substrate stack-up with vertically stacked liquid reservoirs loaded with piezoelectric disk (all dimensions are in mm).

between SMP and PCB is kept constant by coating the PCB traces with a 5 µm thick Benzocyclobutene (BCB, Cyclotene 3022-46, $\epsilon_r = 2.65$ and $\tan\delta = 0.002$). This coating enforces a minimum constant gap between the SMP and PCB metallizations and potentially lowers friction. Microfluidic channel walls are 242 µm in total height to accommodate 203 µm thick SMP, 17 µm thick SMP metallizations, 5 µm BCB, 17 µm thick PCB metallization, and 5 µm FC-40. FC-40

thickness is due to channel height non-uniformity in the fabrication process as previously reported by our group in [120].

SMP and PCB metallization overlap areas are reconfigured by repositioning the SMP using liquid FC40 ($\epsilon_r = 1.9$, $\tan\delta = 0.0005$), which has also been used in numerous prior works due to its low viscosity and dielectric loss [116] [117]. Compression and decompression of the fluid reservoirs under the device ground plane by a piezoelectric disk are used to actuate FC40 and reconfigure the SMP. The microfluidic channel shape constraints SMP displacement to 200 μm, while different piezoelectric disk actuation voltages can be used to generate a different SMP position within this range. The PCB also contains grounding pads parallel to the microstrip lines so that SMP traces can create a capacitive loading from the microstrip lines to the ground as in [134].

SMP motion along the x-axis changes the overlap area between the SMP metallizations and the microstrip lines. Therefore, a variable capacitive loading is realized to implement a slow-wave wave phase shifter [134]. If the motion of the SMP along x-axis relative to its reference position is denoted by s, then the MRPSs within the beamforming network should provide overall phase shifts of $\phi_n(s) = n, n \in 1,2,3,4$. Based on the coordinate system shown in Figure 6.1, the progressive phase shift of β will imply a beam steering angle of θ_s, ϕ_s that is determined from (6.1)

$$\beta = -kd \sin\theta_s \cos\phi_s \qquad (6.1)$$

where $k = 2\pi/\lambda_0$, and ϕ_s is 0 or π for steering in the $x - z$ plane, which is the H −plane of the antennas. The limit of the SMP motion range $s = s_{max}$ then determines the maximum scan angle $\theta_s = \theta_{max}$ with the phase relationship $\phi_n(s) = n$ allowing the utilization of a single SMP and actuator to perform the beam steering.

6.2 MRPAA Design

Keysight Advanced Design System (ADS) Momentum suite is employed for the design of the layout. Ansys EDT HFSS is used to verify the performance under a realistic case of finite size ground plane, substrate, and microfluidic channel walls.

6.2.1 Power Splitter.

Wilkinson power dividers are cascaded to perform the power splitting [136] [137] [138] [139]. It is implemented on the PCB with no other substrate materials on top. The divider is well matched at 28 GHz with an RL better than -15 dB and a worst-case IL of 0.5 dB above theoretical. At center frequency (28.5 GHz), the divider exhibit an RL better than -20 dB and a worst-case IL of 0.4 dB above theoretical. The physical length of quarter-wave transformers is 1.91 mm, and 100 Ω SMD resistors are CH02016-100RGFT from Vishay.

6.2.2 Beamforming Network

The design process starts with selection of desired scan range, SMP actuation range, and unloaded microstrip line impedance. Since the maximum capacitive loading per unit cell in MRPS is limited due to the Bragg frequency considerations, larger scan angles will result in a longer SMP footprint but the design process will remain the same. The design example presented in this manuscript sets θ_{max} as 35° which implies a maximum progressive phase shift β_{max} of 103°. Denoting the phase shifts of the MRPSs within the beamforming feed network at SMP reference state as $[\phi_1, \phi_2, \phi_3, \phi_4]_{\{s=0\}} = [0°, 0°, 0°, 0°]$, we pursue a design that would accomplish $[\phi_1, \phi_2, \phi_3, \phi_4]_{s=s_{max}} = [103°, 206°, 309°, 412°]$, where s denotes the SMP displacement with respect to its reference state as shown in Figure 6.1. SMP actuation range $\pm s_{max}$ is constrained to be about 80% of the microstrip line width as in [134]. Controlled impedance line tool of ADS is employed to determine the width of the microstrip line within the substrate stack-up as $w =$ mm.
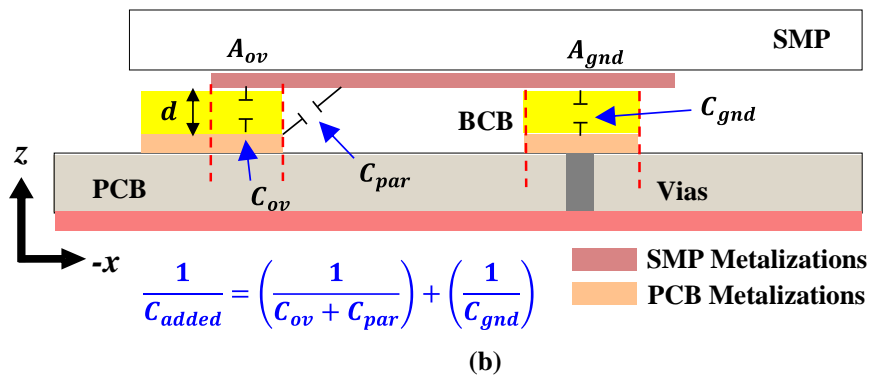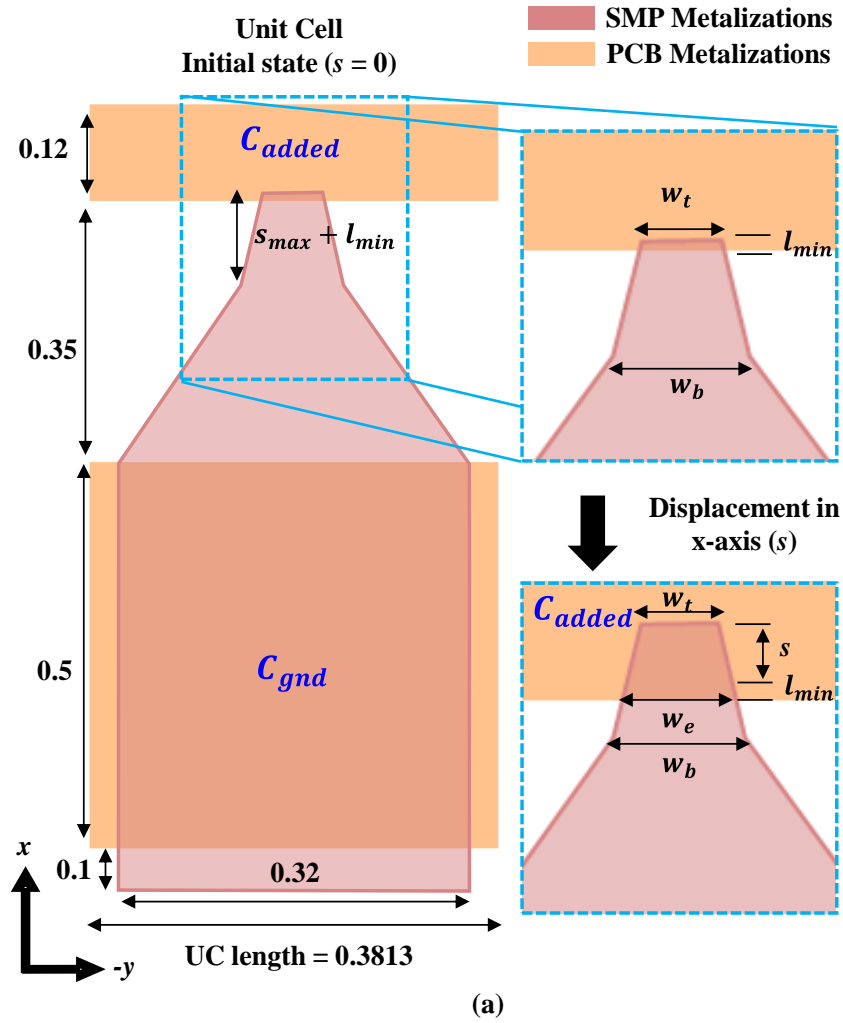
Figure 6.3: MRPAA unit cell description. (a) Layout view showing the overlapping areas (A_{ov}, A_{gnd}) defining the capacitive coupling equivalent capacitances C_{ov} and C_{gnd}; (b) Lateral view of an unit cell detailing the capacitances describing the coupling phenomena between the SMP and PCB metallizations.

This corresponds to 78 Ω characteristic impedance, which will be lowered with capacitive loading of the SMP during phase shifting. Based on the line width, $s_{max} = \pm$ μm. 78 Ω line impedance implies a worst-case reflection of ≈ -10 dB when the input/output of the line is terminated with 50 Ω. From the electrical length and impedance of the line, its L' (unit length inductance) and C' (unit length capacitance) are calculated as 486.72 nH/m and 79.21 pF/m, respectively.

The layout of the unit cell metallization is shown in Figure 6.3(a). The SMP layout consists of two main sections that overlap with different traces of the PCB, as shown in Figure 6.3(b). Overlapping area between the SMP metallization and the ground pad on the PCB (A_{gnd}) forms capacitor C_{gnd}. The ground pad is 0.5 mm wide and carries a 0.3 mm diameter via. Its length is based on the total number of unit cells, which will be determined to be 12.58 mm in the following steps of the design process. Ground pads are placed on both sides of each microstrip line. The distance between the pads and the microstrip lines is reduced to (0.35 mm) to avoid changes in $|S_{11}|$ of the stand-alone line at 28 GHz. The section of the SMP metallization that does not overlap with the PCB line and ground plane traces exhibits a capacitance to the PCB ground ranging from 0.006 pF to 0.013 pF, which is relatively small in comparison to C_{gnd} and therefore negligible to the design of the RF performance.

Repositioning the SMP over the microstrip line generates a capacitive loading on the microstrip line that can be expressed as $1/C_{added} = \left(1/\left(C_{ov} + C_{par}\right)\right) + \left(1/C_{gnd}\right)$. This variable capacitance is dependent on the overlapping area between the SMP metallization and the microstrip line on the PCB (A_{ov}) that forms the capacitor C_{ov}, the RF parasitic capacitance (C_{par}), and C_{gnd}. A_{gnd} does not change with the motion of the SMP due to SMP metallization being 0.1 mm larger than the ground pad in SMP rest (i..s $s = 0$) position. A_{gnd} is made sufficiently large

73

$(0.32 \times 0.5 \; mm^2)$ to generate $C_{gnd} = 0.6$ pF. Since C_{gnd} is significantly larger than C_{ov} (0.0007 -

0.036 pF) and C_{par} (0.0021 - 0.012 pF), C_{added} is approximated as

$$C_{added} \approx C_{ov} + C_{par} \qquad\qquad\qquad (6.2)$$

The shape of A_{ov} is selected to be trapezoidal to allow customization across the different

phase shifters of the beamforming network. At a specific SMP position, A_{ov} can be parameterized

as a function of the top (w_t) and base (w_b) widths of the trapezoid and s. Modification to w_b will

not only alter the value of C_{ov}, but the rate at which it grows as a function of s. w_t is set as 20 μm

which is the minimum reliable width that our fabrication process can tolerate. Selecting w_t as

small as possible minimizes the parasitic capacitive loading at $s = 0$ mm.

Unit Cell Circuit Model

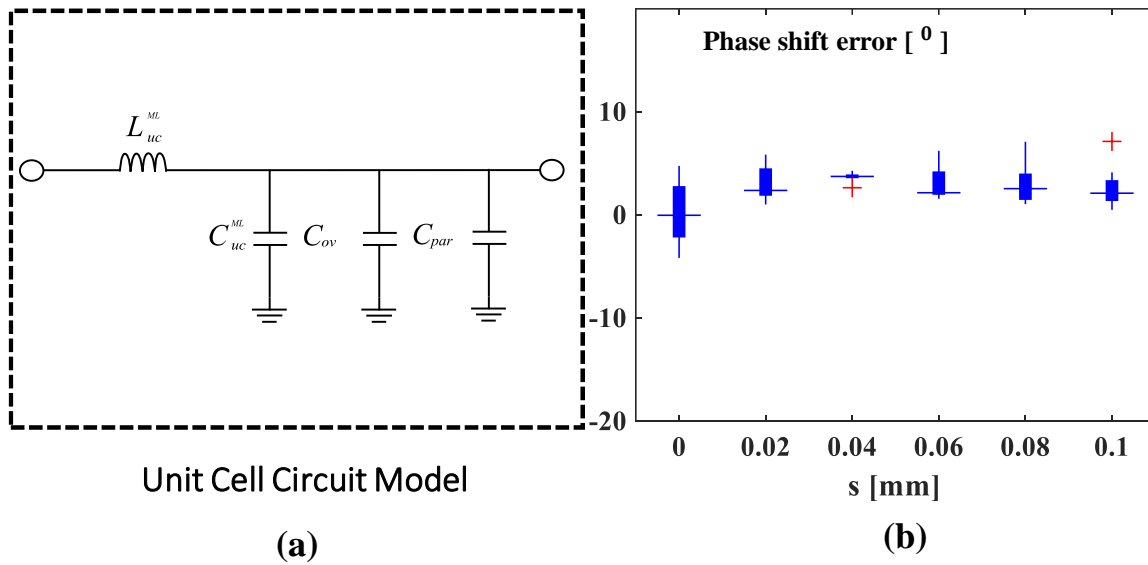**(a)**   **(b)**

Figure 6.4: Parametric circuit model describing the capacitive loading of the microstrip lines. (a) Lumped component circuit diagram; (b) Error incurred by the circuit model when predicting the phase shift per wavelength (15 UC).

The unit cell length must be first determined before carrying out the design using the circuit

model shown in Figure 6.4(a). The unit cell length can be set as 0.3813 mm which implies a $\lambda_g/15$

size (λ_g is the wavelength for the stack-up shown in Figure 6.2(b)). With this length, per unit cell

inductance L_{UC}^{ML} and capacitance C_{UC}^{ML} of the microstrip line can be determined as 0.1856 nH and

0.0302 pF. respectively. C_{ov} is related to A_{ov} as

$$C_{ov}(s, w_b) = \frac{\epsilon_r \epsilon_o}{d} [A_{ov}(s, w_e)] \tag{6.3}$$

where ϵ_o is the vacuum permittivity, ϵ_r is the relative permittivity of the BCB, and d is the

distance between the PCB traces and the metallization on the SMP (i.e. BCB thickness + gap). A_{ov}

can be expressed as

$$A_{ov}(s, w_e) = \left(\frac{w_e(s, w_b) + w_t}{2}\right)(s + l_{min}) \tag{6.4}$$

where w_e is the bottom edge of the trapezoidal area that overlaps with the microstrip line

and depends on the s and w_b. In reference state of the SMP (i.e. $s = 0$), A_{ov} is not zero due to the

$l_{min} = 10$ μm overlap as shown in Figure 6.3(a). l_{min} is useful to maintain the SMP parallel to $x -$

y plane at any position including $s = 0$. If no overlap of traces occurs, SMP may slightly tilt inside

the channel and this may prevent or slow-down the SMP motion. From the geometry, w_e can be

expressed as

$$w_e(s, w_b) = w_t + \left[\frac{(s + l_{min})(w_b - w_t)}{s_{max} + l_{min}}\right] \tag{6.5}$$

Substituting (6.5) and (6.4) into (6.3) results in

$$C_{ov}(s, w_b) = P_{01} + P_{02} + P_{03} + P_{04} + P_{05} + P_{06} \tag{6.6}$$

where

$P_{01} = 1.694 w_b$ $\qquad\qquad\qquad P_{04} = 16936988051 w_b s^2$

$P_{02} = 67.748 s$ $\qquad\qquad\qquad P_{05} = -338739.8 s^2$

$P_{03} = 338739 w_b s$ $\qquad\qquad\qquad P_{06} = 0.0071$

and the units for capacitance and length are taken in pF and m, respectively.

Modeling the parasitic capacitance C_{par} is important for the accuracy of the lumped element circuit model of the unit cell. Our recent work on a stand-alone slow-wave phase shifter in [134] showed the importance of C_{par} in modeling. However, in this recent work [134], C_{par} was constant for any SMP position due to the rectangular cross-section used in the overlap area. The trapezoidal shape of the overlap area needed to realize the proposed beamforming network concept leads to a C_{par} that is dependent on the SMP position and trapezoidal area shape, which is a direct consequence of w_e being a function of s and w_b. C_{par} can be obtained from ADS or full-wave simulations by fitting the phase response of the unit cell to the lumped element circuit model for many s and w_b combinations.

Typically, the circuit model extraction is performed with the simulation of multiple unit cells to account for mutual coupling effects, which is selected as 15 in our work corresponding to a full wavelength. This makes simulation of all w_b and s combinations time consuming to pursue a design. C_{par} can be obtained as

$$C_{par}(s, w_b) = C_{added}(s, w_b) - C_{ov}(s, w_b) \qquad (6.7)$$

where C_{added} represents the value of overall shunt capacitance added to the microstrip line section of the unit cell which is series L_{UC}^{ML} and shunt C_{UC}^{ML}. We extract C_{par} from simulations of few states of $s \in \{s_1, s_2, \dots s_Q\}$ and $w_b \in w_{b1}, w_{b2}, \dots w_{bR}$. We employ a nonlinear least-squares curve fitting approach with $s \in \{0, 0.025, 0.050, 0.075, 0.100\}$, and $w_b \in \{0, 0.05, 0.10, 0.15, 0.20\}$ obtaining a 25 element discretized set of $C_{par}(s_q, w_{br})$ from (6.7). We assume that C_{par} can be approximated with a second order quadratic equation $F(\bar{c}, s, w_b)$ as

$$C_{par} \approx F(\bar{c}, s, w_b) = c_0 + c_1 s + c_2 w_b + c_3 s w_b + c_4 s^2 w_b + c_5 s w_b^2 + c_6 s^2 + c_7 w_b^2 \qquad (6.8)$$

where $\bar{c} = [c_0, c_1, \dots, c_7]$. The nonlinear least-squares curve fitting solves for $\bar{c}$ from the minimization problem

76

$$\min_{x} \Sigma_i \left(F(\bar{c}, s_q, w_{br}) - C_{par}(s_q, w_{br}) \right)^2 \qquad (6.9)$$

Minimization problem in (6.9) is solved with MATLAB function *lsqcurvefit*. Randomly selected 80% (i.e. 20) of $C_{par}(s_q, w_{br})$ are used in solution of (6.9) and remaining 20% (i.e. 5) is used to validate (6.8). This process is repeated 10 times and phase error of 15 unit cells associated with the difference of actual $C_{par}(s_q, w_{br})$ and its prediction $F(\bar{c}, s, w_b)$ is plotted as in Figure 6.4(b). It is shown that selected second order form of $F(\bar{c}, s, w_b)$ is satisfactory with phase errors being constrained within -2.5° and 5°. If in this step, the errors are quite large, the presented procedure can be repeated with a higher order polynomial for better fit. The $\bar{c}$ values that gives the best fit are [0.0008, 103.65, 18.95, 0.0054, 0.001, 0.001, 0.0068, -0.0048], with a contributions vector (in %) $\bar{cc} = [11, 75, 14, 0, 0, 0, 0, 0]$. Therefore, our initial assumption for the model of C_{par} in (6.8) as a second order quadratic equation $F(\bar{c}, s, w_b)$ was excessive, and the system can be explained in a much more compact and simple linear equation that is detailed in (6.10).

$$C_{par} \approx 0.0016 + 103.65(s) + 18.95(w_b) \qquad (6.10)$$

where the coeficients with contributions below 0.1% are rounded to zero. Due to correct fit, we are not concerned with rounding errors.

The design continues with estimating $[w_{b1}, w_{b2}, w_{b3}, w_{b4}]$ to obtain the desired progressive phase shift $\Delta_\phi(s)$ between 4 phase shifters as $[\phi_1, \phi_2, \phi_3, \phi_4] = N_{UC}[\phi_0, \phi_0 + \Delta_\phi, \phi_0 + 2\Delta_\phi, \phi_0 + 3\Delta_\phi]$, where $\phi_0(s) = \phi_1(s)/N_{UC}$ represents the phase delay of the unit cell of the first phase shifter and $\phi_1(0) = \phi_2(0) = \phi_3(0) = \phi_4(0)$ is approximately satisfied due to the identical usage of w_t in design of all phase shifters. In our design process, we first set w_{b1} as 0.02 mm, which is same as w_t resulting in $\phi_0(s_{max})$ =-32.01°. Next we set w_{b4} as 0.16 mm which provides a $C_{added} = 0.0472$ pF at s_{max} and maintains the Bragg frequency above 80 GHz as used in our

recent work [134]. This results in $\phi_0(s_{max}) + 3\Delta_\phi(s_{max}) = $ -42.09°. $\Delta_\phi(s_{max})$ is therefore calculated as 3.36°. as a result, the desired $[\phi_1, \phi_2, \phi_3, \phi_4]/N_{UC}$ at s_{max} is then estimated as [-32.01°,-35.37°,-38.73°,-42.09°]. To facilitate the selection of w_{b2} and w_{b3} that will result in $\phi_2(s_{max})$ =-35.37° and $\phi_3(s_{max})$ =-38.73°, the circuit model is utilized to generate a phase surface plot of the unit cell using (6.10) with s and w_b sampled in 0.01 mm steps (see Figure 6.5(a)). From this surface plot, w_{b2} and w_{b3} are found as 0.065 mm and 0.110 mm, respectively. The number of unit cells N_{UC} required to get a maximum progressive phase shift of 103° is calculated as $103°/\Delta_\phi(s_{max}) = 31$. A safety margin of 2 unit cells is also introduced into the ```design to accommodate for the maximum phase error observed for the model ($\pm 5° \approx 2\Delta_\phi$) in Figure 6.4(b).

The simulated phase of the circuit model of 33 UC for different s using $[w_{b1}, w_{b2}, w_{b3}, w_{b4}]$ =[0.02,0.065,0.11,0.16] mm is presented in Figure 6.5(b) (solid lines). The simulated values are then compared against ideal response (dotted lines) and show a small error between 2° to 5° in PS3 and PS4.

The figure shows that progressive phase delay is not a linear function of s, This is due to the trapezoidal shape selected for A_{ov}. Selecting a different shape such as a trapezoid with non linear edges can be investigated in future to achieve linearity in this response. The layout implemented in the comparison is shown in Figure 6.5(c), showcasing the unit cells of four phase shifters each using the w_b values determined in the previous section. Additionally, Figure 6.5(d) and Figure 6.5(e) show $|S_{11}| < $ -10 dB and $|S_{21}| > 1.7$ dB for all phase shifters. For scanning in both $\phi_s = 0$ and π elevation cuts, the SMP metallizations are mirrored and placed into the other side of microstrip lines. Therefore, a single actuator becomes satisfactory due to simultaneous actuation of all unit cells s is varied from -0.1 to 0.1 mm. This results in the final SMP metallization
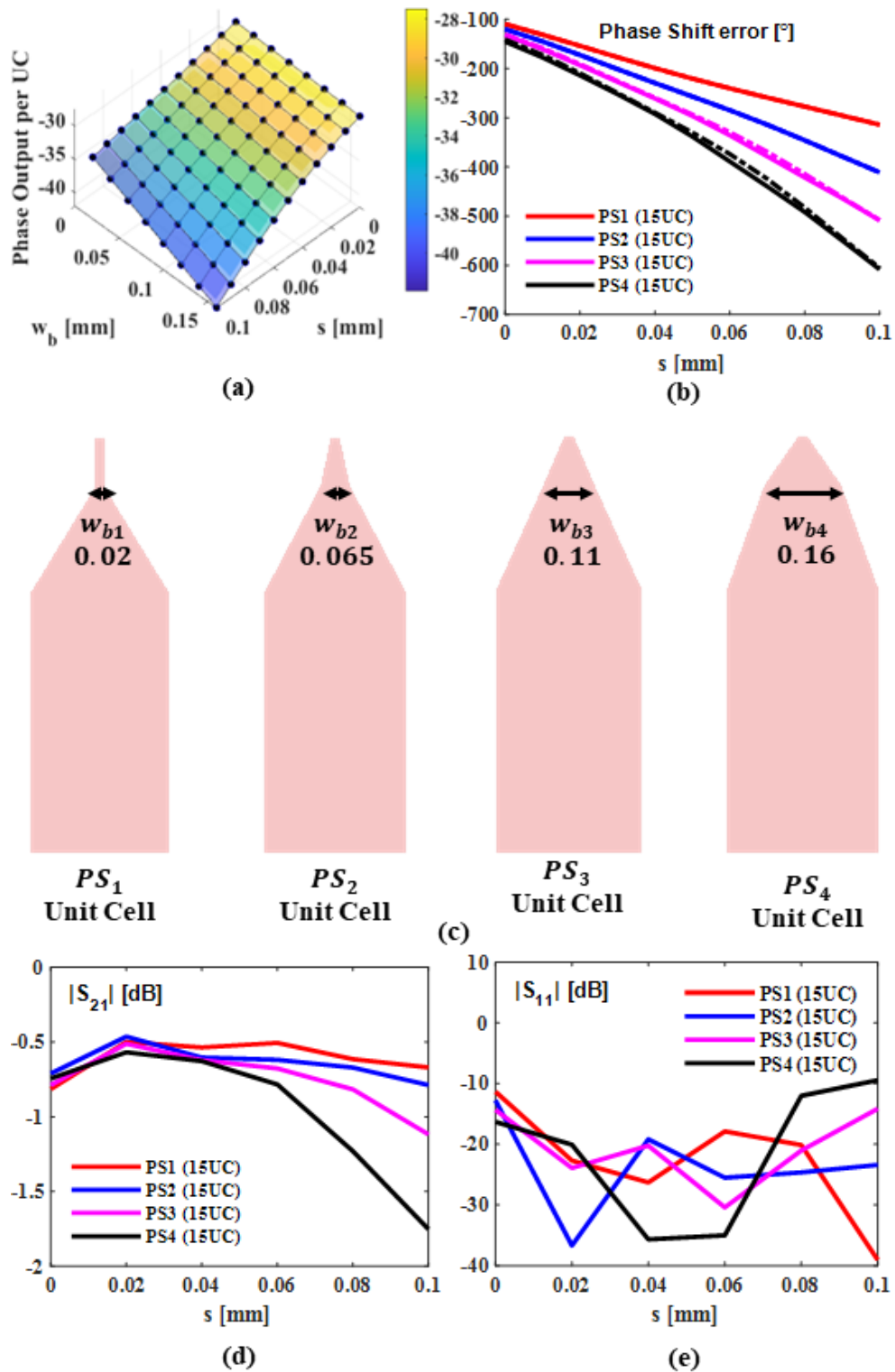
Figure 6.5: Selection of w_b per phase shitfer. (a) Surface plot of unit cell phase as a function of w_b and s using $w_t = 0.02$mm; (b) Phase shift of 33 cascaded UC using the circuit model (solid lines) vs ideal response (dotted lines); (c) Layout top view of the unit cell SMP metallizations for $PS[1,2,3,4]$; (d) Simulated $|S_{11}|$ for $PS[1,2,3,4]$ using 33 UC; (e) Simulated $|S_{21}|$ for $PS[1,2,3,4]$ using 33 UC. (all dimensions are in mm)

layout shown in Figure 6.6(a). Figure 6.6(b) shows the $|S_{11}|$ of each double-sided phase shifter at 28 GHz, which is well-matched to 50 Ω.

Figure 6.6(c) presents $|S_{21}|$ for each double-sided phase shifter at 28 GHz. The IL remains < 1.5 dB in simulated scenarios. Additionally, Figure 6.6(d) shows the phase response of all phase shifters as s changes from -100 µm to 100 µm. The additional loading caused by introducing the mirrored metallizations increases the simulation (solid lines) vs ideal phase response (dotted lines) error previously shown in Figure 6.5(b) by 25° at s_{max}. This discrepancy is related to the loading / unloading of the metallized plates for $s = \pm 0.01$ mm range. For instance, as s reconfigures from 0 to 0.01, one side of the metallization loads the line while the other side of the metallizations unloads the line.

6.2.3 Antenna Elements

The patch antenna element of the array has a footprint of $2.68 \times 3.5\ mm^2$ and resonates at 28 GHz in simulations with a 700 MHz of $|S_{11}| < $ -10 dB bandwidth, 4.05 dB realized broadside gain with 80° half power beam width (HPBW) in the H-plane. The inter-element separation of the array is $\lambda_0/2 = 5.4$ mm. The layout of the antennas is shown in Figure 6.7(a). The broadside realized gain of the stand-alone array is 11.55 dBi and exhibits a half-power beamwidth of 22˚. To compare beamformer simulations against ideal response, the antenna array is fed with both simulated and ideal phase shift from the beamformer section at $s = 0.1$ mm (which is the worst case error in Figure 6.6(d)). The comparison is presented in Figure 6.7(b), where the error incurred by mirroring degrades the maximum scan (at s_{max}) by 5° (Dotted line) when compared against the same antenna array feed ideally (Solid line). The final layout of the MRPAA (which integrates the power splitter section, the beamforming network section, and the antenna elements) is presented in Figure 6.1.
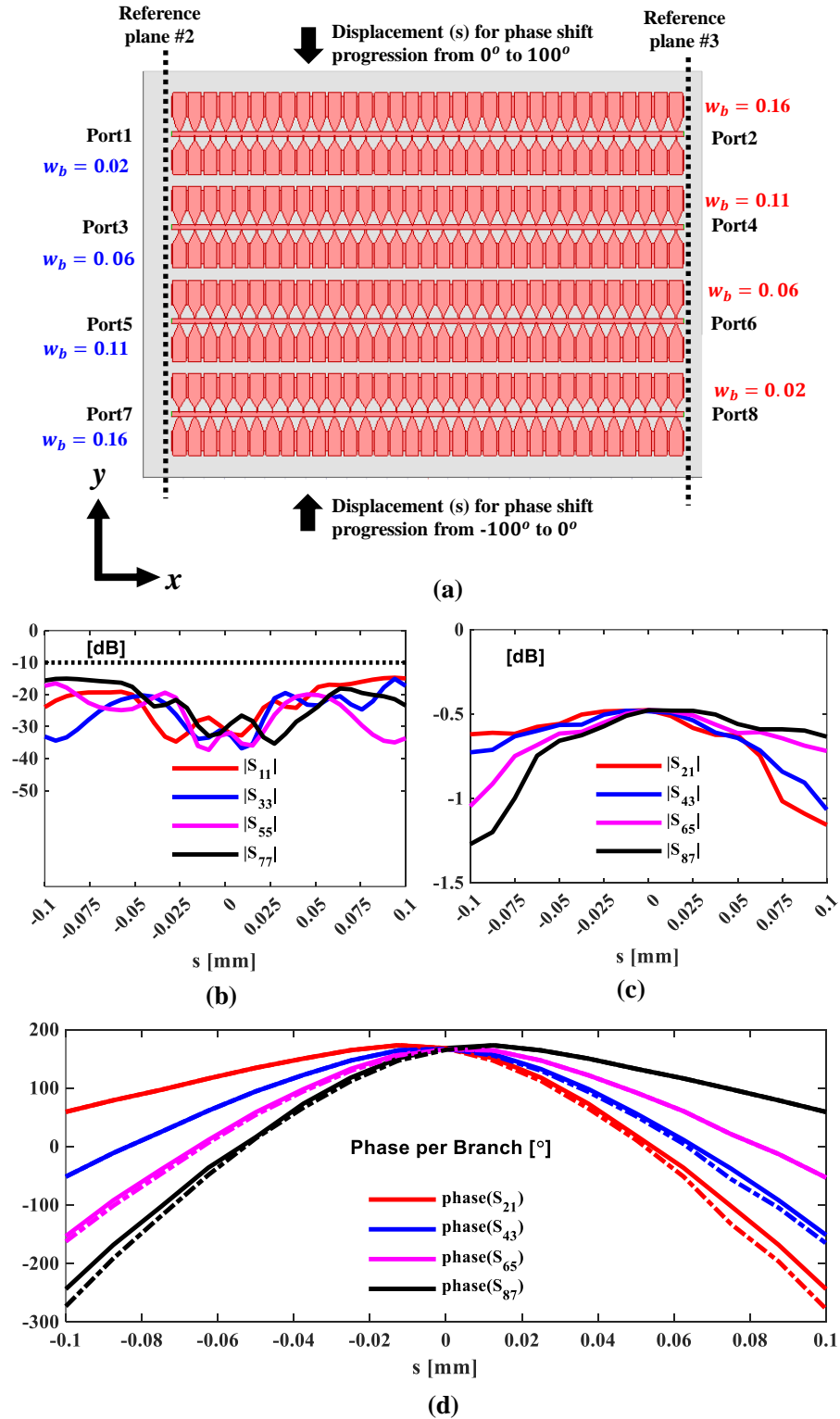
Figure 6.6: Beamformer layout with mirrored SMP metallizations. (a) Layout view of the complete beamformer; (b) Reflection coeficient for each PS; (c) Transmission coeficients for each PS; (d) phase shift of the beamformer between ref planes #2 and #3 for each PS (solid lines) compared against ideal response (dotted lines). (all dimensions are in mm).
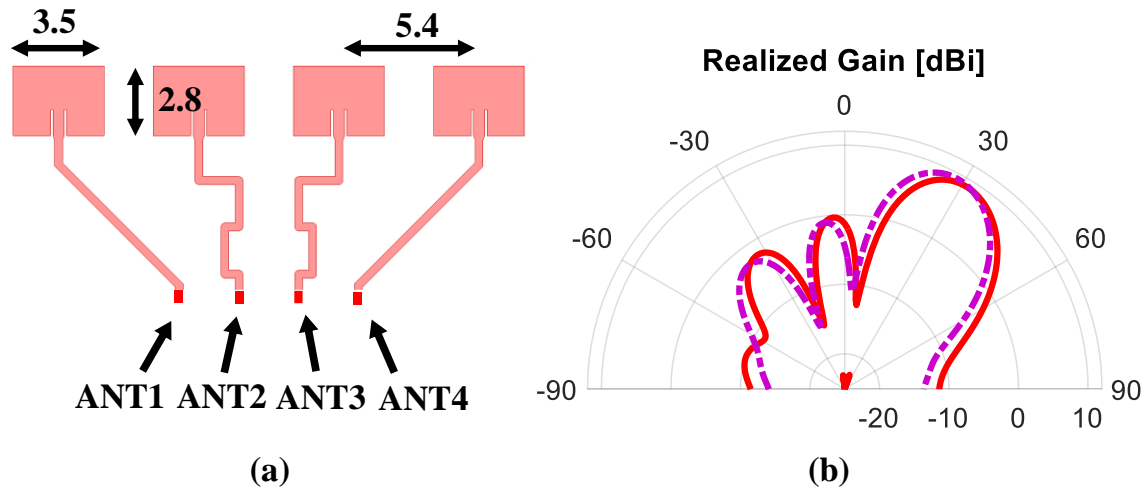
Figure 6.7: Stand-alone antenna array. (a) Layout (top view); (b) Antenna array gain over isotropic using simulated phase shift $\Delta_{\phi[1,2,3,4]\$}$

The total footprint area is $40\times45~mm^2$, including the RF edge connector. The entire layout is simulated in Ansys HFSS, and results are used to compare against measurements in the following sections.

6.3 Fabrication

The PCB and SMP are patterned using standard photolithography techniques; hence, these details are omitted for brevity. The microfluidic channel sidewalls are constructed with photoresist SU8-2075. The 0.203 mm thick PCB is first bonded with a 2 mm thick structural substrate to eliminate the process variations due to RO4003C flexibility. Subsequently, it is spin-coated with a 242 µm thick layer of SU8 in two spin-coating steps. First, a SU8 layer is spin-coated at 1500 rpm for 45 s and soft baked for 25 min at 95 °C. The second SU8 layer is spin-coated at 1500 rpm for 45 s and then soft baked for 45 min at 95 °C. The spin-coating process is followed by a 400 mJ/cm2 UV exposure and three steps of post-exposure baking profile. The first section of the baking profile keeps the PCB at 60 °C for 7 min. The second step ramps the temperature up to 90 °C in 20 min. The final step cools down the PCB to room temperature in 6 hours. As previously

82

established in[120], the application of multiple SU8 coatings and the utilized temperature profile reduces the deformation of the SU8 walls and prevents high deviations of the gap between the SMP and the PCB traces. This step is followed by the preparation of microfluidic channel walls using SU-8 developer and rinsing of the PCB substrate.

The channel sidewalls are bonded with the fused silica using the adhesive bonding technique described in [120]. Once the channel is sealed, a fluid circulator structure is 3D printed and attached to the bottom side of the PCB + structural substrate. The actuation is similar to [14] using vertically stacked reservoirs for achieving compact size. However. The reservoirs in this investigation are placed at the backside of the PCB in a stacked configuration and constructed from ANYCUBIC 3D printing UV sensitive resin using a Stereolithography (SLA) printer. The final prototype is shown in Figure 6.8(a), where the structural top fixture (used to reduce device deformation during handling) is separated to facilitate the visualization of its components. Figure 6.8(b) shows the setup utilized to characterize the realized gain of the prototype.

The reason for the larger size of the 3D printed holder is to achieve stability during testing, which may be compromised due to cable weights on connectors. As shown in Figure 6.2(b),
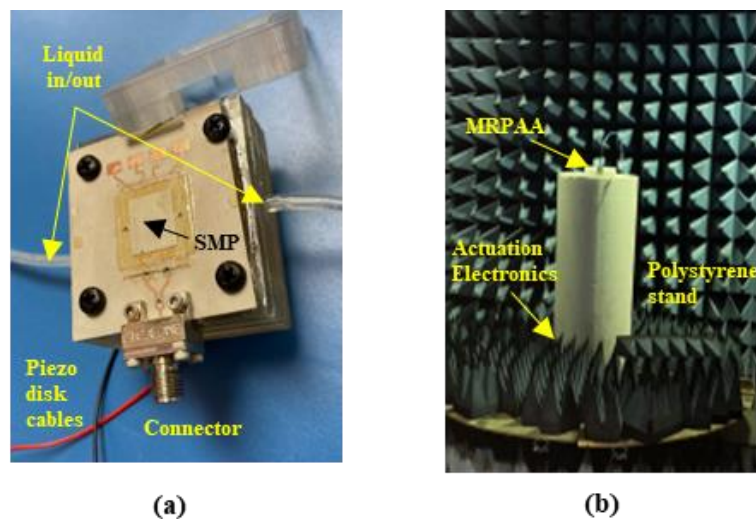

Figure 6.8: MRPAA prototype and test setup. (a) Open top view of the MRPAA; (b) Realized gain experimental validation setup.

actuating the piezoelectric disk compresses/decompress the bottom reservoir and circulates the dielectric liquid. Reversing the polarity of the actuation voltage flips the state of the reservoirs and, therefore, the position of the SMP between -100 μm and 100 μm. The device also exhibits an internal cavity represented as the absence of resin in Figure 6.2(a) to allow for free movement of the inner membrane. The reconfigurable footprint of the MRPAA is 8.38×9.64 mm^2 while the total footprint including connectors and piezo actuation is 40×45 mm^2. The piezodisk utilized is a T216-A4NO-05 with a rated drive voltage of ±180 V.

6.4 Experimental Verification

Reconfiguration speed of the prototype is characterized using an AmScope Microscope Digital Camera Model MU300 which has a limited resolution of 25ms between frames. Applying 160 V_{pk} to the piezo disk enforces an SMP speed of total displacement (0.2 mm) in 3 frames which translates in a reconfiguration time less than 75 ms. This represents an improvement of 40× when compared against previous work such as [13]. This result is consistent to the findings from previous works on microfluidically actuated devices from our group utilizing metallized plate with similar cross section and half the displacement. The lowest voltage at the piezo required to actuate the plate is 50 V_{pk}.

Fig 6.9(a) shows the simulated $|S_{11}|$ of the MRPAA. The simulations predict match at the resonating frequency of the patch antennas (28.5 GHz) for $s =$ [-100,-75,-50,-25,0,25,50,75,100]. Fig 6.9(b) shows the resulting measured $|S_{11}|$ of the prototype vs frequency for the extreme cases of minimum loading ($s = 0$ mm) and max loading. $|S_{11}|$ is well matched to 50 Ω as s is varied from -0.1 to 0.1 mm from 27.5 GHz up to 29 GHz. Fig 6.9(c) shows the experimental verification results of the realized gain of the MRPAA prototype at three states of the array ($s_{max}, s_0, -s_{max}$). The data included in the set correspond to H-plane beam scanning only and has been compensated
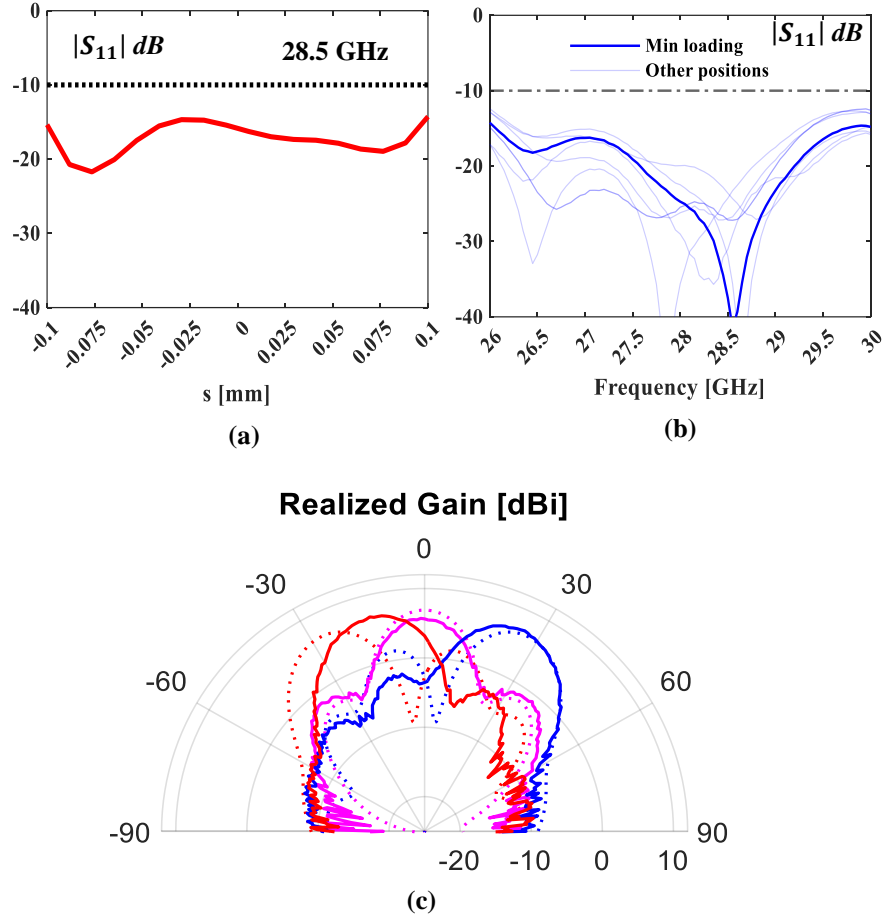
Figure 6.9: MRPAA prototype performance. (a) Simulated $|S_{11}|$ at 28.5 GHz (antenna resonance) as function of s; (b) Measured $|S_{11}|$ vs frequency showing match at 28 GHz band for several loading positions; (c) Measured vs simulated realized gain at 28.5 GHz.

for connector loss. The measured realized gain is 6.8 dBi for the extreme case of beam scanning angle is 30°. It becomes 5.6 dBi when the beam is scanned towards 0°. Similar to the previous work in [120], the large ground plane size in E-plane causes pattern ripples and tilting, causing the broadside gain in H-plane to appear lower. The loss in broadside gain is also increased by distortions in Δ_ϕ near $s = 0$ mm. Fabrication errors in the SMP metallizations and alignment of the plate might be the main cause for increasing this distortion in the array factor by altering Δ_ϕ among the PS. As s changes toward the edges, the Δ_ϕ exits the transition zone and better resemble ideal array factor, showing higher gain.

Fabricated prototype has a measured scan range between -20° to 30°. The gap between expected -30° to measured -20° beam angle at max actuation can be related to fabrication errors associated with over etching, photolithography process misalignment and/or SMP dicing resolutions. The missing 10° scan range corresponds to a state of s = -70 µm instead of -100 µm. Nevertheless, the measurements proves the proposed beamforming network concept and the design procedure followed to achieve progressive phase shift.

It is important to note that the pattern measurement of MRPAA tuned out to be quite challenging due SMP dragging issue within the microfluidic channel. This makes near impossible to fix the position of the SMP over long periods of time. The dragging causes the SMP to shift its position after which is needed for anechoic chamber measurements. A frequent reset of the SMP position was necessary to relocate the SMP to its desired location. The longest time a position was sustained in the lab was 70 seconds, after which, an air bubble relocated inside from the reservoirs to the SU8 walls and the SMP started shifting. Because of this, we can conclude that this shift in the position is most likely caused by the presence of air bubbles inside of the reservoirs due to their cylindrical shape. This constrain has also been observed in a minor degree on previous work on MRPS [134], where the phase profile vs actuation voltage with repeatability error bars was obtained using a signal generator with 50% duty cycle at 0.5Hz frequency, therefore resetting the state of the SMP once every 2 seconds. On the contrary, the realized pattern measurements in this work take a long time to obtain (>2 hrs), giving opportunity for the SMP to drift over time from its position.

The prototype was also tested for reliability, remaining operative after continuous operation of 10 days with actuation of 2×0.2 mm per cycle at a frequency of 10 Hz, for a total of 9 million cycles. The device has been characterized for power handling capabilities up to 1 W

(with 1 W representing the maximum RF power achievable in our lab at the time). Thermal camera measurements at 1 W show an average glass surface temperature of 25.3 °C vs 27.01 °C in simulations utilizing a uniform film coefficient of 20 W/(m2K) at the convection boundary, giving a simulated internal temperature of 28.6 °C. The simulations predict a maximum power handling capability of 15 W under the same test conditions, where the simulated internal temperature reaches the boiling point for the FC-40 liquid. The thermal camera measurements are shown in Figure 6.10.
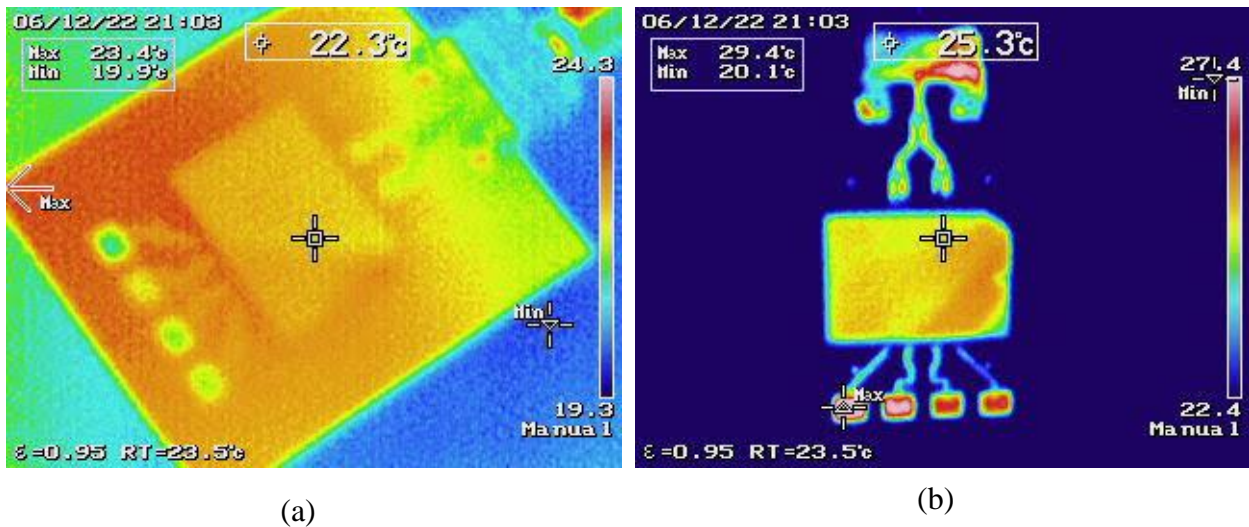
Figure 6.10: Power handling capability analysis. (a) Temperature measurement at 0.5 W; (b) Temperature measurement at 1 W.

Finally, Table 6.1 compares the MRPAA presented in this document against recent state-of-the-art radiation pattern reconfigurable antenna arrays utilizing beamformers. The table shows that the presented MRPAA has good performance with the lowest hardware components complexity between equivalent architectures, better power handling capabilities based on our previous study on capacitively-loaded phase shifters and to the first of our knowledge, the first Microfluidically actuated phased antenna array at mm-Wave bands.

Table 6.1: MRPAA performance comparison.

Ref.	Frequency [GHz]	# Elements	Peak Gain. (dBi)	Phase Resolution [°]	# of actuators	Power [mW]
This work	28s	1×4	6.8	-	1	10000
[140]	5	1×4	9.0	& 0.35	1.6	-
[141]	5.5	1×4	11.16	5.6	4	-
[142]	25	1×4	9.0	-	4	-
[143]	5.8	1×4	8	-	2	-
[144]	1	2×2	12.1	31.25	4	38.6
[145]	28	4×4	-	10	4	2800
[146]	28	4×4	-	-	4	2020

6.5 Chapter Summary

This paper demonstrated a Microfluidically Reconfigurable Phased Antenna Array (MRPAA) operating at 28 GHz. The presented MRPAA exhibits integrated actuation utilizing novel 3D printed circulators as an alternative to PDMS circulators. The MRPAA exhibits a 200 μm reconfiguration, and it is matched to 50 Ω for the entire reconfiguration range at 28 GHz. MPAA also exhibits 5.6 dBi realized broadside gain when the SMP is positioned in the minimum capacitive loading ($s = 0$ mm), with canning range [-20°,30°] in the H-plane as the SMP is repositioned inside the microfluidic channel. Future work will consider improvements in design and fabrication processes to extend the scan range. In addition, application to 2D beam steering will also be investigated.

Chapter 7: Final Remarks and Overview of Future Work

This dissertation has demonstrated multiple examples of microfluidics based reconfiguration techniques applied to realization of millimeter-wave reconfigurable antennas. Their design and operation have been demonstrated with successful experimental verifications. More specifically, microfluidic actuation of selectively metalized plates (SMP) has been utilized to introduce novel frequency reconfigurable antennas, spatially adaptive antenna arrays, and radiation pattern reconfigurable antenn arrays (beam steering) operating within mm-Wave frequencies. All antennas have been operated with a single actuator to minimize complexity of the device, which was enabled through creative design approaches that took advantage of the "selective" metallizations of the SMP.

Microfluidically actuated spatially adaptive antenna array (MRSA) has been shown to be capable of controlling mm-Wave wireless channel by changing its physical location within a compact footprint. Thanks to its new strategically designed RF feed network, MRSA allows to change physical location of the radiating antenna elements while any other RF and digital electronics hardware supporting the operation of the array remains stationary. A MRSA prototype has been realized at 28 GHz with 45 mm ($4.2\ \lambda_0$) spatial adaptation capability. The prototype was experimentally verified, and its measured realized gain pattern was utilized to show that MRSA achieves link-level performance improvement of 24% from 8.5 bps/Hz to 10.5 bps/Hz and spectral efficiency improvement of 100% with a 5 dB improvement in the average signal-to-interference ratio.

A frequency reconfigurable antenna has been introduced and designed to operate at 28 GHz or 38 GHz mm-Wave bands.Besides the RF design/reconfiguration approach, an important contribution was the first time demonstration of a multilayered microfluidic actuator that can simultaneously reposition multiple metalized plates within the microfluidic channel. Whereas previous designs required allocating a larger 2D area for multiple reservoirs, introducing vertically stacked reservoirs allowed for a reduction in the device's size.

The integrated compact actuation mechanism has been later on improved and used in mm-Wave phase shifters and beam steering antenna arrays. The first investigation was the design and experimental verification of a microfluidically actuated reconfigurable phase shifter (MRPS). The MRPS used SMP-based microfluidically reconfiguration techniques to create a variable loading on a microstrip. This investigation is supported by introducing a novel microfluidic actuated RF loading technique based on variable capacitive coupling as generated by SMP repositioning within the microfluidic channel, thereby altering the propagating wave's speed. The presented MRPS used a 100 µm reconfiguration distance to provide 305° of phase range at 28 GHz band and pawed the way for the microfluidically reconfigurable phased antenna arrays (MRPAAs).

Subsequently, a 28 GHz MRPAA has been introduced by devising a novel design process benefiting from customized MRPSs to create a beamforming network that can be controlled with one actuator. The MRPAA exhibited 200 µm SMP reconfiguration range that in turn translated into a measured scanning range of [-20°,30°]. MRPAA showed a peak realized gain between 5.6 dBi and 6.8 dBi.

7.1 Additional Comments and Recommendations

The integration of the devices presented in this investigation offers the possibility of a fully microfluidically actuated phased antenna array operating at 28 GHz or 38 GHz and with spatial

adaptation capability for an improved signal-to-interference ratio. However, this technology is better suited for high-power applications, such as backhauling, due to the reconfiguration times inherent to mechanical actuation. As a result, further work on actuation time improvement needs to be addressed.

Some solutions for speed improvement might include:

- The air bubbles (compressible fluid) inside the microfluidic channel are the primary source of operational waste when acting on these devices. Redesigning the reservoir structures to facilitate the extraction of air bubbles will prove helpful in increasing actuation speeds and general operation. A solution could be to utilize dome-shaped reservoirs instead of cylindrical to minimize air trapped in corners, as shown in Figure 7.1. Where initial filing with the aid of gravity helps the extraction of the air bubbles from the reservoir.

(a)   (b)
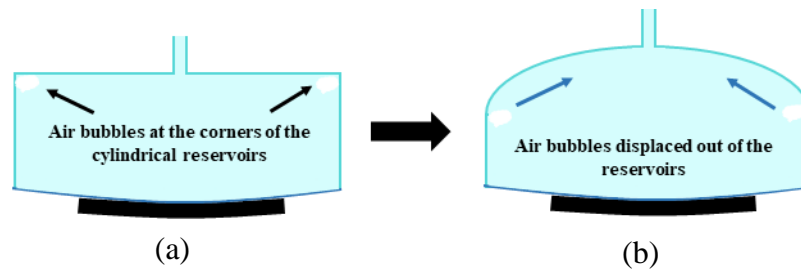
Figure 7.1: Reservoir shape. (a) Current shape cylindrical; (b) proposed reservoir shape.

- All the devices presented in this investigation utilize a copper thickness of 17 μm. This height is significant compared to the minimum SMP/PCB gap we can achieve with our current fabrication operational procedure (~5 microns). This high aspect ratio makes the control during the BCB/Parylene deposition step difficult. Therefore, thinner metal layers are a promising solution to increase manufacturing reliability

- The circuit model introduced in Chapter VI predicts the performance of a single-sided SMP phase shifter. However, the required mirroring step to achieve complete range scanning is not included in Figure 7.2
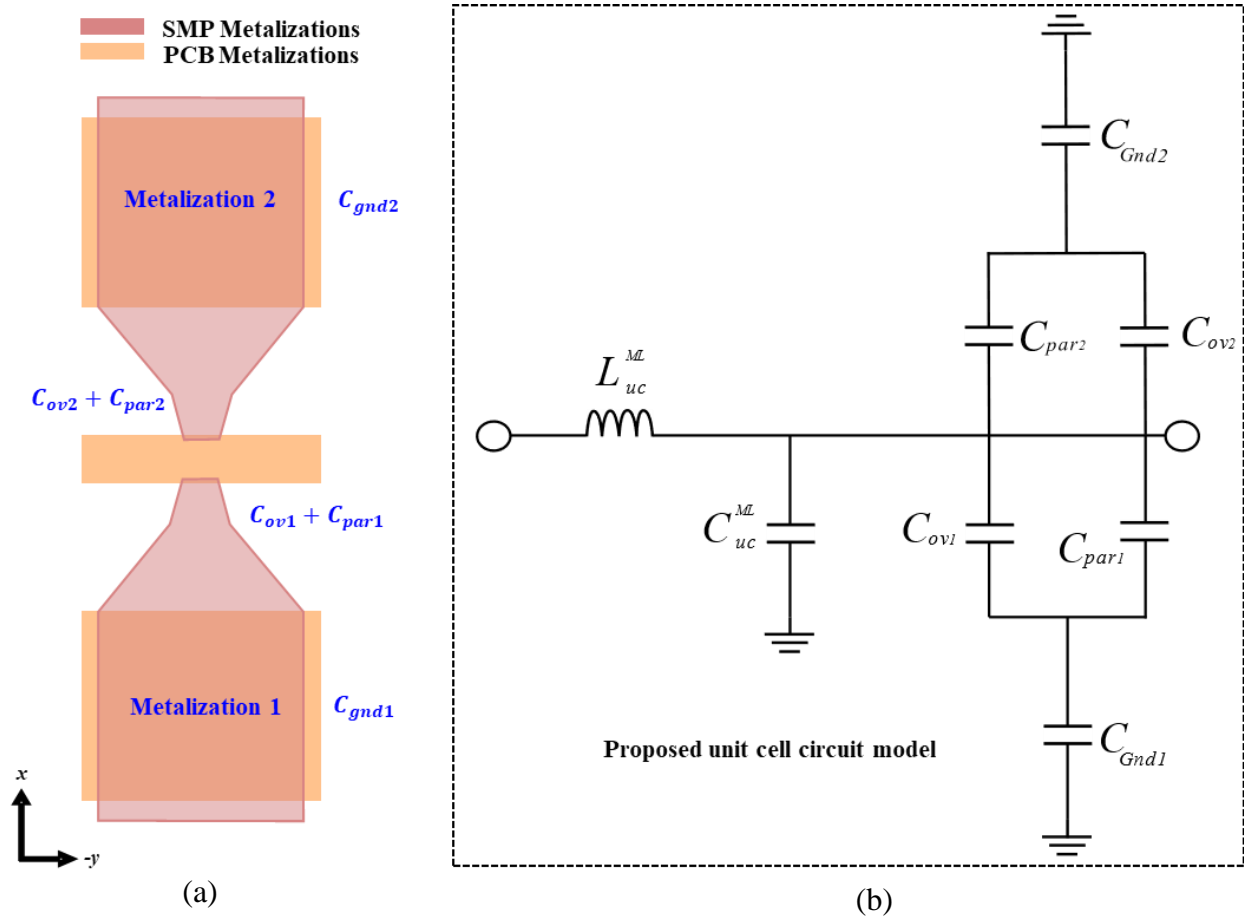

Figure 7.2: Proposed unit cell circuit model. (a) Layout; (b) Proposed circuit model.

References

[1] S. A. Busari, S. Mumtaz, K. M. S. Huq, J. Rodriguez, and H. Gacanin, "System-Level Performance Evaluation for 5G mmWave Cellular Network." pp. 1-7.

[2] "Front Matter," *Channel Equalization for Wireless Communications*, pp. i-xxvii, 2011.

[3] Q. Xue, P. Zhou, X. Fang, and M. Xiao, "Performance Analysis of Interference and Eavesdropping Immunity in Narrow Beam mmWave Networks," *IEEE Access,* vol. 6, pp. 67611-67624, 2018.

[4] Z. Pi, and F. Khan, "An introduction to millimeter-wave mobile broadband systems," *IEEE Communications Magazine,* vol. 49, no. 6, pp. 101-107, 2011.

[5] G. M. Rebeiz, and K. Koh, "Silicon RFICs for phased arrays," *IEEE Microwave Magazine,* vol. 10, no. 3, pp. 96-103, 2009.

[6] G. M. Rebeiz, C. D. Patel, S. K. Han, C. H. Ko, and K. M. J. Ho, "The Search for a Reliable MEMS Switch," *IEEE Microwave Magazine,* vol. 14, no. 1, pp. 57-67, 2013.

[7] B. D. Wiltshire, M. A. Rafi, and M. H. Zarifi, "Microwave resonator array with liquid metal selection for narrow band material sensing," *Scientific Reports,* vol. 11, no. 1, pp. 8598, 2021/04/21, 2021.

[8] N. Vahabisani, S. Khan, and M. Daneshmand, "A <italic>K</italic>-Band Reflective Waveguide Switch Using Liquid Metal," *IEEE Antennas and Wireless Propagation Letters,* vol. 16, pp. 1788-1791, 2017.

[9] V. Radonić, S. Birgermajer, and G. Kitić, "Microfluidic EBG Sensor Based on Phase-Shift Method Realized Using 3D Printing Technology," *Sensors (Basel, Switzerland),* vol. 17, no. 4, pp. 892, 2017.

[10] K. Entesari, and A. P. Saghati, "Fluidics in Microwave Components," *IEEE Microwave Magazine,* vol. 17, no. 6, pp. 50-75, 2016.

[11] A. Dey, R. Guldiken, and G. Mumcu, "Microfluidically Reconfigured Wideband Frequency-Tunable Liquid-Metal Monopole Antenna," *IEEE Transactions on Antennas and Propagation,* vol. 64, no. 6, pp. 2572-2576, 2016.

[12] T. Palomo, and G. Mumcu, "Frequency-agile RF filters using microfluidically reconfigurable selectively metallized plates." pp. 1-4.

[13] A. Qaroot, and G. Mumcu, "Microfluidically Reconfigurable Reflection Phase Shifter," *IEEE Microwave and Wireless Components Letters,* vol. 28, no. 8, pp. 684-686, 2018.

[14] E. González, and G. Mumcu, "Integrated Actuation of Microfluidically Reconfigurable mm-Wave SPST Switches," *IEEE Microwave and Wireless Components Letters,* vol. 29, no. 8, pp. 541-544 , ISSN = 1558-1764 , DOI = 10.1109/LMWC.2019.2925889, 2019.

[15] E. González-Carvajal, and G. Mumcu, "Frequency and Bandwidth Tunable mm-Wave Hairpin Bandpass Filters Using Microfluidic Reconfiguration With Integrated Actuation," *IEEE Transactions on Microwave Theory and Techniques,* vol. 68, no. 9, pp. 3756-3768, 2020.

[16] A. Gupta, and R. K. Jha, "A Survey of 5G Network: Architecture and Emerging Technologies," *IEEE Access,* vol. 3, pp. 1206-1232, 2015.

[17] *Use of spectrum bands above 24 GHz for mobile radio services* F. C. Commission, 2018.

[18] K. Q. T. Zhang, "Channel Characterization," *Wireless Communications*, pp. 37-69, 2015.

[19] C. Dehos, J. L. González, A. D. Domenico, D. Kténas, and L. Dussopt, "Millimeter-wave access and backhauling: the solution to the exponential data traffic increase in 5G mobile communications systems?," *IEEE Communications Magazine,* vol. 52, no. 9, pp. 88-95, 2014.

[20] L. Fa-Long, and Z. Charlie, "An Introduction to Modulations and Waveforms for 5G Networks," *Signal Processing for 5G: Algorithms and Implementations*, pp. 1-23: IEEE, 2016.

[21] S. Singh, M. N. Kulkarni, A. Ghosh, and J. G. Andrews, "Tractable Model for Rate in Self-Backhauled Millimeter Wave Cellular Networks," *IEEE Journal on Selected Areas in Communications,* vol. 33, no. 10, pp. 2196-2211, 2015.

[22] M. U. Sheikh, and J. Lempiäinen, "Analysis of multipath propagation for 5G system at higher frequencies in microcellular environment." pp. 1660-1664.

[23] E. B. Gregory, "Frontmatter," *Channel Equalization for Wireless Communications: From Concepts to Detailed Mathematics*, pp. i-xxvii: IEEE, 2011.

[24] V. Jungnickel, K. Manolakis, W. Zirwas, B. Panzner, V. Braun, M. Lossow, M. Sternad, R. Apelfröjd, and T. Svensson, "The role of small cells, coordinated multipoint, and massive MIMO in 5G," *IEEE Communications Magazine,* vol. 52, no. 5, pp. 44-51, 2014.

[25] C. Ming-Chin, C. Meng Chang, and S. Yeali, "Resource management issues in 5G ultra dense smallcell networks." pp. 159-164.

[26] Z. N. Chen, "Handbook of Antenna Technologies," *Springer Singapore*, pp. XXXI, 3473, 2016.

[27] Y. Rahmat-Samii, L. I. Williams, and R. G. Yaccarino, "The UCLA bi-polar planar-near-field antenna-measurement and diagnostics range," *IEEE Antennas and Propagation Magazine,* vol. 37, no. 6, pp. 16-35, 1995.

[28] Z. Mahlaoui, E. Antonino-Daviu, M. Ferrando-Bataller, H. Benchakroun, and A. Latif, "Frequency reconfigurable patch antenna with defected ground structure using varactor diodes." pp. 2217-2220.

[29] Y. Yashchyshyn, K. Derzakowski, P. R. Bajurko, J. Marczewski, and S. Kozłowski, "Time-Modulated Reconfigurable Antenna Based on Integrated S-PIN Diodes for mm-Wave Communication Systems," *IEEE Transactions on Antennas and Propagation,* vol. 63, no. 9, pp. 4121-4131, 2015.

[30] A. S. Emhemmed, and N. A. Ahmed, "Frequency reconfigurable proximity coupled patch antenna." pp. 1-5.

[31] Y. Luo, K. Kikuta, Z. Han, T. Takahashi, A. Hirose, and H. Toshiyoshi, "An Active Metamaterial Antenna With MEMS-Modulated Scanning Radiation Beams," *IEEE Electron Device Letters,* vol. 37, no. 7, pp. 920-923, 2016.

[32] A. A. Ibrahim, A. Batmanov, and E. P. Burte, "Design of reconfigurable antenna using RF MEMS switch for cognitive radio applications." pp. 369-376.

[33] Y. Xu, Y. Tian, B. Zhang, J. Duan, and L. Yan, "A novel RF MEMS switch on frequency reconfigurable antenna application," *Microsystem Technologies,* vol. 24, no. 9, pp. 3833-3841, 2018/09/01, 2018.

[34] S. Adhikari, Y. Ban, and K. Wu, "Magnetically Tunable Ferrite Loaded Substrate Integrated Waveguide Cavity Resonator," *IEEE Microwave and Wireless Components Letters,* vol. 21, no. 3, pp. 139-141, 2011.

[35] I. F. d. Costa, A. C. S, D. H. Spadoti, L. G. d. Silva, J. A. J. Ribeiro, and S. E. Barbin, "Optically Controlled Reconfigurable Antenna Array for mm-Wave Applications," *IEEE Antennas and Wireless Propagation Letters,* vol. 16, pp. 2142-2145, 2017.

[36] J. M. Floc'h, and I. B. Trad, "Design of mechanically reconfigurable meander antenna using the Galinstan liquid metal." pp. 1-4.

[37] M. Zhu, and L. Sun, "Design of frequency reconfigurable antenna based on metasurface." pp. 1785-1788.

[38] C. Wei-Shiuan, C. F. Yang, C. Chih-Kai, L. Wen-Jiao, C. Liang, and C. Wen-Shyh, "Pattern reconfigurable millimeter-wave antenna design for 5G handset applications." pp. 1-3.

[39] G. Mumcu, M. Kacar, and J. Mendoza, "Mm-Wave Beam Steering Antenna With Reduced Hardware Complexity Using Lens Antenna Subarrays," *IEEE Antennas and Wireless Propagation Letters,* vol. 17, no. 9, pp. 1603-1607, 2018.

[40] S. Foo, "Millimeter-wave TTD metamaterial Fresnel lens." pp. 2649-2650.

[41] K. Daheshpour, S. J. Mazlouman, A. Mahanfar, J. X. Yun, X. Han, C. Menon, F. Carpi, and R. G. Vaughan, "Pattern reconfigurable antenna based on moving V-shaped parasitic elements actuated by dielectric elastomer," *Electronics Letters,* 46, https://digital-library.theiet.org/content/journals/10.1049/el.2010.0862, 2010].

[42] G. Dufour, N. Tiercelin, W. T. Khan, P. Coquet, P. Pernod, and J. Papapolymerou, "Large frequency tuning of a millimeter-wave antenna using dielectric liquids in integrated micro-channels." pp. 1-4.

[43] S. A. Long, and G. H. Huff, "Experiments on a fluidic loading mechanism for beam-steering reflectarrays." pp. 1-4.

[44] A. Singh, and C. E. Saavedra, "Fluidic Stub-Loaded Patch Antenna for Frequency-Tunable Polarization Reconfiguration," *IEEE Open Journal of Antennas and Propagation,* vol. 2, pp. 362-369, 2021.

[45] G. Mumcu, A. Dey, and T. Palomo, "Frequency-Agile Bandpass Filters Using Liquid Metal Tunable Broadside Coupled Split Ring Resonators," *IEEE Microwave and Wireless Components Letters,* vol. 23, no. 4, pp. 187-189, 2013.

[46] A. Dey, R. Guldiken, and G. Mumcu, "Wideband frequency tunable liquid metal monopole antenna." pp. 392-393.

[47] A. Gheethan, R. Guldiken, and G. Mumcu, "Microfluidic enabled beam scanning focal plane arrays." pp. 208-209.

[48] V. T. Bharambe, and J. J. Adams, "Planar 2-D Beam Steering Antenna Using Liquid Metal Parasitics," *IEEE Transactions on Antennas and Propagation,* vol. 68, no. 11, pp. 7320-7327, 2020.

[49] E. Carrasco, J. Gomez-Cruz, M. Serrano-Berrueco, C. E. Saavedra, and C. Escobedo, "Design of Microfluidic Reflectarray Elements for Multi-Reconfiguration Using Liquid Metal," *IEEE Open Journal of Antennas and Propagation,* vol. 3, pp. 425-434, 2022.

[50] L. Song, W. Gao, C. O. Chui, and Y. Rahmat-Samii, "Liquid metal 3D printed microfluidic channel reconfigurable patch antenna with switchable slots." pp. 1-2.

[51] A. Arbelaez, I. Goode, J. Gomez-Cruz, C. Escobedo, and C. E. Saavedra, "Liquid Metal Reconfigurable Patch Antenna for Linear, RH, and LH Circular Polarization With Frequency Tuning," *Canadian Journal of Electrical and Computer Engineering,* vol. 43, no. 4, pp. 218-223, 2020.

[52] T. Palomo, and G. Mumcu, "Highly reconfigurable bandpass filters using microfluidically controlled metallized glass plates." pp. 1-3.

[53] A. Gheethan, and G. Mumcu, "2D beam scanning focal plane array using microfluidic reconfiguration techniques." pp. 1666-1667.

[54] A. A. Gheethan, A. Dey, and G. Mumcu, "Passive Feed Network Designs for Microfluidic Beam-Scanning Focal Plane Arrays and Their Performance Evaluation," *IEEE Transactions on Antennas and Propagation,* vol. 63, no. 8, pp. 3452-3464, 2015.

[55] A. Dey, and G. Mumcu, "Microfluidically Controlled Frequency-Tunable Monopole Antenna for High-Power Applications," *IEEE Antennas and Wireless Propagation Letters,* vol. 15, pp. 226-229, 2016.

[56] A. Dey, and G. Mumcu, "Small microfluidically tunable top loaded monopole." pp. 148-149.

[57] E. Gonzalez, and G. Mumcu, "A microfluidically switched feed network for beam-scanning focal plane arrays." pp. 5-6.

[58] M. H. Yılmaz, E. Güvenkaya, G. Mumcu, and H. Arslan, "Millimeter-Wave Wireless Channel Control Using Spatially Adaptive Antenna Arrays," *IEEE Communications Letters,* vol. 21, no. 3, pp. 680-683, 2017.

[59] E. González, and G. Mumcu, "Integrated Actuation of Microfluidically Reconfigurable mm-Wave SPST Switches," *IEEE Microwave and Wireless Components Letters,* vol. 29, no. 8, pp. 541-544, 2019.

[60] A. Dey, A. Kiourti, G. Mumcu, and J. L. Volakis, "Microfluidically reconfigured frequency tunable dipole antenna." pp. 1-2.

[61] E. González, and G. Mumcu, "Mm-wave 2D beam-steering focal plane array with microfluidically switched feed network." pp. 907-908.

[62] C. Kim, H. Chun, J. Chung, K. Song, and S. Lee, "Non-collapsible PDMS nanochannel fabrication with tunable width and height using single master mold." pp. 1723-1727.

[63] J. Hacker, C. Hillman, A. Papavasiliou, K. Chong Gon, A. Abbaspour-Tamijani, C. Y. Kim, D. W. Kang, and G. Rebeiz, "A 16-element transmit/receive Q-band electronically steerable subarray tile." pp. 1-3.

[64] B. Sadhu, Y. Tousi, J. Hallin, S. Sahl, S. K. Reynolds, R. Ö, K. Sjögren, O. Haapalahti, N. Mazor, B. Bokinge, G. Weibull, H. Bengtsson, A. Carlinger, E. Westesson, J. E. Thillberg, L. Rexberg, M. Yeck, X. Gu, M. Ferriss, D. Liu, D. Friedman, and A. Valdes-Garcia, "A 28-GHz 32-Element TRX Phased-Array IC With Concurrent Dual-Polarized Operation and Orthogonal Phase and Gain Control for 5G Communications," *IEEE Journal of Solid-State Circuits,* vol. 52, no. 12, pp. 3373-3391, 2017.

[65] J. Wu, Y. J. Cheng, and Y. Fan, "A Wideband High-Gain High-Efficiency Hybrid Integrated Plate Array Antenna for V-Band Inter-Satellite Links," *IEEE Transactions on Antennas and Propagation,* vol. 63, no. 4, pp. 1225-1233, 2015.

[66] O. Bayraktar, O. A. Civi, and T. Akin, "Beam Switching Reflectarray Monolithically Integrated With RF MEMS Switches," *IEEE Transactions on Antennas and Propagation,* vol. 60, no. 2, pp. 854-862, 2012.

[67] C. H. Li, T. Y. Chao, C. W. Lai, W. C. Chen, C. L. Ko, C. N. Kuo, Y. T. Cheng, M. C. Kuo, and D. C. Chang, "A 37.5-mW 8-dBm-EIRP 15.5°-HPBW 338-GHz Terahertz Transmitter Using SoP Heterogeneous System Integration," *IEEE Transactions on Microwave Theory and Techniques,* vol. 63, no. 2, pp. 470-480, 2015.

[68]   E. A. Rojas-Nastrucci, R. Ramirez, D. Hawatmeh, D. Lan, J. Wang, and T. Weller, "Laser enhanced direct print additive manufacturing for mm-wave components and packaging." pp. 1531-1534.

[69]   M. Kacar, J. Wang, G. Mumcu, C. Perkowski, K. Church, B. I. Wu, and T. Weller, "Phased Array Antenna Element with Embedded Cavity and MMIC using Direct Digital Manufacturing." pp. 81-82.

[70]   Y.-C. Tsai, Y.-B. Chen, and R.-B. Hwang, "Combining the switched-beam and beam-steering capabilities in a 2-D phased array antenna system," *Radio Science,* vol. 51, pp. 47-58, 2016.

[71]   A. Abbaspour-Tamijani, and K. Sarabandi, "An affordable millimeter-wave beam-steerable antenna using interleaved planar subarrays," *IEEE Transactions on Antennas and Propagation,* vol. 51, no. 9, pp. 2193-2202, 2003.

[72]   F. Akbar, and A. Mortazawi, "Scalable Phased Array Architectures With a Reduced Number of Tunable Phase Shifters," *IEEE Transactions on Microwave Theory and Techniques,* vol. 65, no. 9, pp. 3428-3434, 2017.

[73]   C. Chang, R. Lee, and T. Shih, "Design of a Beam Switching/Steering Butler Matrix for Phased Array System," *IEEE Transactions on Antennas and Propagation,* vol. 58, no. 2, pp. 367-374, 2010.

[74]   D. F. Filipovic, S. S. Gearhart, and G. M. Rebeiz, "Double-slot antennas on extended hemispherical and elliptical silicon dielectric lenses," *IEEE Transactions on Microwave Theory and Techniques,* vol. 41, no. 10, pp. 1738-1749, 1993.

[75]   D. I. Abu-Al-Nadi, T. H. Ismail, and M. J. Mismar, "Interference suppression by element position control of phased arrays using LM algorithm," *AEU - International Journal of Electronics and Communications,* vol. 60, no. 2, pp. 151-158, 2006/02/13/, 2006.

[76]   F. Tokan, and F. Güneş, "Interference suppression by optimising the positions of selected elements using generalised pattern search algorithm," *Microwaves, Antennas & Propagation, IET,* vol. 5, pp. 127-135, 03/03, 2011.

[77]   M. K. Samimi, S. Sun, and T. S. Rappaport, "MIMO channel modeling and capacity analysis for 5G millimeter-wave wireless systems." pp. 1-5.

[78]   B. Ai, K. Guan, R. He, J. Li, G. Li, D. He, Z. Zhong, and K. M. S. Huq, "On Indoor Millimeter Wave Massive MIMO Channels: Measurement and Simulation," *IEEE Journal on Selected Areas in Communications,* vol. 35, no. 7, pp. 1678-1690, 2017.

[79]   S. Guillouard, G. E. Zein, and J. Citerne, "Wideband propagation measurements and Doppler analysis for the 60 GHz indoor channel." pp. 1751-1754 vol.4.

[80]   N. Moraitis, and P. Constantinou, "Indoor channel measurements and characterization at 60 GHz for wireless local area network applications," *IEEE Transactions on Antennas and Propagation,* vol. 52, no. 12, pp. 3180-3189, 2004.

[81]   E. González, and G. Mumcu, "Millimeter-Wave Beam-Steering Focal Plane Arrays With Microfluidically Switched Feed Networks," *IEEE Transactions on Antennas and Propagation,* vol. 66, no. 12, pp. 7424-7429, 2018.

[82]   A. A. Gheethan, M. C. Jo, R. Guldiken, and G. Mumcu, "Microfluidic Based Ka-Band Beam-Scanning Focal Plane Array," *IEEE Antennas and Wireless Propagation Letters,* vol. 12, pp. 1638-1641, 2013.

[83]   H. E. Bussey, J. E. Gray, E. C. Bamberger, E. Rushton, G. Russell, B. W. Petley, and D. Morris, "International Comparison of Dielectric Measurements," *IEEE Transactions on Instrumentation and Measurement,* vol. IM-13, no. 4, pp. 305-311, 1964.

[84] T. Namiki, Y. Murayama, and K. Ito, "Improving radiation-pattern distortion of a patch antenna having a finite ground plane," *IEEE Transactions on Antennas and Propagation,* vol. 51, no. 3, pp. 478-482, 2003.

[85] J. Huang, "The finite ground plane effect on the microstrip antenna radiation patterns," *IEEE Transactions on Antennas and Propagation,* vol. 31, no. 4, pp. 649-653, 1983.

[86] A. Kumar, J. Mohan, and H. Gupta, "Surface wave suppression of microstrip antenna using different EBG designs." pp. 355-359.

[87] N. Llombart, A. Neto, G. Gerini, and P. d. Maagt, "Planar circularly symmetric EBG structures for reducing surface waves in printed antennas," *IEEE Transactions on Antennas and Propagation,* vol. 53, no. 10, pp. 3210-3218, 2005.

[88] R. Gonzalo, P. D. Maagt, and M. Sorolla, "Enhanced patch-antenna performance by suppressing surface waves using photonic-bandgap substrates," *IEEE Transactions on Microwave Theory and Techniques,* vol. 47, no. 11, pp. 2131-2138, 1999.

[89] T. Palomo, and G. Mumcu, "Microfluidically Reconfigurable Microstrip Line Combline Filters With Wide Frequency Tuning Capabilities," *IEEE Transactions on Microwave Theory and Techniques,* vol. 65, no. 10, pp. 3561-3568, 2017.

[90] S. Choi, W. Su, M. M. Tentzeris, and S. Lim, "A Novel Fluid-Reconfigurable Advanced and Delayed Phase Line Using Inkjet-Printed Microfluidic Composite Right/Left-Handed Transmission Line," *IEEE Microwave and Wireless Components Letters,* vol. 25, no. 2, pp. 142-144, 2015.

[91] V. Bharambe, J. J. Adams, I. D. Joshipura, H. R. Ayers, and M. D. Dickey, "Reversibly Reconfigurable Liquid Metal Patch Antenna Using A Superhydrophobic Spray-Coating." pp. 287-288.

[92] A. J. King, J. F. Patrick, N. R. Sottos, S. R. White, G. H. Huff, and J. T. Bernhard, "Microfluidically Switched Frequency-Reconfigurable Slot Antennas," *IEEE Antennas and Wireless Propagation Letters,* vol. 12, pp. 828-831, 2013.

[93] L. Yu, C. Iliescu, F. e. h. Tay, and B. Chen, "SU8 Adhesive Bonding using Contact Imprinting." pp. 189-192.

[94] A. Dey, and G. Mumcu, "Microfluidically controlled metalized plate based frequency reconfigurable monopole for high power RF applications." pp. 2299-2300.

[95] S. Rangan, T. S. Rappaport, and E. Erkip, "Millimeter-Wave Cellular Wireless Networks: Potentials and Challenges," *Proceedings of the IEEE,* vol. 102, no. 3, pp. 366-385, 2014.

[96] N. Ojaroudiparchin, M. Shen, and G. F. Pedersen, "Low-cost planar MM-wave phased array antenna for use in mobile satellite (MSAT) platforms." pp. 528-531.

[97] M. Islam, M. Ibrahimy, S. Motakabber, A. K. M. Z. Hossain, and S. M. Azam, "Microstrip Patch Antenna with Defected Ground Structure for Biomedical Application," vol. 8, pp. 586-595, 06/01, 2019.

[98] K. V. Kishore, G. S. Rajesh, V. Kumar, and P. Srinivasulu, "Design of 0.71λ, spacing 8-element microstrip patch antenna linear array for 0.43GHz wind profiling radar." pp. 1-6.

[99] K. Kibaroglu, M. Sayginer, and G. M. Rebeiz, "An ultra low-cost 32-element 28 GHz phased-array transceiver with 41 dBm EIRP and 1.0–1.6 Gbps 16-QAM link at 300 meters." pp. 73-76.

[100] J. Huang, "A Ka-band circularly polarized high-gain microstrip array antenna," *IEEE Transactions on Antennas and Propagation,* vol. 43, no. 1, pp. 113-116, 1995.

[101] C. Deng, B. Yektakhah, and K. Sarabandi, "Series-Fed Dual-Polarized Single-Layer Linear Patch Array With High Polarization Purity," *IEEE Antennas and Wireless Propagation Letters,* vol. 18, no. 9, pp. 1746-1750, 2019.

[102] N. Ojaroudiparchin, M. Shen, S. Zhang, and G. F. Pedersen, "A Switchable 3-D-Coverage-Phased Array Antenna Package for 5G Mobile Terminals," *IEEE Antennas and Wireless Propagation Letters,* vol. 15, pp. 1747-1750, 2016.

[103] K. Y. Alqurashi, and J. R. Kelly, "Continuously tunable frequency reconfigurable liquid metal microstrip patch antenna." pp. 909-910.

[104] A. Valdes-Garcia, S. T. Nicolson, J. W. Lai, A. Natarajan, P. Y. Chen, S. K. Reynolds, J. H. C. Zhan, D. G. Kam, D. Liu, and B. Floyd, "A Fully Integrated 16-Element Phased-Array Transmitter in SiGe BiCMOS for 60-GHz Communications," *IEEE Journal of Solid-State Circuits,* vol. 45, no. 12, pp. 2757-2773, 2010.

[105] Z. Gao, L. Dai, D. Mi, Z. Wang, M. A. Imran, and M. Z. Shakir, "MmWave massive-MIMO-based wireless backhaul for the 5G ultra-dense network," *IEEE Wireless Communications,* vol. 22, no. 5, pp. 13-21, 2015.

[106] L. Jeon, and J.-G. Kim, "A Compact X-Band Bi-Directional Phased-Array T/R Chipset in 0.13 $\mu{\hbox {m}}$ CMOS Technology," *IEEE Transactions on Microwave Theory Techniques,* vol. 61, pp. 562-569, 01/01, 2013.

[107] D. M. Zaiden, J. E. Grandfield, T. M. Weller, and G. Mumcu, "Compact and Wideband MMIC Phase Shifters Using Tunable Active Inductor-Loaded All-Pass Networks," *IEEE Transactions on Microwave Theory and Techniques,* vol. 66, no. 2, pp. 1047-1057, 2018.

[108] M. Sayginer, and G. M. Rebeiz, "An Eight-Element 2–16-GHz Programmable Phased Array Receiver With One, Two, or Four Simultaneous Beams in SiGe BiCMOS," *IEEE Transactions on Microwave Theory and Techniques,* vol. 64, no. 12, pp. 4585-4597, 2016.

[109] C. W. Byeon, and C. S. Park, "A Low-Loss Compact 60-GHz Phase Shifter in 65-nm CMOS," *IEEE Microwave and Wireless Components Letters,* vol. 27, no. 7, pp. 663-665, 2017.

[110] S. Dey, and S. K. Koul, "Reliability Analysis of Ku-Band 5-bit Phase Shifters Using MEMS SP4T and SPDT Switches," *IEEE Transactions on Microwave Theory and Techniques,* vol. 63, no. 12, pp. 3997-4012, 2015.

[111] P. Edinger, C. Errando-Herranz, and K. B. Gylfason, "Low-Loss MEMS Phase Shifter for Large Scale Reconfigurable Silicon Photonics." pp. 919-921.

[112] W. Tian, Y. Zhang, M. Li, Z. Xie, and W. Li, "5-Bit Spiral Distributed RF MEMS Phase Shifter." pp. 94-98.

[113] S. Khan, N. Vahabisani, and M. Daneshmand, "A Fully 3-D Printed Waveguide and Its Application as Microfluidically Controlled Waveguide Switch," *IEEE Transactions on Components, Packaging and Manufacturing Technology,* vol. 7, no. 1, pp. 70-80, 2017.

[114] L. L. Cloirec, A. Benlarbi-Delai, and B. Bocquet, "3 bit 90/spl deg/ millimeter phase shifter using microfluidic technology." pp. 1161-1164.

[115] K. Khoshmanesh, S.-Y. Tang, J. Y. Zhu, S. Schaefer, A. Mitchell, K. Kalantar-zadeh, and M. D. Dickey, "Liquid metal enabled microfluidics," *Lab on a Chip,* vol. 17, no. 6, pp. 974-993, 2017.

[116] T. Palomo, and G. Mumcu, "Microfluidically Reconfigurable Metallized Plate Loaded Frequency-Agile RF Bandpass Filters," *IEEE Transactions on Microwave Theory and Techniques,* vol. 64, no. 1, pp. 158-165, 2016.

[117] M. Azarmanesh, M. Dejam, P. Azizian, G. Yesiloz, A. A. Mohamad, and A. Sanati-Nezhad, "Passive microinjection within high-throughput microfluidics for controlled actuation of droplets and cells," *Scientific Reports,* vol. 9, no. 1, pp. 6723, 2019/04/30, 2019.

[118] J. Mendoza, and G. Mumcu, "Mm-Wave Frequency Reconfigurable Antenna with Multilayer Integrated Microfluidic Actuation." pp. 145-146.

[119] N. S. Barker, and G. M. Rebeiz, "Optimization of distributed MEMS transmission-line phase shifters-U-band and W-band designs," *IEEE Transactions on Microwave Theory and Techniques,* vol. 48, no. 11, pp. 1957-1966, 2000.

[120] J. Mendoza, M. Karabacak, H. Arslan, and G. Mumcu, "A Spatially Adaptive Antenna Array for Mm-Wave Wireless Channel Control With Microfluidics Based Reconfiguration," *IEEE Access,* vol. 8, pp. 182898-182907, 2020.

[121] J. A. Palyvos, "A survey of wind convection coefficient correlations for building envelope energy systems' modeling," *Applied Thermal Engineering,* vol. 28, no. 8, pp. 801-808, 2008/06/01/, 2008.

[122] T. Singh, N. K. Khaira, and R. R. Mansour, "Thermally Actuated SOI RF MEMS-Based Fully Integrated Passive Reflective-Type Analog Phase Shifter for mmWave Applications," *IEEE Transactions on Microwave Theory and Techniques,* vol. 69, no. 1, pp. 119-131, 2021.

[123] A. Borgioli, L. Yu, A. S. Nagra, and R. A. York, "Low-loss distributed MEMS phase shifter," *IEEE Microwave and Guided Wave Letters,* vol. 10, no. 1, pp. 7-9, 2000.

[124] C. Çalışkan, M. Yazici, and Y. Gurbuz, "All-Pass Network and Transformer Based SiGe BiCMOS Phase Shifter for Multi-Band Arrays," *IEEE Transactions on Circuits and Systems II: Express Briefs,* vol. 68, no. 1, pp. 186-190, 2021.

[125] L. Weijun, H. Liu, Z. Zhang, P. Sun, and X. Liu, "High-Power X-Band 5-b GaN Phase Shifter with Monolithic Integrated E/D HEMTs Control Logic," *IEEE Transactions on Electron Devices,* vol. PP, pp. 1-7, 08/04, 2017.

[126] L. Wang, B. Ai, Y. Niu, X. Chen, and P. Hui, "Energy-Efficient Power Control of Train–Ground mmWave Communication for High-Speed Trains," *IEEE Transactions on Vehicular Technology,* vol. 68, no. 8, pp. 7704-7714, 2019.

[127] G. X. Kong, X. Q. Li, J. Q. Zhang, and Q. F. Wang, "Design of a millimeter wave helical reflectarray antenna with high power handling capacity," *Journal of Physics: Conference Series,* vol. 1607, no. 1, pp. 012007, 2020/08/01, 2020.

[128] J. Shin, J. Bae, H. Koo, S. Bae, J. Na, H. Oh, H. Jeon, H. Jung, Y. C. Choi, S. Woo, C. M. Song, K. C. Hwang, K. Y. Lee, and Y. Yang, "5.8 GHz 4-Channel Beamforming Tx IC for Microwave Power Transfer," *IEEE Access,* vol. 9, pp. 72316-72325, 2021.

[129] W. Theunissen, V. Jain, and G. Menon, "Development of a Receive Phased Array Antenna for High Altitude Platform Stations using Integrated Beamformer Modules." pp. 779-782.

[130] C. Laffey, S. K. Sharma, R. Farkouh, and J. C. S. Chieh, "Dual Mode Phased Array Antenna using Silicon RFICs based Integrated Beamforming Network." pp. 35-38.

[131] S. S. Madeti, Z. Salahuddin, C. N. R. Pearce, S. E. Saddow, G. Mumcu, F. Vassallo, and D. Katherine, "Broadband 8–12 GHz 8 × 8 Modified Butler Matrix." pp. 1-6.

[132] A. Tajik, A. S. Alavijeh, and M. Fakharzadeh, "Asymmetrical 4×4 Butler Matrix and its Application for Single Layer 8×8 Butler Matrix," *IEEE Transactions on Antennas and Propagation,* vol. 67, no. 8, pp. 5372-5379, 2019.

[133] K. A. Shila, and G. Mumcu, "Mm-Wave Beam Steering Antenna Based on Extended Hemispherical Lens Antenna Subarrays." pp. 1517-1518.

[134] J. Mendoza, and G. Mumcu, "Microfluidically Reconfigurable Mm-Wave Slow-Wave Phase Shifter with Integrated Actuation," 2022.

[135] P. Meineri, D. Dubuc, and K. Grenier, "Liquid-based tunable loaded-line phase shifter." pp. 719-722.

[136] H. M. Oh, J. T. Lim, J. E. Lee, E. G. Lee, J. Lee, S. K. Choi, C. W. Byeon, J. H. Son, J. H. Lee, and C. Y. Kim, "28 GHz Wilkinson power divider with λ/6 transmission lines in 65nm CMOS technology." pp. 206-209.

[137] J. Kim, and G. M. Rebeiz, "Miniature Four-Way and Two-Way 24 GHz Wilkinson Power Dividers in 0.13 μm CMOS," *IEEE Microwave and Wireless Components Letters,* vol. 17, no. 9, pp. 658-660, 2007.

[138] S. Kim, S. Jeon, and J. Jeong, "Compact three-way planar power divider using five-conductor coupled line," *IEICE Electronics Express,* vol. 8, 09/10, 2011.

[139] M.-J. Chiang, H.-S. Wu, and C. Tzuang, "Correction to "A Ka-Band CMOS Wilkinson Power Divider Using Synthetic Quasi-TEM Transmission Lines"," *Microwave and Wireless Components Letters, IEEE,* vol. 18, pp. 148-148, 03/01, 2008.

[140] H. J. Qian, J. Zhou, B. Yang, and X. Luo, "A 4-Element Digital Modulated Polar Phased-Array Transmitter With Phase Modulation Phase-Shifting," *IEEE Journal of Solid-State Circuits,* vol. 56, no. 11, pp. 3331-3347, 2021.

[141] M. C. Tan, M. Li, Q. H. Abbasi, and M. A. Imran, "A Wideband Beamforming Antenna Array for 802.11ac and 4.9 GHz in Modern Transportation Market," *IEEE Transactions on Vehicular Technology,* vol. 69, no. 3, pp. 2659-2670, 2020.

[142] R. Lu, C. Yu, Y. Zhu, and W. Hong, "Compact Millimeter-Wave Endfire Dual-Polarized Antenna Array for Low-Cost Multibeam Applications," *IEEE Antennas and Wireless Propagation Letters,* vol. 19, no. 12, pp. 2526-2530, 2020.

[143] H. Ren, P. Li, Y. Gu, and B. Arigong, "Phase Shifter-Relaxed and Control-Relaxed Continuous Steering Multiple Beamforming 4 × 4 Butler Matrix Phased Array," *IEEE Transactions on Circuits and Systems I: Regular Papers,* vol. 67, no. 12, pp. 5031-5039, 2020.

[144] J. J. Luther, S. Ebadi, and X. Gong, "A Low-Cost 2 $\times$ 2 Planar Array of Three-Element Microstrip Electrically Steerable Parasitic Array Radiator (ESPAR) Subcells," *IEEE Transactions on Microwave Theory and Techniques,* vol. 62, no. 10, pp. 2325-2336, 2014.

[145] R. Lu, C. Weston, D. Weyer, F. Buhler, D. Lambalot, and M. P. Flynn, "A 16-Element Fully Integrated 28-GHz Digital RX Beamforming Receiver," *IEEE Journal of Solid-State Circuits,* vol. 56, no. 5, pp. 1374-1386, 2021.

[146] J. Pang, Z. Li, R. Kubozoe, X. Luo, R. Wu, Y. Wang, D. You, A. A. Fadila, R. Saengchan, T. Nakamura, J. Alvin, D. Matsumoto, B. Liu, A. T. Narayanan, J. Qiu, H. Liu, Z. Sun, H. Huang, K. K. Tokgoz, K. Motoi, N. Oshima, S. Hori, K. Kunihiro, T. Kaneko, A. Shirane, and K. Okada, "A 28-GHz CMOS Phased-Array Beamformer Utilizing Neutralized Bi-Directional Technique Supporting Dual-Polarized MIMO for 5G NR," *IEEE Journal of Solid-State Circuits,* vol. 55, no. 9, pp. 2371-2386, 2020.

Appendix A: 3D Printed Reservoirs

This appendix details the dimensions of the vertically stacked reservoir utilized in the prototypes in Chapter 5. Figure A.1 shows the vertical reservoir assembly and its exploded view identifying the different structures forming it. The membranes were replaced with a more flexible 0.1 mm thick substrate.
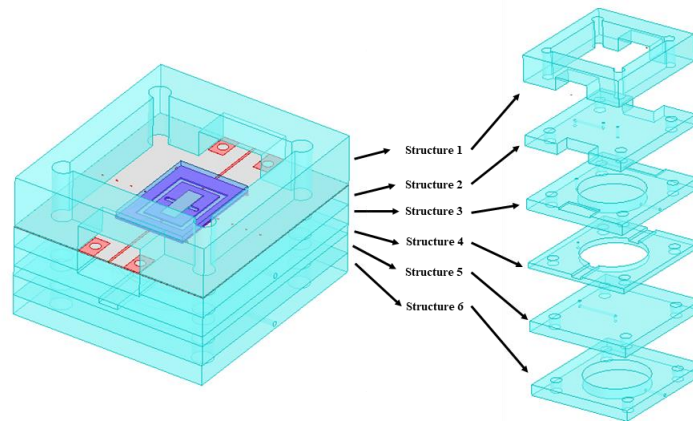
Figure A.1: Reservoir assembly

The details of each structure is shown in Figure A.2
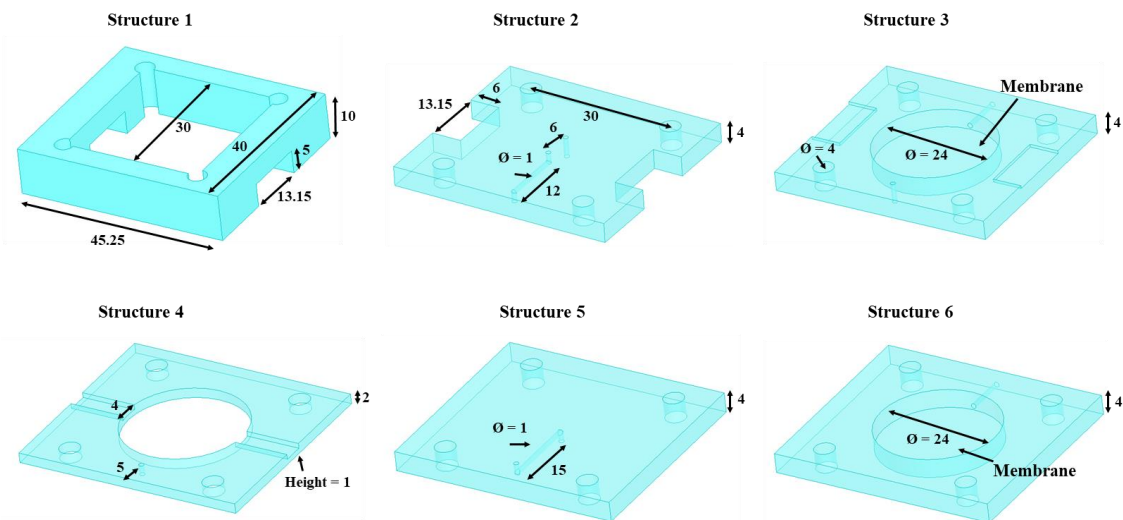
Figure A.2: Reservoir structures dimensions

Appendix B: Copyright Permissions

The permission below is for the reproduction of material in Chapter 3.

The permission below is for the reproduction of material in Chapter 4.

About the Author

Jonas J. Mendoza Sandoval was born and raised in Venezuela in 1989; he received his B.Eng. Degree in electrical engineering from the Electrical Engineering department of Universidad de Carabobo in August 2012 (Venezuela). In Venezuela, he gained experience in the most important manufacturing companies in the country, developing his interest in applying the PMI best practices for various EE projects, offering practical expertise on drive unit implementation. He also worked as an optimization project engineer to research, design, and implement system improvements to enhance OEE performance. He joined the University of South Florida in 2017 as a research assistant under the guidance of Dr. Gokhan Mumcu to pursue Ph.D.-level studies in RF and microwave systems. He developed his RF systems expertise on the topics of RF filters, MMIC technology, low-noise amplifiers, power amplifiers, mm-wave antenna arrays, lens antennas, and advanced antenna design. Likewise, he developed several 3D virtual scenarios as a visual guide to improving undergrad students' understanding of electromagnetic fields in space. Additionally, He acquired experience as a lab manager (anechoic chamber) at Reconfigurable RF Devices & Systems Laboratory (ReDS). Jonas also takes pride in elevating USF status by coordinating the WAMI Forum conference as General Chair for two consecutive years 2019 - 2020.